Title

Bioinspired Materials to Address Challenges in Biomedicine and Cellular Agriculture

Author

Nasajpour, Amir

Publication Date

2023

Peer reviewed|Thesis/dissertation

UNIVERSITY OF CALIFORNIA

Los Angeles

Bioinspired Materials to Address Challenges in Biomedicine and Cellular Agriculture

A dissertation submitted in partial satisfaction of the

requirements for the degree Doctor of Philosophy

in Chemistry

by

Amir Nasajpour

2023

ABSTRACT OF THE DISSERTATION

Bioinspired Materials to Address Challenges in Biomedicine and Cellular Agriculture

by

Amir Nasajpour

Doctor of Philosophy in Chemistry

University of California, Los Angeles, 2023

Professor Paul S. Weiss, Chair

Nature has developed advanced materials after billions of years of evolution in an exquisite way, giving rise to elaborate materials with optimized designs, architectures, properties, and functionalities. These functionalities emerge from the directed assembly of biomolecules from the molecular level up to the length scales relevant to living cells, cellular tissue, and entire organisms.

Inspired by these bottom-up assembly processes, I have developed materials that self-assemble into active substrates mimicking the actuation found in living muscle fibers. The resulting bioinspired materials display properties that mimic endogenous viscoelastic properties found in collagen and, consequently, push muscle cellular differentiation faster than the state-of-the-art elastic scaffolds. During my PhD, I developed a nonwoven CLC electrospun scaffold by dispersing three cholesteryl ester-based mesogens within polycaprolactone (PCL). We tuned the ratio of our mesogens so that the CLC would be in the mesophase at the cell culture incubator temperature of 37 °C. In these scaffolds, the PCL polymer provided an elastic bulk matrix while

the homogeneously dispersed CLC established a viscoelastic fluidlike interface. Increasing the CLC concentration within the composites enhanced myoblast adhesion strength promoted myofibril formation in vitro with mouse myoblast cell lines. Cholesteryl ester liquid crystals (CLCs) intrinsic ability to organize into supramolecular helicoidal structures on the mesoscale allows cell-helix interaction to create dynamic biomaterials.

Inspired by the shoaling behavior of fish, I devised a method to deploy the CLC-helix to orchestrate and to template the three-dimensional aggregation of anchorage-dependent cells lines. The 3D cellular aggregates are rapidly produced off the dynamic scaffold providing a platform to manufacture cost-effective organoids for precision medicine and cellular agriculture.

As scientists, it is our calling to provide solutions to protect society. During my PhD, we were faced with the Coronavirus (COVID-19) pandemic. We developed a self-cleaning fabric ambient environment sunlight provides enough energy to stimulate the band gap of embedded 3D anisotropic nanoparticles fiber matrix, mixing the dimensionality of the nanomaterial mentioned gives rise to rose-thorn-like protrusions a natural defense plant morphology seen in nature.

Herpes simplex virus (HSV) plagues billions of humans with infections globally. We have developed and demonstrated rose-thorn-inspired antiviral fibrous arrays by electrospinning a composite of polycaprolactone (PCL) polymer with a dispersion of anisotropic zinc oxide tetrapod nanoparticles (ZOTeN). This rose-thorn-mimicking material enables physical and chemical protection. Under blue-light stimulation, ZOTeN photocatalyzes the production of hydrogen peroxide for an accessible disinfection and sterilizing mechanism to prolong materials usage. The fibrous material has dose-dependent antiviral properties against both HSV-1 and HSV-2. The engineered mats can potentially be used for manufacturing antiviral garments, face coverings, and bandages.

The dissertation of Amir Nasajpour is approved.

Justin R. Caram

William M. Gelbart

Alireza Moshavernia

Hosea Martin Nelson

Paul S. Weiss, Committee Chair

University of California, Los Angeles

2023

To my colleagues, mentors, and family

TABLE OF CONTENTS

Table of Contents

List of Tables & Figures

List of Abbreviations

1-D	one-dimensional
2-D	two-dimensional
3-D	three-dimensional
AFM	atomic force microscopy
ALP	alkaline phosphatase
BMMs	bone marrow macrophages
CLC	cholesteryl ester liquid crystal
CT	computed tomography
DAPI	4’,2-diamidino-2-phenylindole
DNA	deoxyribonucleic acid
ECM	extracellular matrix
FWHM	full width at half maximum
GAPDH	glyceraldehyde 3-phosphate dehydrogenase
GMSCs	gingival mesenchymal cells
HAp	hydroxyapatite
HApMPs	hydroxyapatite microparticles
HSV	herpes simplex virus
ICP-MS	inductively-coupled plasma mass spectrometry
KPa	kilopascal
MAPK	mitogen-activated protein kinase
MSCs	mesenchymal stem cells
OCN	osteocalcin

OPG	osteoprotegrin
PBS	phosphate-buffered saline
PCL	polycaprolactone
PBMCs	peripheral blood mononuclear cells
POM	polarized optical micrograph
PTH	parathyroid hormone
qPCR	quantitative polymerase chain reaction
RANKL	receptor activator of NF κB ligand
RFP	red fluorescent protein
RNA	ribonucleic acid
ROS	reactive oxygen species
SEM	scanning electron microscopy
UV	ultraviolet
UV-Vis	ultraviolet-visible spectroscopy
WAXD	wide-angle X-ray diffraction
XPS	X-ray photoelectron spectroscopy
XRD	X-ray diffraction
ZOTeN	zinc oxide tetrapod nanoparticles

ACKNOWLEDGMENTS

I am humbled to have had Professor Paul S. Weiss as my academic advisor, with whom I will also have the pleasure of developing a startup company - Entropic Biosciences, Inc.- based on the research and development under his supervision during my PhD at UCLA.

I would also like to acknowledge our funding for these projects: the Good Food Institute (GFI) Exploratory Grant Program and the UCLA Physical Sciences Entrepreneurship Innovation Fund.

I further recognize the collaborators and colleagues who drove me to think critically during my PhD. Together we have developed numerous technologies to address challenges associated in fields ranging from medicine to materials engineering. I am thankful for the relentless support from long-time colleague Professor Yogendra Mishra, who is always available for scientific discussions and continued support. I am looking forward to future scientific ventures with him. Professor Ali Tamayol and Professor Ali Khademhosseini also deserve special mention: They have guided me throughout much of my bioengineering research and later entrepreneurship.

I sincerely thank all my UCLA undergraduates: Mathews Yi and Matthey Ji, who spearheaded the liquid crystal electrospun nanofibers publications; Lauren Vuong, who leads the bioinspired shoaling biomaterial for personalized medicine; Maximilian Floridia, who has contributed to many projects during his short time in the group; and Ilya Mazalov, who as a high school trainee provided me with constant scientific feedback and curiosity. Finally, I am extremely grateful to my parents Abulghasem and Zohreh. I am humbled to have their love and support during my academic journey.

CURRICULUM VITAE

Education

University of California, Los Angeles, M.S., 2020 *Chemistry*, Los Angeles, CA

Harvard University, Graduate Certificate, 2018 *Bioengineering and Nanotechnology*, Cambridge, MA

University of Florida, B.S., 2014 *Plant Cellular & Molecular Biology*, Gainesville, FL

Grants

The Good Food Institute (GFI) Exploratory Grant Program Title: "Dynamic Organoleptic Scaffolds" $50,000 March 2022-August 2022 Lead PI: **Amir Nasajpour.**

Physical Sciences Entrepreneurship Innovation Fund Title: "Self-Exercising Scaffolds for Cellular Agriculture and Human Health" $100,000 Oct 1, 2022- Sept 30, 2023, Lead PI: Paul S. Weiss Co-PI: **Amir Nasajpour.**

Peer-reviewed Publications

1. "A Nanoengineered Antiviral Fibrous Array with Rose-Inspired Architecture", **Nasajpour, A.**, Samandari, M., Chandrashekhar, P., Abolhassani, R., Suryawanshi, R., Adelung, R., Rubahn, H., Mishra, Y., Khademhosseini, A., Shukla, D., Tamayol, A., and Weiss, P.S., *ACS Materials Letters* 2021, *3*, 1566-1571. **Highlighted** by Nanowerk
2. "Cholesteryl Ester Liquid Crystal Nanofibers for Tissue Engineering Applications", **Nasajpour, A**., Mostafavi, A., Chlanda, A., Rinoldi, C., Sharifi, S., Ji, S., M., Ye, M., Jonas, S.J., Swieszkowski, W., Weiss, P.S., Khademhosseini, A., and Tamayol, A., *ACS Materials Letters* 2020, *2*, 1067-1073.
3. "A Multifunctional Polymeric Periodontal Membrane with Osteogenic and Antibacterial Characteristics", **Nasajpour, A.,** Ansari, A., Rinoldi, C., Shahrokhi-Rad, A., Aghaloo, T., Shin S., Mishra, Y.K., Adelung, R., Swieszkowski, W., Annabi, N., Khademhosseini, A., Moshaverinia, A., and Tamayol, A., *Advanced Functional Materials*. 2018, *28*, 1703437. **Highlighted** by the University of Nebraska-Lincoln
4. "Nanostructured Fibrous Membranes with Rose Spike-Like Architecture", **Nasajpour, A**., Mandla, S., Shree, S., Mostafavi, E., Sharifi, S., Khalilpour, A., Saghazadeh, S., Hassan, S., Mitchell, M.M., Leijten, L., Hou, X., Moshaverinia, A., Annabi N., Adelung R., Mishra Y.K., Shin, S.R., Tamayol, A., and Khademhosseini, A., *Nano Letters* 2017 *17*, 6235-62405.
5. "Gold Nanocomposite Bio-ink for Printing 3D Cardiac Constructs" Zhu, K., Shin, S.R., Kempen, T., Chen, Li. Y., Ponraj, V., **Nasajpour, A.**, Mandla, S., Hu, N., Liu, X., Leijten, J., Lin, Y.-D., Hussain, M., Zhang, Y.Z., Tamayol A., and Khademhosseini, A.,

Advanced Functional Materials 2017, *27*, 1605352.

6. "Micro and Nanotechnologies in Heart Valve Tissue Engineering", Hasan, A., Saliba, J., Modarres, H., Bakhaty, A., **Nasajpour, A.,** Mofrad, R.K., and Sanati-Nezhad, A., *Biomaterials* 2016, *103*, 278-292.
7. "Advancing Tissue Engineering: A Tale of Nano, Micro and Macroscale Integration", Leijten, J., Rouwkema, J., Zhang, Y., **Nasajpour, A.,** Dokmeci, M., and Khademhosseini, A., *Small* 2016, *16*, 2130- 2145.
8. "Tandem Deprotection-Dimerization-Macrocyclization Route to C2 Symmetric Cyclo-Tetrapeptides", Ha, K., Lebedyeva, I., Hamedzadeh, S., Li, Z., Quiñones, R., Pillai, G., Williams, B., **Nasajpour, A.,** Martin, K., Asiric, A.M., and Katritzky, A. R., *Chemistry-A European Journal* 2014, *20*, 4874-4879.
9. "Conformationally Assisted Lactamizations for the Synthesis of Symmetrical and Unsymmetrical Bis- 2,5-Diketopiperazines" Ha, K., Lebedyeva, I., Li, Z., Martin, K., Williams, B., Faby, E., **Nasajpour, A.**, Pillai, G., Al-Youbi, A.O., and Katritzky, A.R., *Journal of Organic Chemistry* 2013, *78*, 8510–8523.

Patents

1) Weiss, P.S., **Nasajpour, A.,** Tamayol, A., Samandari, M. (2022). "A Dynamic Cholesteric Liquid Crystal for Organoid, Spheroid, 3D Cell Aggregative Manufacturing." U.S. Provisional Application No. 63/477,082, filed December 23, 2022 (UCLA TDG Top Tech 2023)

2) **Nasajpour, A.**, Weiss, P.S. (2020). "Devices Comprising a Liquid Crystal Layer and Use Thereof." U.S. World Intellectual Property WO 2022/120120 A1, published June 09, 2022

3) Weiss, P.S., **Nasajpour, A.**, Tamayol, A. (2020). "Liquid Crystal-Based Scaffolds and Use Thereof." U.S. World Intellectual Property WO 2022/020752 A1, published July 27, 2022

Editorial Referee

Scientific Reports	May 2021 – Current
Journal of Applied Physics	March 2021 – Current

Chapter 1

Nature as a Canvas for Inspiration

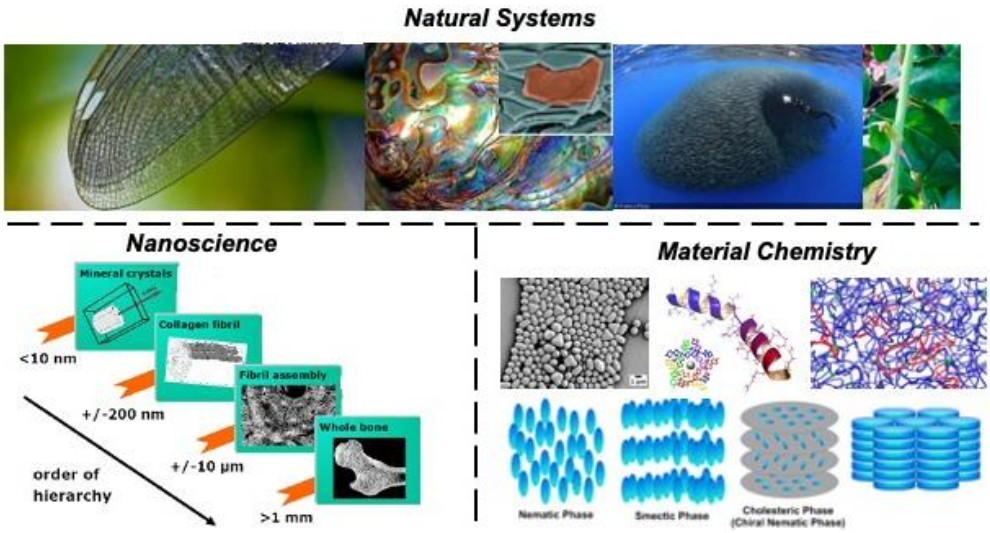

1.1 Introduction

Natural selection is the process by which a species becomes more fit to its environment over time, and this evolutionary mechanism provides scientists with a roadmap to design materials by a "bioinspired approach." Designing such materials requires the understanding of the organism's environment and how it has evolved over time to have the highest likelihood of surviving and reproducing. For instance, naturally occurring liquid crystals in plants have been shown to increase trees' wind tolerance, and corneal liquid crystals in some vertebrates manages internal eye pressure.[1,2] Scientists use this understanding to reverse engineer such materials found in nature to address societal challenges.[3] An example is reverse engineering the photosystem II enzyme found in plants to create more efficient light-harvesting systems for energy. Another well-studied example involves sedentary aquatic-based organisms, who deploy polypeptide coacervates in salt-rich environments in order to adhere to porous, rough surfaces. The chemistry leading to this adhesive behavior has led to inspiration for biomedical-based adhesives, many of which are being commercialized.

In Chapter 2, I begin this thesis by describing cholesteryl ester liquid crystal scaffolding technology based on a defense mechanism in shoaling fish, in which single entities assemble and congregate into one large entity. Natural advantages of this behavior include hydrodynamic efficacy, reproductive enhancement, and predator avoidance. I reverse engineer this assembly process from a bottom-up approach using molecules that assemble into large supramolecular structures. I highlight the usage of this material in electrospun nanofibers and its advantages in orchestrating muscle cell differentiation. Using the materials developed in my doctoral research, I describe a method to orchestrate 3D cellular organoid organization from a 2D monolayer. In this process, the mechanical twisting from the biomaterial directs and stacks the cells into 3D

aggregates in less than one day in cell culture.[4]

Next, in Chapter 3, I introduce a rose-inspired nonwoven fiber array. In addition to discussing the advantages of the composites, I provide a broad overview of the design process where I introduce 3D zinc oxide nanomaterials and the electrospinning processing required for the fiber development. I discuss the rose-inspired fiber's ability to generate hydrogen peroxide off the surface of the nanomaterial's catalytic surface, which has beneficial consequences in treating herpes and in mitigating the spread of COVID-19.[5]

In Chapter 4, we use the multimineral composition found in teeth as inspiration for artificial enamel. Realizing the strength that different minerals impart to teeth, we designed our enamel with both hydroxyapatite and whitlockite. I describe how I designed an osteogenic niche comprised of a commercially modified alginate hydrogel and whitlockite microparticles with properties that can direct osteogenesis of human gingival mesenchymal stem cells.[6,7] We conducted *in vivo* studies on these mesenchymal stem cells, which promoted bone repair in calvarial defects in murine models. Our results confirmed the development of a promising treatment modality for craniofacial bone regeneration based on an injectable growth factor-free hydrogel delivery system.

Finally, in my conclusions in Chapter 5, I highlight current challenges and future opportunities for using the bioinspired material as a life science tool to be provided by Entropic Biosciences, Inc.[8]

References

1. Mitov, M. Cholesteric Liquid Crystals in Living Matter. *Soft Matter* **2017,** *13*, 4176-4209.

2. Jewell, S. A. Living Systems and Liquid Crystals. *Liq. Cryst.* **2011,** *38*, 1699-1714.

3. Tibbitt, M. W.; Langer, R. Living Biomaterials. *Acc. Chem. Res.* **2017,** *50*, 508-513.

4. Nasajpour, A.; Mostafavi, A.; Chlanda, A.; Rinoldi, C.; Sharifi, S.; Ji, M. S.; Ye, M.; Jonas, S. J.; Swieszkowski, W.; Weiss, P. S.; Khademhosseini, A.; Tamayol, A. Cholesteryl Ester Liquid Crystal Nanofibers for Tissue Engineering Applications. *ACS Mater. Lett*. **2020**, *2*, 1067–1073.

5. Nasajpour, A.; Samandari, M.; Patil, C. D.; Abolhassani, R.; Suryawanshi, R. K.; Adelung, R.; Rubahn, H.-G.; Khademhosseini, A.; Mishra, Y. K.; Shukla, D.; Tamayol, A.; Weiss, P. S. Nanoengineered Antiviral Fibrous Arrays with Rose-Thorn-Inspired Architectures. *ACS Mater. Lett*. **2021**, *3*, 1566–1571.

6. Wegst, U.; Bai, H.; Saiz, E.; et al. Bioinspired Structural Materials. *Nature Mater*. **2015**, *14*, 23-26.

7. Dai, H.; Dai, W.; Hu, Z.; Zhang, W.; Zhang, G.; Guo, R. Advanced Composites Inspired by Biological Structures and Functions in Nature: Architecture Design, Strengthening Mechanisms, and Mechanical-Functional Responses. *Adv. Sci*. **2023**, *10*, 2207192-2207227.

8. Pouraghaei Sevari, S.; Kim, J. K.; Chen, C.; Nasajpour, A.; Wang, C.-Y.; Krebsbach, P. H.; Khademhosseini, A.; Ansari, S.; Weiss, P. S.; Moshaverinia, A. Whitlockite-Enabled Hydrogel for Craniofacial Bone Regeneration. *ACS Appl. Mater. Interfaces* **2021**, *13*, 35342–35355.

Chapter 2

Cholesteryl Ester Liquid Crystal Nanofibers for Tissue Engineering Applications

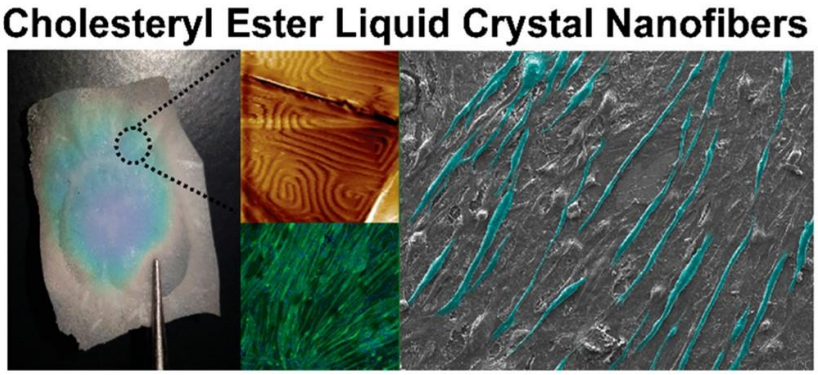

The information in this chapter was published in *ACS Materials Letters*, **2020**, *2*, 1067–1073 and has been reproduced with permission from the authors.

"Cholesteryl Ester Liquid Crystal Nanofibers for Tissue Engineering Applications", Nasajpour, A., Mostafavi, A., Chlanda, A., Rinoldi, C., Sharifi, S., Ji, S., M., Ye, M., Jonas, J., S., Swieszkowski, W., Weiss, P., S., Khademhosseini, A., and Tamayol, A., *ACS Materials Letters*, **2020**, *2*, 1067–1073

2.1 Abstract

Liquid-crystal-based biomaterials provide promising platforms for the development of dynamic and responsive interfaces for tissue engineering. Cholesteryl ester liquid crystals (CLCs) are particularly well suited for these applications, due to their roles in cellular homeostasis and their intrinsic ability to organize into supramolecular helical structures that reflect light in a reversible manner at a critical phase transition temperature. Here, we develop a nonwoven CLC electrospun scaffold by dispersing three cholesteryl ester-based mesogens within polycaprolactone (PCL). We tuned the ratio of our CLC mesogens to achieve a phase transition at the cell culture incubator temperature of 37 °C. In these scaffolds, the PCL provides structural integrity while the homogenously dispersed CLCs adopts a helical structure with its axis parallel to the surface, causing the mesogens to alternate between homeotropic and planar alignments. This alternating orientation can give rise to fingerprint-like striations that establish a dynamic interface, which mimic the hierarchical and dynamic structures found within the native extracellular matrix in skeletal muscle tissue. Using atomic force microscopy, as well immunochemistry, we found that these fingerprint-like striations led to greater myoblast adhesion strength, shortened differentiation times, and overall enhanced myofibril formation in vitro compared to the tested control counterparts.

2.2 Introduction

The liquid crystalline (LC) phase shares properties seen in both liquids and solids. Historically, LC-based materials have been applied in commercial applications with great success, such as in the development of Kevlar® body armor and the fabrication of modern liquid crystal displays.[1] More recently, LCs have been used to mimic various biological processes, ranging from epithelial tissue organization, bacterial biofilm formation, and the assembly of many biologically

derived materials.[2-6] The engineering of LC biomaterials is poised to overcome challenges that have thus far precluded the ability to recreate the hierarchical as well viscoelastic behavior of native extracellular matrix (ECM).[7-9]

A key challenge to the incorporation of LCs into tissue engineering substrates is the cytotoxicity associated with most commercially available LC mesogens. To date, cholesteryl ester liquid crystals (CLCs) have been a largely overlooked class of mesogens, even though they play key roles in modulating/stabilizing cell membranes, maintaining cellular homeostasis, and regulating signaling processes. These properties make CLCs attractive candidates for tissue engineering applications.[10] Stupp and co-workers showed that poly(lactic acid) scaffolds with covalently bound cholesterol moieties promote the adhesion, migration, and proliferation of 3T3 fibroblasts.[11] Films of LC-based elastomers and networks have also been used to create three-dimensional (3D) porous scaffolds that promote the proliferation and function of muscle and cardiac cells.[12-14] In a notable study, mouse myoblast cells (C2C12s) encapsulated within injectable peptide amphiphile liquid crystal scaffolds maintained their proliferation, differentiation, and maturation potentials in both *in vitro* and *in vivo* (murine) models.[15] However, these LC-based scaffolds were not load-bearing nor free standing. In addition, the peptides used required complex syntheses, which could limit the use of the materials by other groups.

2.3 Methods and Discussion

CIn this study, we electrospun a nonwoven cholesteryl ester liquid crystal scaffold (CLC-S) by dispersing cholesteryl oleyl carbonate, cholesteryl pelargonate, and cholesteryl benzoate within polycaprolactone (PCL). By using a known ratio of the *cis*-unsaturated fatty acids cholesteryl oleyl carbonate to the cholesteryl pelargonate found in Table 2.1 and Figure S2.1, we assemble a mesophase phase in the range to 36-40 °C, which coincides with the temperature of the

cell culture incubator; the melting temperature of the liquid crystal mixture increases with the percent composition of cholesteryl pelargonate due to the more efficient packing of saturated fatty acids.[16] Others have shown cholesteric liquid crystals can control the patterning and assembly of nanoparticles at fluid interfaces due to surface patterns created from the alternating anchoring conditions of the CLC.[17,18] We speculate that these topographical and frustrated states can be used to stimulate the culture cells using the pitch of the CLC. This stimulation could shorten the time needed for differentiation.

Table 2.1 Cholesteryl ester liquid crystal scaffold (CLC-S) composition used in this study. To generate the cholesteryl ester liquid crystal (CLC) mixtures for our electrospun scaffolds, we dispersed reported CLC compositions for the varying tested CLC-S conditions in a 4 mL azeotropic solvent mixture of chloroform:dimethylformamide (3:1).

Composition	PCL	Cholesteryl oleyl carbonate	Cholesteryl pelargonate	Cholesteryl benzoate
15% (w/v) PCL	**600 mg**			
25% (w/v) CLC-S	**600 mg**	**320 mg**	**580 mg**	**100 mg**
37% (w/v) CLC-S	**600 mg**	**480 mg**	**870 mg**	**150 mg**
50% (w/v) CLC-S	**600 mg**	**640 mg**	**1160 mg**	**200 mg**

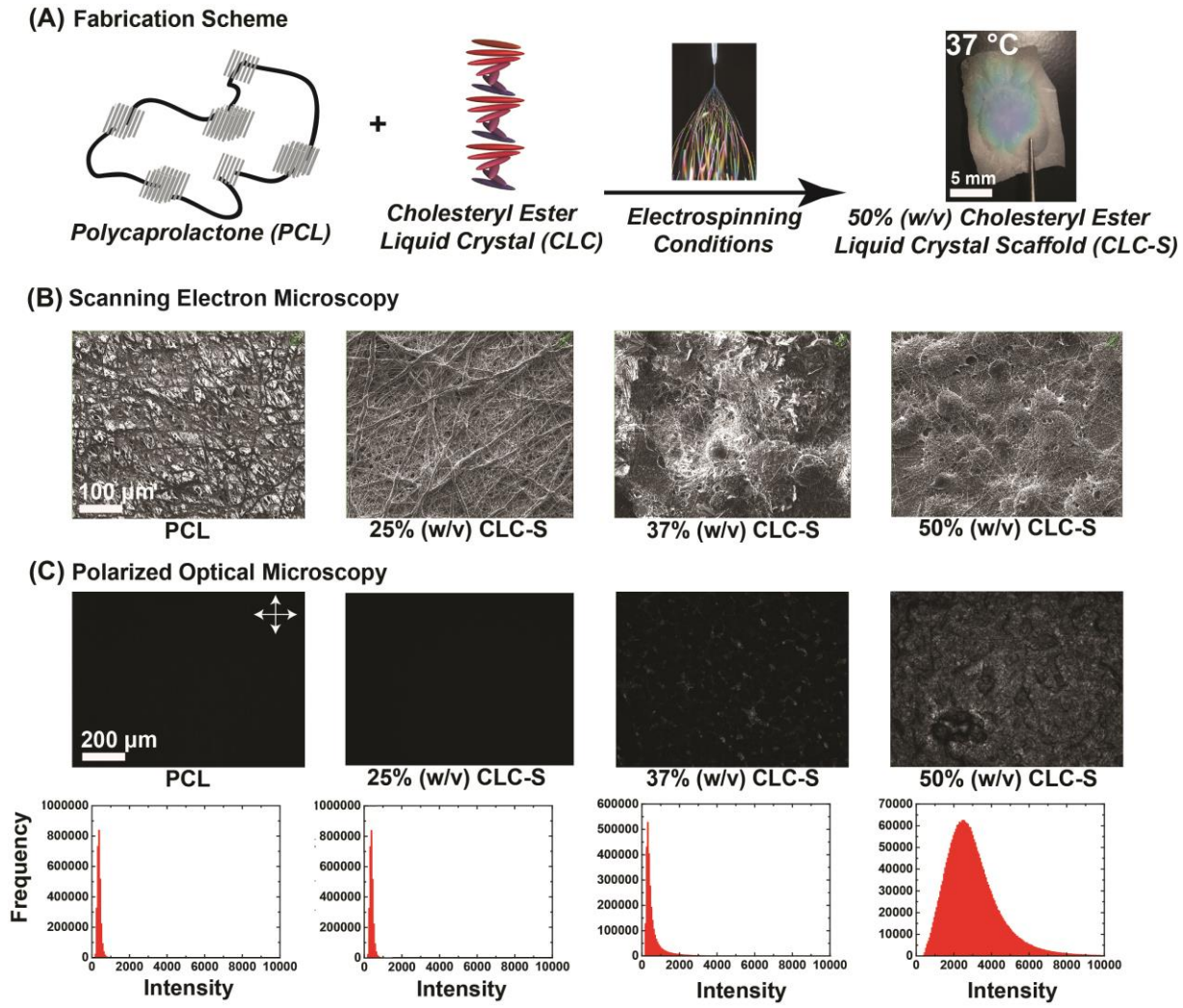

Figure 2.1. Microscopic investigation of cholesteryl ester liquid crystal scaffolds (CLC-S). **(A)** Fabrication scheme for the electrospun CLC-S: A 15% weight per volume (w/v) polycaprolactone (PCL) solution with cholesteryl ester liquid crystal mesogens of varying concentrations were electrospun. (**B**) Scanning electron microscopy images of the PCL-only scaffold, 25% (w/v) CLC-S, 37% (w/v) CLC-S, 50% (w/v) CLC-S. (**C**) Polarized optical micrograph (POM) imaging of the CLC-S condition and accompanying frequency-intensity plots.

To test this hypothesis, after physicochemical characterization of the scaffolds, we cultured C2C12s on our CLC-S and characterized their growth and development *via* immunohistochemistry and atomic force microscopy (AFM). Our CLC-S was fabricated *via* conventional electrospinning and was designed to dynamically stimulate cultured cells, providing a biomimetic native skeletal muscle ECM (Figure 2.1A). The CLC-S was electrospun with a 15% (w/v) solution of PCL and

varying weight per volume fractions of CLC (Table 2.1). The electrospinning flow rate and electrical field were adjusted to ensure the formation of a fibrous scaffold.[19-21] The CLC-S with the highest CLC concentration (50% w/v) reflected light off the scaffold when heated to 37 °C as opposed to a typical opaque nanofiber (*i.e.*, PCL control) (Figures 2.1A and S2.2). UV-Vis spectroscopy demonstrated that the pristine PCL controls had an opaque spectrum. Samples with CLC (*i.e.*, pristine CLC and 50% (w/v) CLC-S) had similar overall optical reflection profiles. However, the 50% (w/v) CLC-S was slightly blueshifted compared with the pristine CLC.

To investigate the microscopic features of the CLC-S further, we imaged them using scanning electron microscopy (SEM) (Figure 2.1B). The control PCL-only scaffolds appeared as a typical fibrous electrospun scaffold. However, the CLC-S with varying concentrations of CLC demonstrated different structural characteristics than their PCL-only counterparts. For example, the 25% (w/v) CLC-S formed distinct web-like features. Similarly, when increasing the CLC concentration to 50% (w/v), the generated CLC-S exhibited large regions of aggregation that formed bead-on-string like morphologies within the PCL polymer network (Figure 2.1B).

To test the encapsulation and functionality of the CLC within PCL network, polarized optical microscopy (POM) was used to measure the light polarizing properties of the CLC-S that are characteristic of CLCs. The CLC-S were first heated to the thermotropic CLC phase transition temperature of 36-40 °C using a custom-built microscope mount heater. While acquiring the 50% (w/v) CLC-S POM micrograph, we observed large regions of birefringent texture polarization across the scaffold (Figure 2.1C). These textures were likely due to the confinement of CLC within the PCL polymeric web. These results were consistent with our previous findings shown in Figures 2.1B and S2.2.

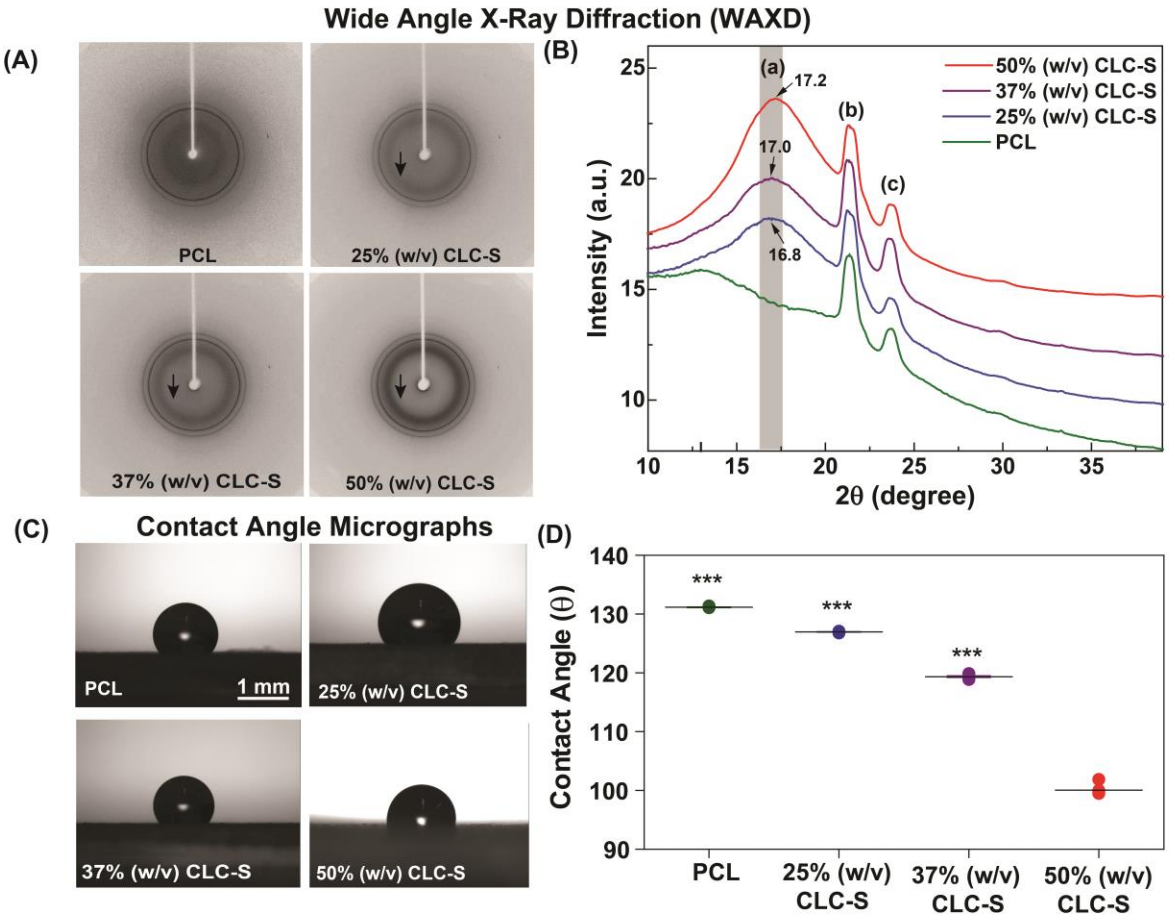

Figure 2.2. Wide angle X-ray diffraction (WAXD) patterns and hydrophilicity of the cholesteryl ester liquid crystal scaffolds (CLC-S). (**A**) Fiber diffraction patterns obtained for the scaffolds with varying cholesteryl ester liquid crystal concentrations. Broad reflection bands are annotated with black arrows within the micrographs of the CLC-S, showing a gradual move to higher θ and reflection sharpening. (**B**) Two-dimensional scattering intensity versus 2θ for each scaffold. (**C**) Contact angle micrographs for each scaffold. (**D**) Plot of measured contact angle values for each scaffold. The contact angles of the polycaprolactone (PCL)-only scaffold, 25% (w/v) CLC-S, and 37% (w/v) CLC-S were found to be significantly different from the 50% (w/v) CLC-S (n=6 for contact angle measurements, ***: P <0.001).

Wide-angle X-ray diffraction further illustrated the incorporation of the CLC within the semi-crystalline PCL mesh (Figures 2.2A and 2.2B). In the CLC samples, diffuse reflection bands were observed at 2θ = 16.8-17.2^{o}, which were similar to what others have reported.[22] However, these diffuse reflection bands were not present in the pristine PCL scaffolds. As shown in the micrographs in Figures 2.2A and subsequent plots in 2.2B, gradually increasing the CLC

concentration (*i.e.*, from 25-50% w/v) shifts the reflection band from 2θ = 16.8 ^{o} to 2θ = 17.2^{o}. This shift suggests that an increase in the CLC concentration leads to a decrease in the *d*-spacing of the CLC (from 5.27 Å to 5.15 Å) in the prepared scaffolds. Moreover, increasing the CLC concentration in the scaffold caused a substantial sharpening of the reflection from a full width at half maximum of FWHM = 6.7^{o} to FWHM = 4.6^{o}. This sharpening suggests that increasing the CLC concentration leads to weaker anchoring, allowing for greater overall molecular ordering.[17]

Contact angle measurements were performed to evaluate the overall hydrophilicity of the CLC-S. Our results showed that increasing the concentration of the CLC renders the scaffold more hydrophilic (Figure 2.2C, D), creating favorable interfaces for cellular attachment and growth.[23-25]

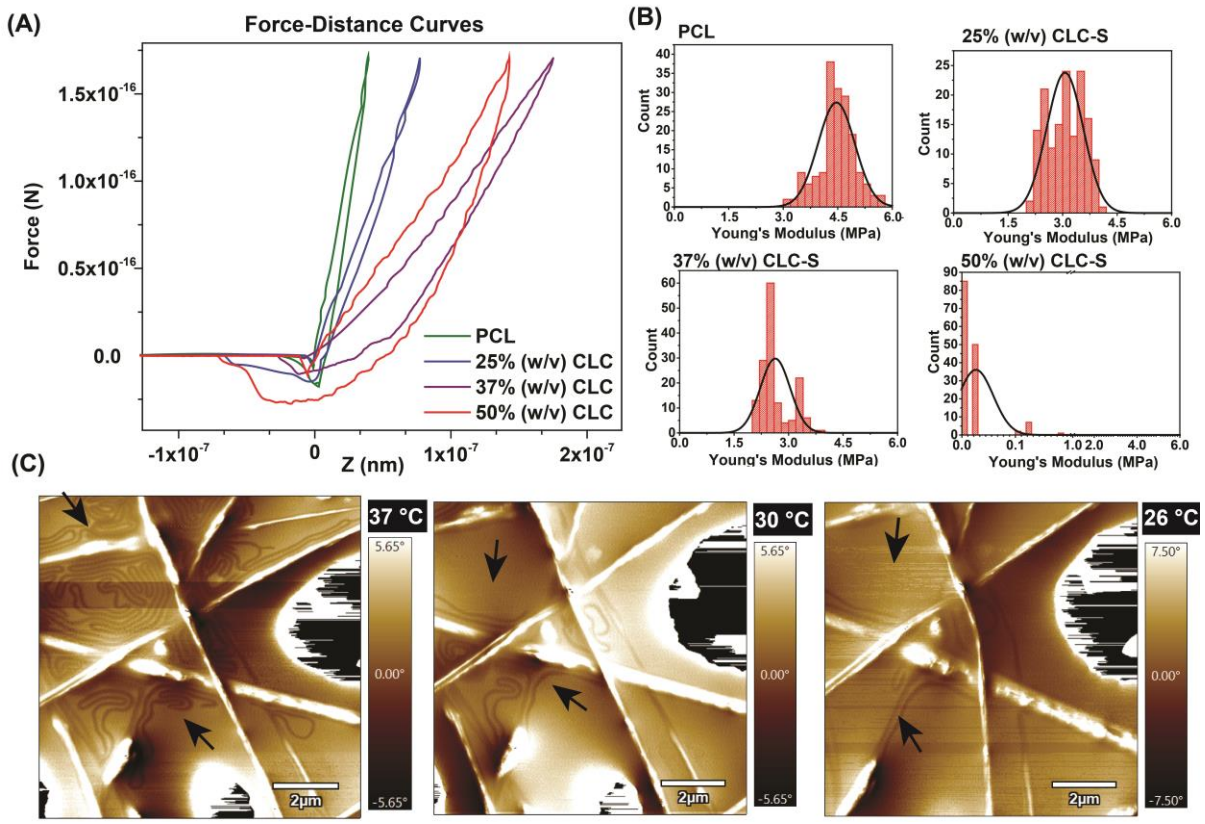

Figure 2.3. Surface and mechanical characterization of the cholesteryl ester liquid crystal scaffold (CLC-S). (A) Force-distance curves of the tested scaffolds with atomic force microscopy (AFM). **(B)** Nanoindentation using AFM shows that the Young's moduli of the scaffolds decreased with increasing concentration of cholesteryl ester liquid crystal (CLC). The 50% (w/v) CLC-S displayed Young's moduli on the kPa scale, 3 orders of magnitude lower than that of the PCL-only scaffold. **(C)** The 50% (w/v) CLC-S was heated to 37 °C then cooled to room temperature. Temperature controlled AFM phase contrast imaging of depicts fingerprint-like striations under homeotropic anchoring conditions at our engineered phase transition temperature.

We probed the CLC-S with AFM to understand the scaffold's mechanical properties at the bio-interface (Figure 2.3A, B) as well its thermoresponsive topographical behavior (Figures 2.3C, S2.5, and S2.6). Based on our force-distance curves obtained by AFM, we predominantly found elastic deformation profiles for all the tested scaffolds except those for 50% (w/v) CLC-S, which showed a viscoelastic deformation profile (Figure 2.3A). The PCL-only scaffold, 25% (w/v) CLC-S, and 37% (w/v) CLC-S were relatively elastic and were found to be less stiff with increasing CLC concentration (Figure 2.3B). Interestingly, the 50% (w/v) CLC-S had Young's

moduli ranging from 3-16 kPa, mimicking the native skeletal muscle cell ECM (Figure 2.3C). The bulk tensile mechanical properties of the generated scaffolds were also tested with Instron measurements. There was no compromise in bulk properties upon increasing CLC concentration, making it suitable for possible surgical grafting applications not possible in the pristine CLCs (Figure S2.4).[26] Upon scanning the PCL-only scaffold, we found a lamellar morphology expected of pure PCL. The 50% (w/v) CLC-S had a non-confined layer of phase-separated CLC that gave rise to fingerprint-like striations upon heating to 37 °C (Figures 2.3C, S2.5, and S2.6).[27] These CLC-S mechanical properties can mimic the viscoelastic behavior seen in the ECM as well hierarchical organization found in skeletal muscle tissue.[28]

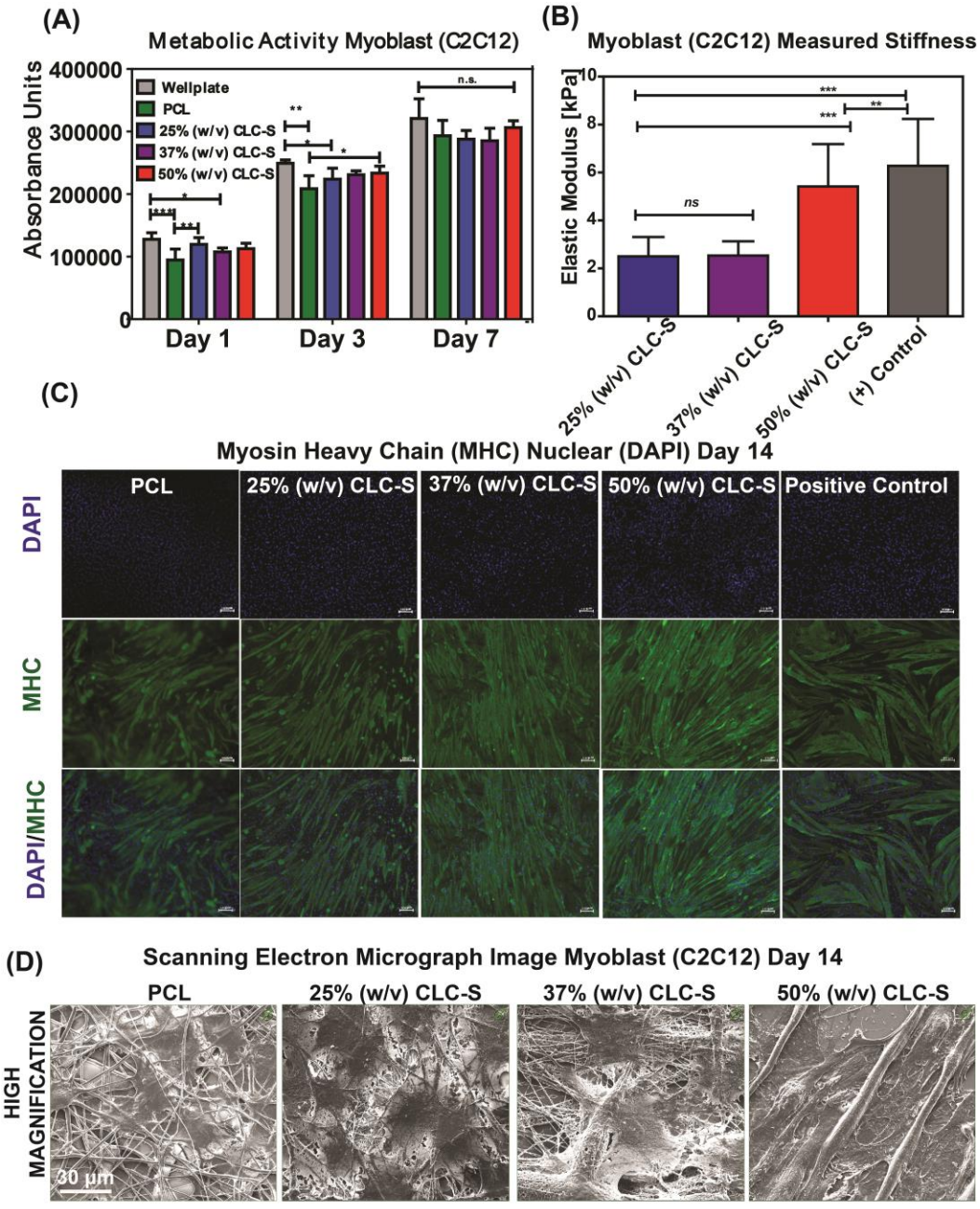

Figure 2.4. ***In vitro*** **biocompatibility of muscle cells with cholesteryl ester liquid crystal scaffolds (CLC-S)**. **(A)** Presto Blue analysis (metabolic analysis) of the skeletal muscle cells (C2C12) cultured over 7 days. **(B)** Atomic force microscopy measurements of cellular stiffness on tested scaffolds. **(C)** Immunohistochemistry with myosin heavy chain and 4′,6-diamidino-2-phenylindole (DAPI) of C2C12s cultured on scaffolds with various concentrations of cholesteryl ester liquid crystal (CLC) at days 7 and 14. **(D)** Scanning electron microscopy images showing the morphology of the cultured C2C12s on scaffolds with various concentrations of CLC at 14 days post differentiation. (n=6 for C2C12 metabolic activity assays, n=4 for elastic modulus measurements, **: $P < 0.01$, ***: $P < 0.001$

Dynamic materials have recently attracted significant attention for engineering advanced, smart biomedical systems.[29,30] To evaluate the suitability of the engineered CLC-S as tissue engineering scaffolds, we cultured C2C12s on them. The biocompatibility of the CLC-S was analyzed using a cell viability assay kit on days 1 and 3 of cell culture (Figure 2.4A). The number of cells adhered to the CLC-S increased with CLC concentration and remained viable (Figure S2.7). The 50% (w/v) CLC-S resulted in the formation of confluent cellular layers, while the PCL-only scaffold poorly supported cellular adhesion (Figure S2.7). The trend was expected due to the hydrophobicity of the scaffolds with lower CLC weight per volume fraction (Figures 2.2C, D). We measured the elastic moduli of the muscle cells adhered to the scaffolds. We found the elastic modulus of the cells on the 50% (w/v) CLC-S were significantly higher than those of the pure PCL scaffolds (Figure 2.4C). These elasticity measurements indicated that the presence of CLC significantly influenced cellular adhesion and mechano-signal transduction. We speculate that this mechanical interaction could lead to higher integrin binding activity, remodeling of the actin cytoskeleton, and therefore modulation of cell stiffness. It has been demonstrated that changes in actin filaments due to the application of dynamic loads can affect cellular organization and growth.[31]

Cellular organization and cytoskeletal arrangement of the cultured cells were then examined by F-actin staining on both day 7 and day 14 post-differentiation. Figure S2.9 shows a homogeneous cell distribution over all scaffolds and deeper cellular infiltration with increasing CLC concentration. The F-actin staining data suggest that the addition of CLC not only created a suitable environment for cellular attachment but also stimulated cellular infiltration, enabling the formation of 3D-like cellular networks. Myoblast differentiation to myotubes were confirmed by immunostaining against myosin heavy chains. Immunohistochemical analysis showed that

myoblasts seeded on the 50% and 37% (w/v) CLC-S on day 14 exhibited formation of multinucleated elongated myotubes with positive myosin heavy chain expression (Figure 2.4C). The myotubes' formation on the PCL-only scaffold and the 25% (w/v) CLC-S was considerably lower than the two other scaffolds, indicating that many myoblasts (stained nuclei) failed to differentiate, resulting in incomplete myotube formation. Figure 2.4D shows SEM images of the scaffolds cultured with C2C12 at 7 days post differentiation. At 50% (w/v) CLC-S, elongated myotubes were formed, indicative of cellular organization, despite the random alignment of the scaffold. The thickness of these myotubes had a direct relationship with the CLC concentration (Figures 2.4D and S2.10). Overall, it appears that the combination of better mechanical properties, the biomimetic chemical composition, and the dynamic interface of the CLC-S facilitated the cellular adhesion, proliferation, differentiation, and eventually organization. However, to draw definite conclusions, more in-depth multiscale analyses and studies with experimental animal models should be carried out.

2.4 Conclusions and Prospects

In summary, we developed a dynamic thermotropic cholesteryl ester liquid crystal scaffold with hierarchical architecture, mechanical properties, and great potential for growing skeletal muscle tissues. The advantages of our scaffold are its simplicity, biocompatibility, and robust mechanical properties, which can promote C2C12 cellular proliferation and differentiation. While being strong enough to withstand surgical procedures, the scaffolds offer local and interfacial Young's moduli like those of native muscle ECM. Collectively, this work demonstrates a promising and useful synthetically engineered active biomaterial, which enables the growth of myoblasts and their differentiation to myotubes. These active materials can self-assemble and promote cellular adhesion, proliferation, and differentiation offering new opportunities to advance

muscle tissue engineering. We anticipate that the use of fully synthetic scaffolds can open the door to medical applications beyond tissue engineering.

References

1. Andrienko, D. Introduction to Liquid Crystals. *J. Mol. Liq.* **2018,** *267*, 520-541.

2. Saw, T. B.; Doostmohammadi, A.; Nier, V.; Kocgozlu, L.; Thampi, S.; Toyama, Y.; Marcq, P.; Lim, C. T.; Yeomans, J. M.; Ladoux, B. Topological Defects in Epithelia Govern Cell Death and Extrusion. *Nature* **2017,** *544*, 212-216.

3. Pérez-González, C.; Alert, R.; Blanch-Mercader, C.; Gómez-González, M.; Kolodziej, T.; Bazellieres, E.; Casademunt, J.; Trepat, X. Active Wetting of Epithelial Tissues. *Nat. Phys.* **2019,** *15*, 79-88.

4. Patteson, A. E.; Gopinath, A.; Arratia, P. E. The Propagation of Active-Passive Interfaces in Bacterial Swarms. *Nat. Commun.* **2018,** *9*, 5373.

5. Mitov, M. Cholesteric Liquid Crystals in Living Matter. *Soft Matter* **2017,** *13*, 4176-4209.

6. Jewell, S. A. Living Systems and Liquid Crystals. *Liq. Cryst.* **2011,** *38*, 1699-1714.

7. Tibbitt, M. W.; Langer, R. Living Biomaterials. *Acc. Chem. Res.* **2017,** *50*, 508-513.

8. Martella, D.; Parmeggiani, C. Advances in Cell Scaffolds for Tissue Engineering: The Value of Liquid Crystalline Elastomers. *Chem.: Eur. J.* **2018,** *24*, 12206-12220.

9. Mohamed, M. A.; Fallahi, A.; El-Sokkary, A. M. A.; Salehi, S.; Akl, M. A.; Jafari, A.; Tamayol, A.; Fenniri, H.; Khademhosseini, A.; Andreadis, S. T.; Cheng, C. Stimuli-Responsive Hydrogels for Manipulation of Cell Microenvironment: From Chemistry to Biofabrication Technology. *Prog. Polym. Sci.* **2019,** *98*, 101147.

10. Maxfield, F. R.; Tabas, I. Role of Cholesterol and Lipid Organization in Disease. *Nature* **2005,** *438*, 612-621.

11. Hwang, J. J.; Iyer, S. N.; Li, L.-S.; Claussen, R.; Harrington, D. A.; Stupp, S. I. Self-Assembling Biomaterials: Liquid Crystal Phases of Cholesteryl oligo(l-lactic acid) and Their Interactions with Cells. *Proc. Natl. Acad. Sci. U.S.A.* **2002,** *99*, 9662-9667.

12. Gao, Y.; Mori, T.; Manning, S.; Zhao, Y.; Nielsen, A. D.; Neshat, A.; Sharma, A.; Mahnen, C. J.; Everson, H. R.; Crotty, S.; Clements, R. J.; Malcuit, C.; Hegmann, E. Liquid Crystal Elastomer Foams with Elastic Properties Specifically Engineered as Biodegradable Brain Tissue Scaffolds. *ACS Macro Lett.* **2016,** *5*, 4-9.

13. Ferrantini, C.; Pioner Josè, M.; Martella, D.; Coppini, R.; Piroddi, N.; Paoli, P.; Calamai, M.; Pavone Francesco, S.; Wiersma Diederik, S.; Tesi, C.; Cerbai, E.; Poggesi, C.; Sacconi, L.; Parmeggiani, C. Development of Light-Responsive Liquid Crystalline Elastomers to Assist Cardiac Contraction. *Circ. Res*. **2019,** *124*, e44-e54.

14. Martella, D.; Pattelli, L.; Matassini, C.; Ridi, F.; Bonini, M.; Paoli, P.; Baglioni, P.; Wiersma, D. S.; Parmeggiani, C. Liquid Crystal-Induced Myoblast Alignment. *Adv. Healthc. Mater.* **2019,**

8, 1801489.

15. Sleep, E.; Cosgrove, B. D.; McClendon, M. T.; Preslar, A. T.; Chen, C. H.; Sangji, M. H.; Pérez, C. M. R.; Haynes, R. D.; Meade, T. J.; Blau, H. M.; Stupp, S. I. Injectable Biomimetic Liquid Crystalline Scaffolds Enhance Muscle Stem Cell Transplantation. *Proc. Natl. Acad. Sci. U.S.A* **2017,** *114*, E7919-E7928.

16. Van Hecke, R. G.; Karukstis, K. K.; Li H.; Hendargo, C. H.; Cosand, J. A.; Fox, M. M. Synthesis and Physical Properties of Liquid Crystals: An Interdisciplinary Experiment *J. Chem. Educ.* **2005,** *82*, 9, 1349.

17. Tran, L.; Bishop, K. J. M. Swelling Cholesteric Liquid Crystal Shells to Direct the Assembly of Particles at the Interface. *ACS Nano* **2020**, *14*.

18. Tran, L.; Lavrentovich, M. O.; Durey, G.; Darmon, A.; Haase, M. F.; Li, N.; Lee, D.; Stebe, K. J.; Kamien, R. D.; Lopez-Leon, T. Change in Stripes for Cholesteric Shells via Anchoring in Moderation. *Phys. Rev. X*. **2017**, 7, 167.

19. Nasajpour, A.; Ansari, S.; Rinoldi, C.; Rad, A. S.; Aghaloo, T.; Shin, S. R.; Mishra, Y. K.; Adelung, R.; Swieszkowski, W.; Annabi, N.; Khademhosseini, A.; Moshaverinia, A.; Tamayol, A. A Multifunctional Polymeric Periodontal Membrane with Osteogenic and Antibacterial Characteristics. *Adv. Funct. Mater.* **2018,** *28*, 1703437.

20. Nasajpour, A.; Mandla, S.; Shree, S.; Mostafavi, E.; Sharifi, R.; Khalilpour, A.; Saghazadeh, S.; Hassan, S.; Mitchell, M. J.; Leijten, J.; Hou, X.; Moshaverinia, A.; Annabi, N.; Adelung, R.; Mishra, Y. K.; Shin, S. R.; Tamayol, A.; Khademhosseini, A. Nanostructured Fibrous Membranes with Rose Spike-Like Architecture. *Nano Lett.* **2017,** *17*, 6235-6240.

21. Khalili, S.; Khorasani, S. N.; Razavi, S. M.; Hashemibeni, B.; Tamayol, A. Nanofibrous Scaffolds with Biomimetic Composition for Skin Regeneration. *Appl. Biochem. Biotechnol*. **2019,** *187*, 1193-1203.

22. Krigbaum, W. R.; Watanabe, J.; Ishikawa, T. Thermotropic Polyesters. 2. Investigation of the Mesophase Properties of Polymers Based on 4,4'-Dihydroxybiphenyl. *Macromolecules* **1983,** *16*, 1271-1279.

23. Ostuni, E.; Chapman, R. G.; Liang, M. N.; Meluleni, G.; Pier, G.; Ingber, D. E.; Whitesides, G. M. Self-Assembled Monolayers That Resist the Adsorption of Proteins and the Adhesion of Bacterial and Mammalian Cells *Langmuir* **2001,** *17*, 6336-6343.

24. Dowling, D. P.; Miller, I. S.; Ardhaoui, M.; Gallagher, W. M. Effect of Surface Wettability and Topography on the Adhesion of Osteosarcoma Cells on Plasma-Modified Polystyrene. *J. Biomater. Appl.* **2010,** *26*, 327-347.

25. Liu, D.; Liu, L.; Onck, P. R.; Broer, D. J. Reverse Switching of Surface Roughness in a Self-Organized Polydomain Liquid Crystal Coating. *Proc. Natl. Acad. Sci. U.S.A* **2015,** *112*, 3880-3885.

26. Ostrovidov, S.; Salehi, S.; Costantini, M.; Suthiwanich, K.; Ebrahimi, M.; Sadeghian, R. B.; Fujie, T.; Shi, X.; Cannata, S.; Gargioli, C.; Tamayol, A.; Dokmeci, M. R.; Orive, G.; Swieszkowski, W.; Khademhosseini, A. 3D Bioprinting in Skeletal Muscle Tissue Engineering. *Small* **2019,** *15*, 1805530.

27. Liu, D.; Broer, D. J. Self-Assembled Dynamic 3D Fingerprints in Liquid-Crystal Coatings Towards Controllable Friction and Adhesion. *Angew. Chem. Int. Ed.* **2014,** *53*, 4542-4546.

28. Ghosh, K.; Pan, Z.; Guan, E.; Ge, S.; Liu, Y.; Nakamura, T.; Ren, X.-D.; Rafailovich, M.; Clark, R. A. F. Cell Adaptation to a Physiologically Relevant ECM Mimic with Different Viscoelastic Properties. *Biomaterials* **2007,** *28*, 671-679.

29. Derakhshandeh, H.; Kashaf, S. S.; Aghabaglou, F.; Ghanavati, I. O.; Tamayol, A. Smart Bandages: The Future of Wound Care. *Trends Biotechnol.* **2018,** *36*, 1259-1274.

30. Saghazadeh, S.; Rinoldi, C.; Schot, M.; Kashaf, S. S.; Sharifi, F.; Jalilian, E.; Nuutila, K.; Giatsidis, G.; Mostafalu, P.; Derakhshandeh, H.; Yue, K.; Swieszkowski, W.; Memic, A.; Tamayol, A.; Khademhosseini, A. Drug Delivery Systems and Materials for Wound Healing Applications. *Adv. Drug Deliv. Rev.* **2018,** *127*, 138-166.

31. Samandari, M.; Abrinia, K.; Mokhtari-Dizaji, M.; Tamayol, A. Ultrasound Induced Strain Cytoskeleton Rearrangement: An Experimental and Simulation Study. *J. Biomech.* **2017,** *60*, 39-47.

Supplementary Figures

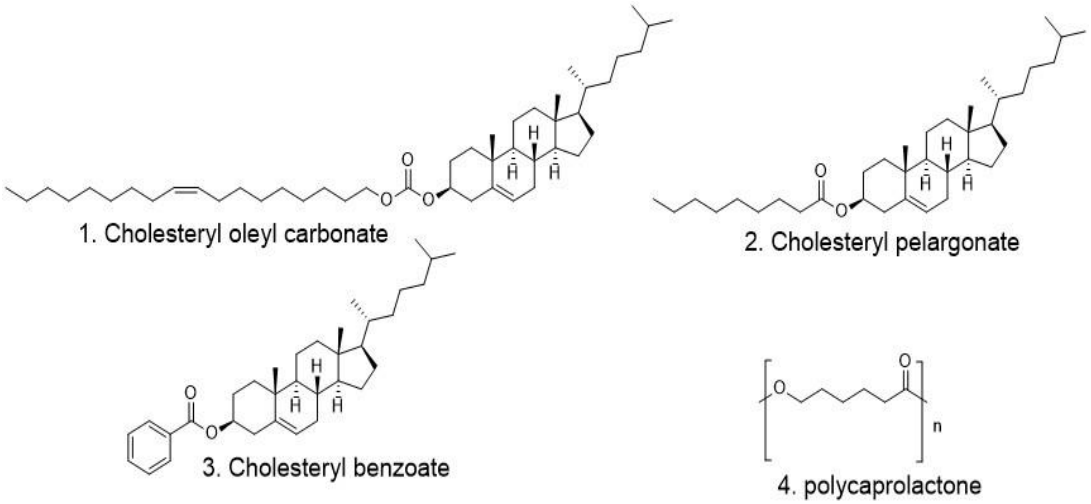

Figure S2.1. Chemical structures of compounds used in fabrication of the cholesteryl ester liquid crystal scaffolds.

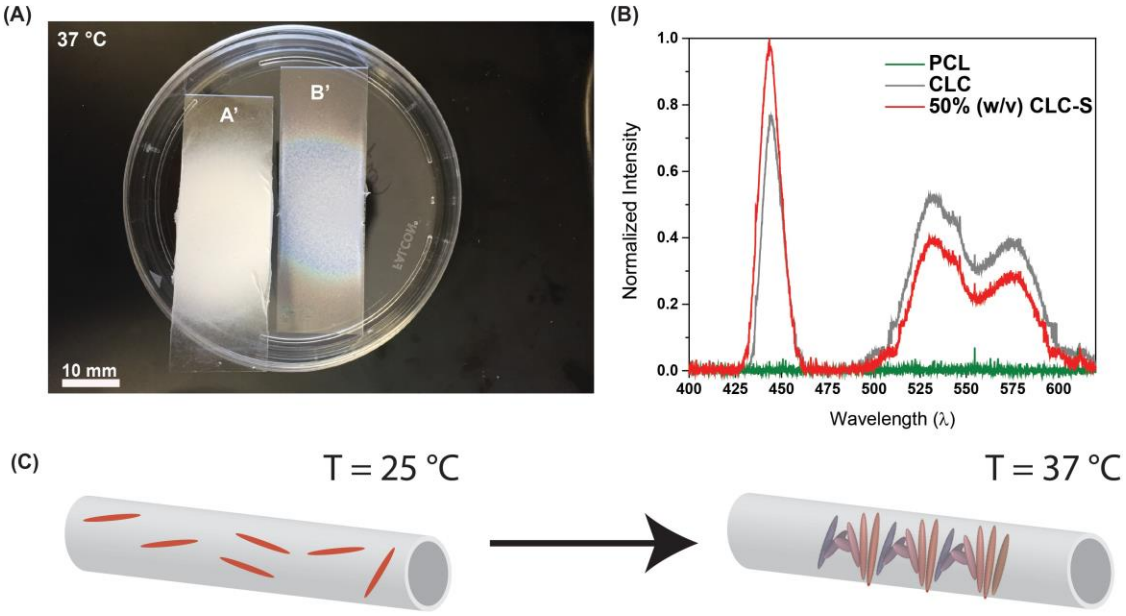

Figure S2.2. Photograph of the engineered cholesteryl ester liquid crystal scaffolds (CLC-S). (A) Representative polycaprolactone (PCL) sample A' and 50% (w/v) CLC-S sample B' were heated to 37 °C before the image was taken. It is evident from the photograph that the CLC-S sample was thermochromic while the control PCL sample was opaque. (B) Ultraviolet–visible spectroscopy of generated PCL, cholesteryl ester liquid crystal, and CLC-S at 37 °C. (C) Schematic of how upon heating the CLC-S to 37 °C, the fingerprint-like striations can reflect light as seen in photograph (A).

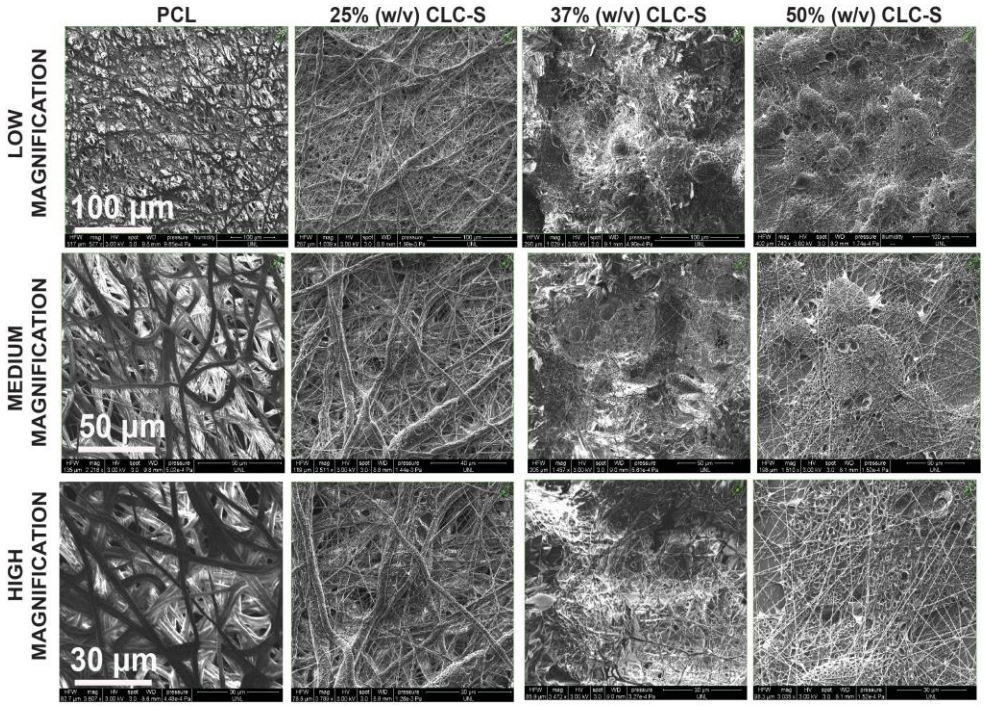

Figure S2.3. Scanning electron micrograph of the cholesteryl ester liquid crystal scaffolds (CLC-S). Varying magnification of the generated weight per volumes of 0%, 25%, 37%, and 50% CLC-S. PCL: polycaprolactone.

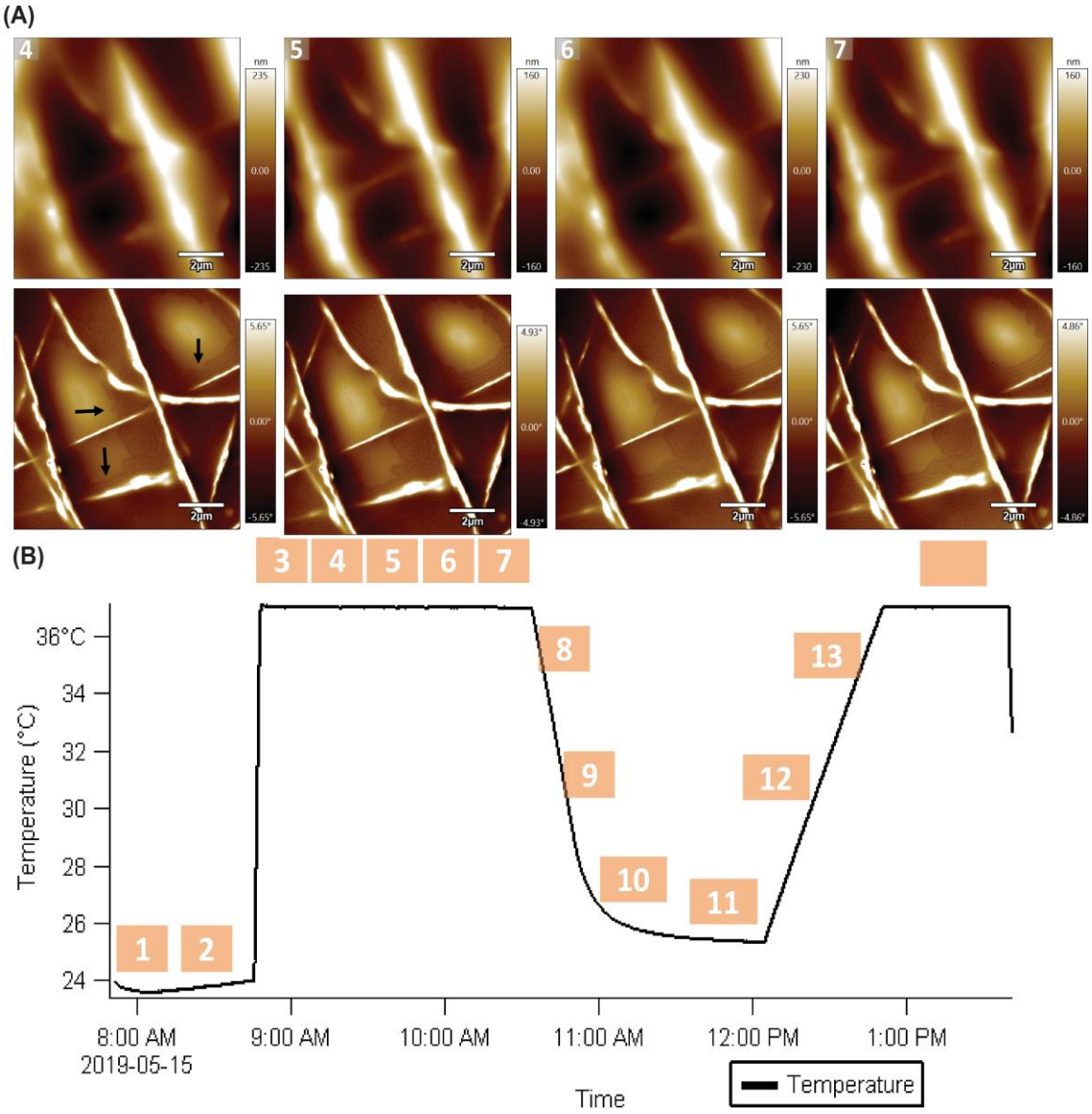

Figure S2.4. (A) Atomic force microscopy (AFM) temperature ramp experiments with 50% (w/v) cholesteric liquid crystal substrates (CLC-S). Upper panels are topographic images; lower panels are simultaneously acquired phase contrast images of the same area. (B) Samples were heated to 37 °C and were monitored over 1 hour. This measurement indicates that the CLC domains were dynamic and moving within the webbing of the nanofibers.

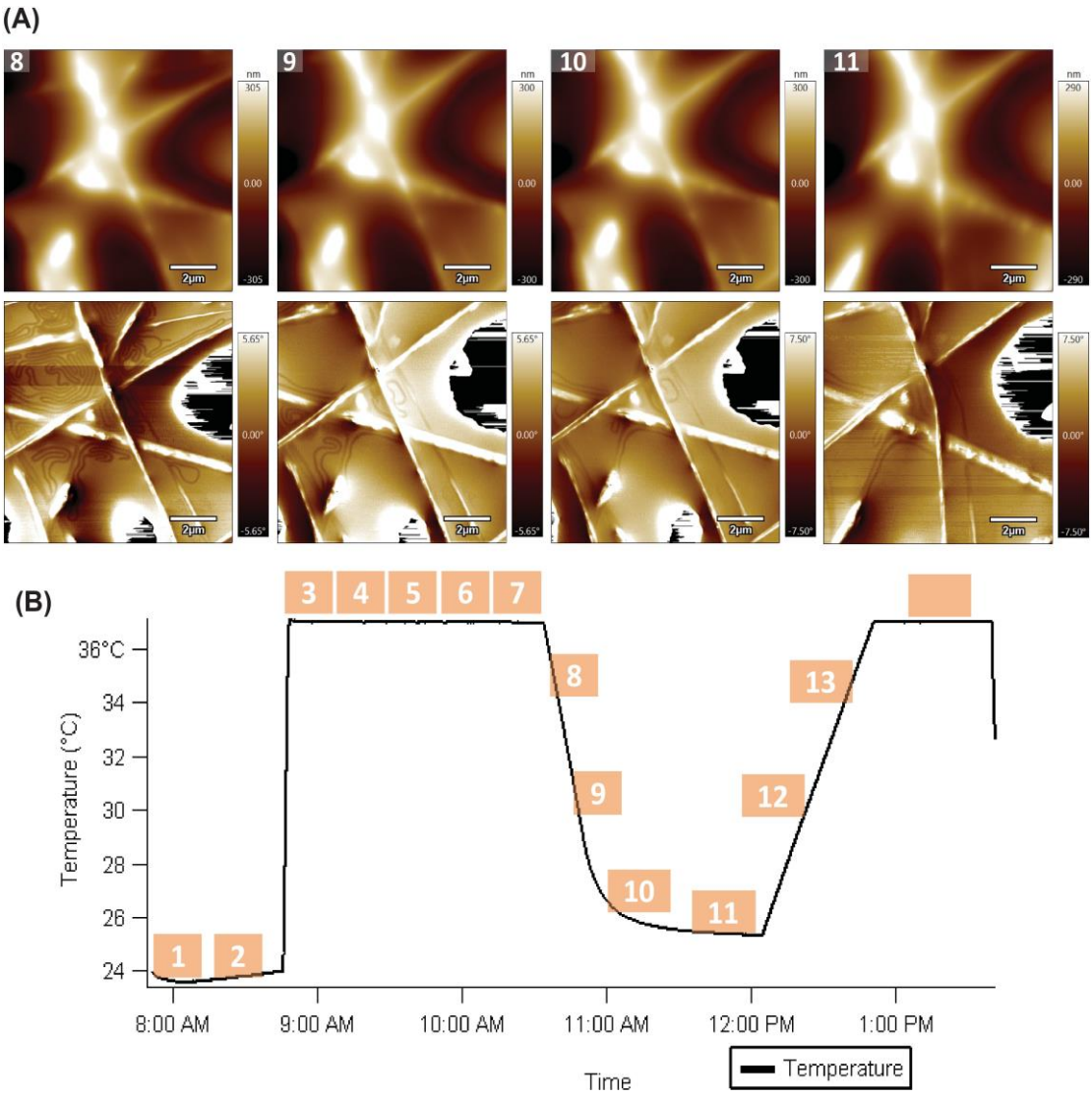

Figure S2.5. (A) Atomic force microscopy assessment of temperature ramp experiments with 50% (w/v) cholesteric liquid crystal scaffolds (CLC-S). Upper panels are topographic images; lower panels are simultaneously acquired phase contrast images of the same area. (B) Samples were heated to 37 °C then cooled to room temperature. The appearance of CLC domains within the webbing of the scaffolds was found to be reversible.

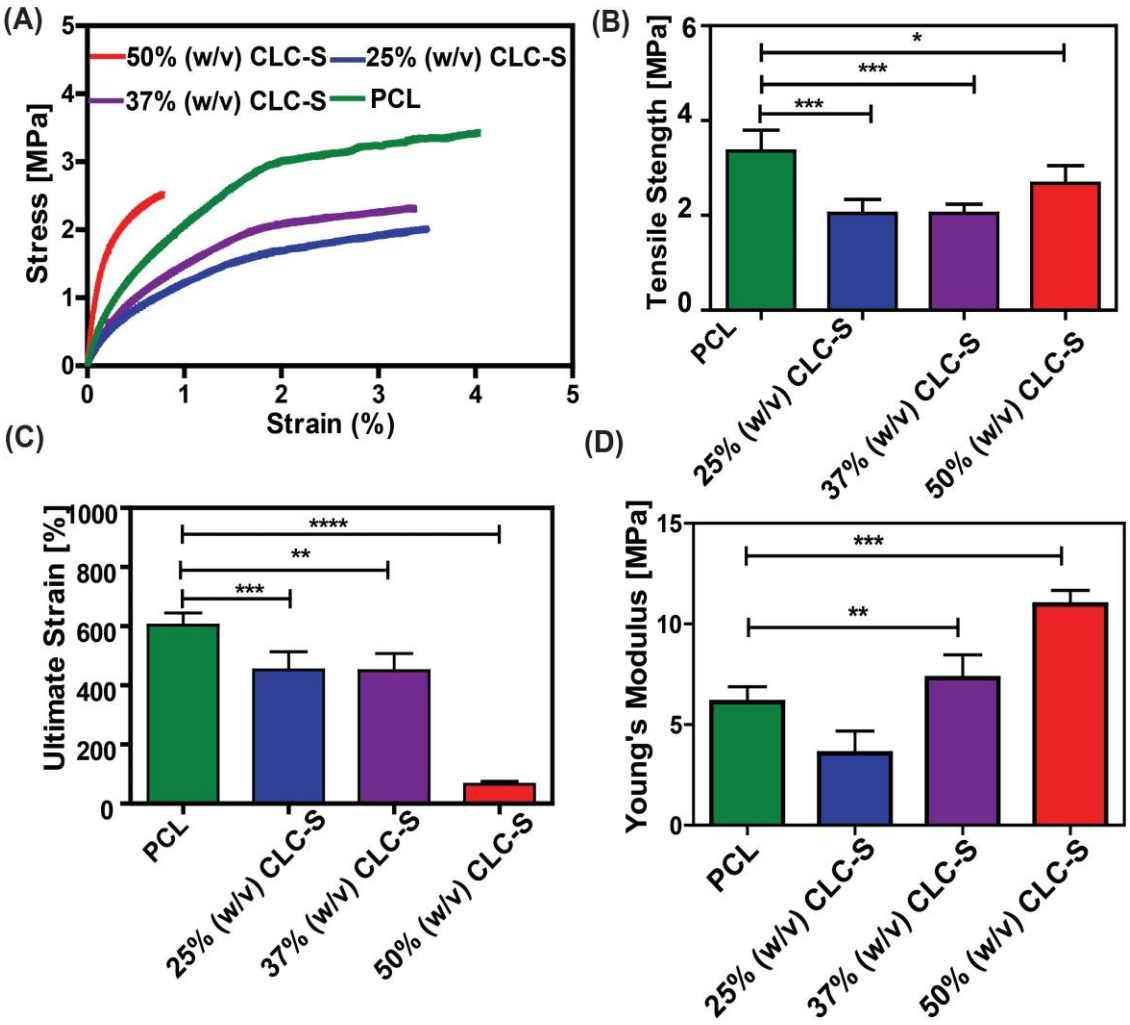

Figure S2.6. Bulk mechanical testing of cholesteryl ester liquid crystal scaffolds (CLC-S). (A) Representative stress-strain curve for generated hybrid CLC-S (B) Tensile strength; (C) Ultimate strain; and (D) Young's modulus (n = 4, statistical analysis by one-way ANOVA). PCL: polycaprolactone.

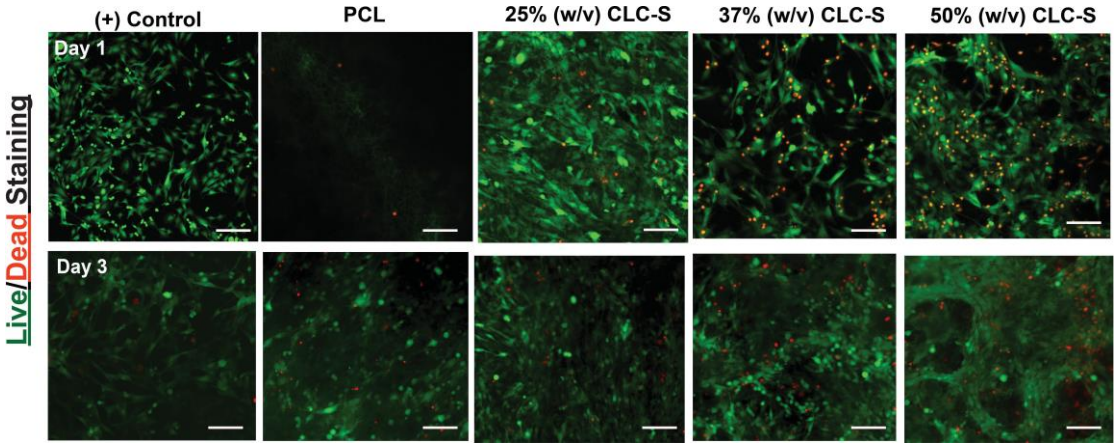

Figure S2.7. Live/dead staining of the cholesteryl ester liquid crystal scaffold (CLC-S). Samples were incubated with calcein acetoxymethyl ester and ethidium homodimer in phosphate-buffered saline and imaged under fluorescence microscope. All scale bars are 200 μm. Control: Cell Culture Well plate PCL: polycaprolactone.

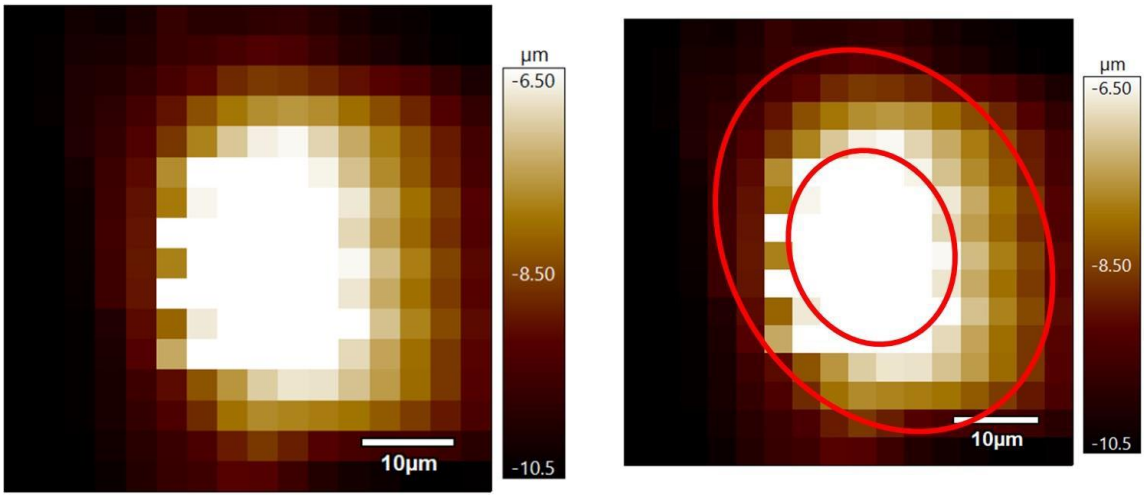

Figure S2.8. Phase contrast images of mouse myoblast (C2C12) cells cultured on the substrates tested under controlled cell culture conditions, resulting in the atomic force microscopy cellular adhesion Young's modulus testing results the images depict the morphology of a single cell with cellular proper dimensions further validating the fidelity of the experiments.

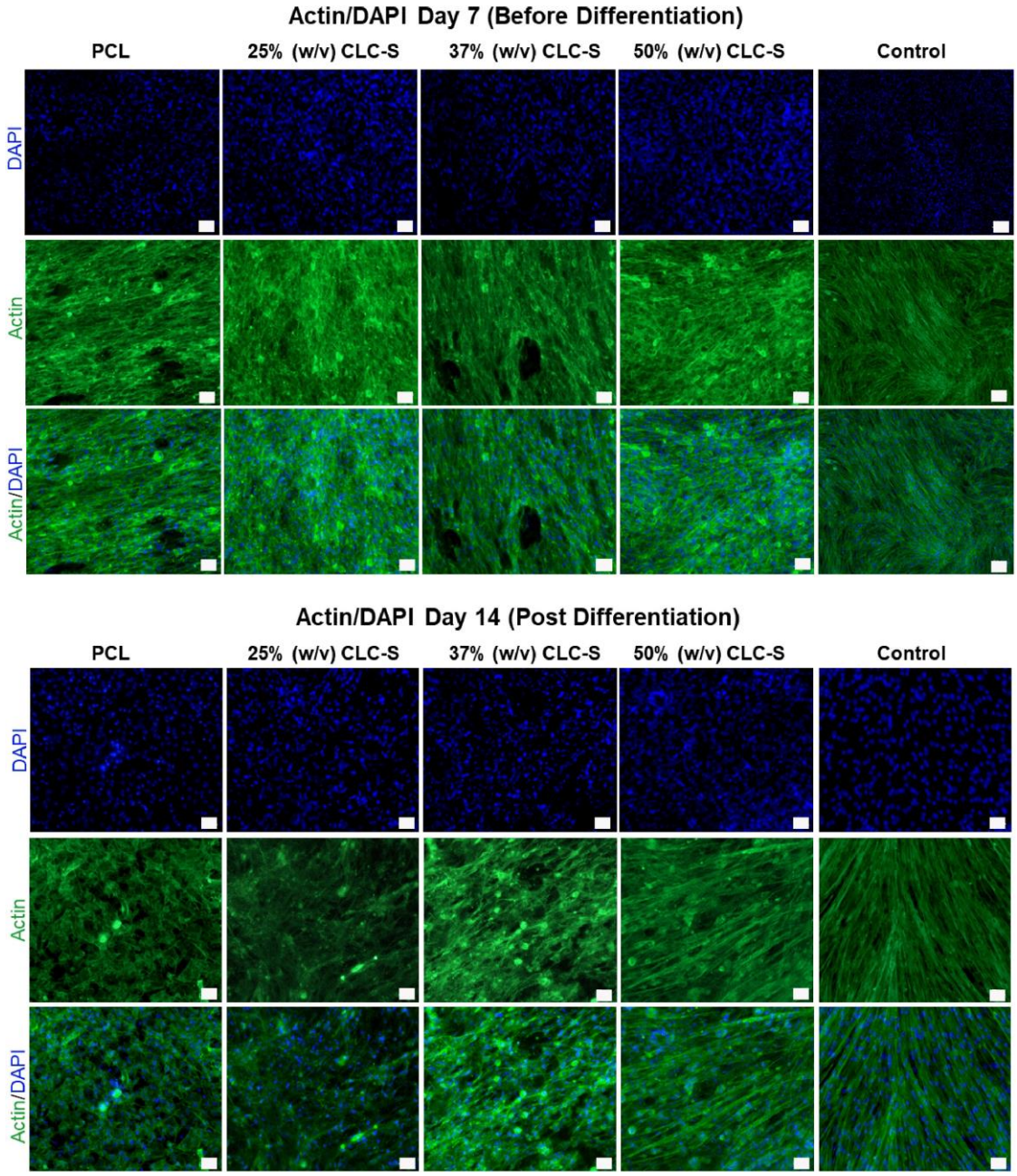

Figure S2.9. F-actin/DAPI staining of cells cultured on the cholesteryl ester liquid crystal scaffolds (CLC-S) on Day 7 (before differentiation) and Day 14 (after differentiation). All scale bars are 50 µm. DAPI: 4',6-diamidino-2-phenylindole, PCL: polycaprolactone, CLC-S: cholesteryl ester liquid crystal scaffold.

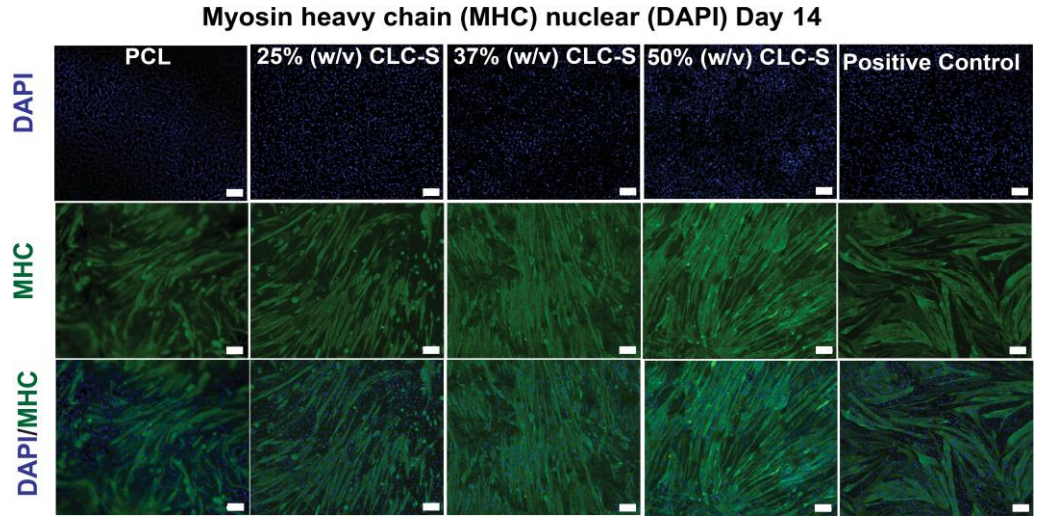

Figure S2.10. Immunohistochemistry staining of myosin heavy chain (MHC) and 4′,6-diamidino- 2-phenylindole (DAPI) of C2C12 mouse myoblasts cultured on various tested cholesteryl ester liquid crystal scaffolds (CLC-S), Day 14, after differentiation. All scale bars are 100 µm. PCL: polycaprolactone.

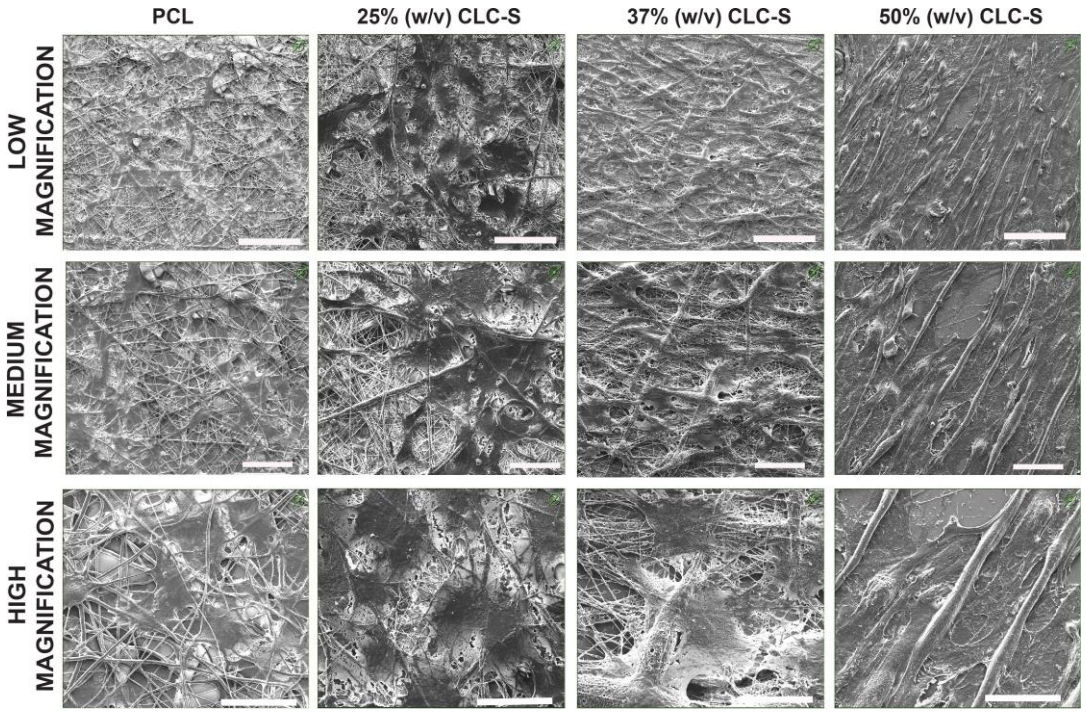

Figure S2.11. Scanning electron micrographs of the cholesteryl ester liquid crystal scaffolds (CLC-S) day 14 differentiation of mouse myoblast cells (C2C12). Scale bars: top panels 100 µm, middle panels 50 µm, bottom panels 30 µm. PCL: polycaprolactone.

Chapter 3

Nanoengineered Antiviral Fibrous Arrays with Rose-Thorn-Inspired Architectures

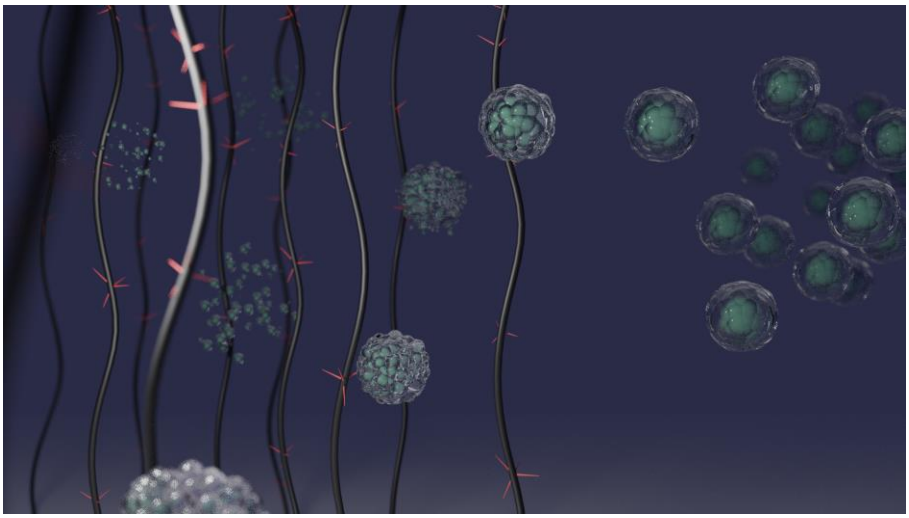

The information in this chapter was published in *ACS Materials Letters*, **2021**, *3*, 1566-1571 and has been reproduced with permission from the authors.

"A Nanoengineered Antiviral Fibrous Array with Rose-Inspired Architecture", Nasajpour, A., Samandari, M., Chandrashekhar, P., Abolhassani, R., Suryawanshi, R., Adelung, R., Rubahn, H., Mishra, Y, Khademhosseini, A., Shukla, D., Tamayol, A., and Weiss, P., S., *ACS Materials Letters*, **2021**, *3*, 1566-1571

3.1 Abstract

Herpes simplex virus (HSV) plagues billions of humans with infections globally. We have developed and demonstrated rose-thorn-inspired antiviral fibrous arrays by electrospinning a composite of polycaprolactone (PCL) polymer with a dispersion of anisotropic zinc oxide tetrapod nanoparticles (ZOTeN). This rose-thorn-mimicking material enables physical and chemical protection. Under blue light stimulation, ZOTeN photocatalyze the production of hydrogen peroxide for an accessible disinfection and sterilizing mechanism to prolong material usage. Using scanning electron microscopy and X-ray photoelectron spectroscopy, we confirm the rose-thorn-inspired morphology and the chemical composition, respectively. The fibrous material has dose-dependent antiviral properties against both HSV-1 and HSV-2. The engineered mats can potentially be used for manufacturing antiviral garments, face coverings, and bandages.

3.2 Introduction

Herpes simplex virus (HSV) is a double-stranded DNA virus with an icosahedral protein cage enveloped by a lipid bilayer.[1] This virus is responsible for billions of human infections globally. Symptoms range from asymptomatic to life-threatening complications, depending on the host's health and age. There are two major strains of HSV – HSV-1, which is associated with oral and ocular infections, and HSV-2, which is associated with genital diseases.[2,3] Current standards of care for HSV treatments rely on the oral delivery or intravenous injection of nucleoside analogs such as acyclovir, famciclovir, or valacyclovir. Topical treatments use 5% valacyclovir as well as 10% docosanol ointments.[3] HSV treatments include immune response modifiers, vaccines, and nanomaterials.[4] Interestingly, zinc oxide tetrapod nanoparticles (ZOTeN) have been shown to bind HSV viral particles electrostatically *via* oxygen vacancies and overall greater biocompatibility compared to varying zinc oxide nanoparticle morphology.[5-7] The bound viral particles "train" the

host immune cells *in vivo*, providing a synergistic microbicidal effect and vaccine treatment against primary and secondary female genital herpes infections.[8,9]

3.3 Methods and Discussion

In this study, we build on previous work demonstrating that ZOTeN rose-thorn-inspired materials enhance antimicrobial behavior compared to scaffolds containing commercially available spherical ZnO nanoparticles, due to the rose-thorn-like spikes morphology developed with the anisotropic ZOTeN provide the catalytic surfaces needed for antimicrobial and antiviral properties.[10] We hypothesized that these ZOTeN rose-thorn-like protrusions will generate antiviral properties when incorporated into nonwoven fibrous mats that could provide topical treatment for herpes simplex virus and could be deployed as antiviral garments, or face coverings in viral outbreaks. These thorns create interfaces in which the ZOTeN catalytic surfaces protrude from the scaffold. The scaffolds in this study were engineered by electrospinning ZOTeN with an ester-terminated polycaprolactone polymer solution (Scheme 3.1). Not demonstrated in our initial rose-thorn nanofiber study, visible light (405 nm) source can excite the ZOTeN rose-thorn protrusions above the nanomaterial's bandgap to photocatalyze a sterilizing-effect.[10-12] This sterilizing mechanism enhances the ZOTeN-laden fibers' intrinsic antimicrobial and antiviral properties.

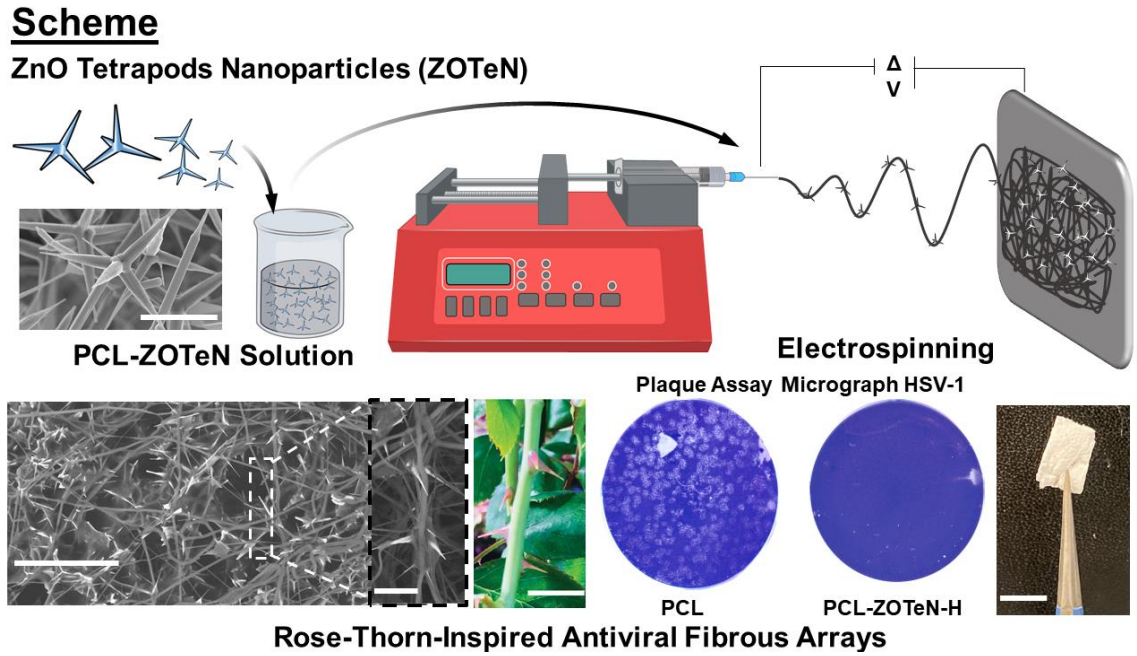

Scheme Scheme 3.1. Method to generate the rose-thorn-inspired antiviral dressing topical treatment for herpes simplex virus (HSV-1) and (HSV-2). The fabrication scheme for the electrospun zinc oxide tetrapod nanoparticles (ZOTeN) ZnO-laden nanofibers is developed with a 2% ZOTeN weight per volume (w/v), 4% (w/v) ZOTeN solution, a 12% (w/v) polycaprolactone (PCL)-ester-terminated hexafluoroisopropanol solution spun using a conventional electrospinning setup. Scale bars are 3 µm for the ZOTeN particles, 100 µm for the electrospun structure, 20 µm for rose-thorn-shaped material scanning electron micrograph, and 2 mm for the actual rose digital photograph.

We imaged the electrospun scaffolds using scanning electron microscopy (SEM) to test their morphologies and to determine the interface architectures of the bioinspired engineered mats. The polycaprolactone (PCL) polymer control without the ZOTeN had typical nanofiber morphologies. However, upon the addition of the ZOTeN, a rose-thorn-like morphology, derived from the ZOTeN arms, protrudes from the surface of the nanofiber. This morphology provides an interface favorable for viral particle interactions (Figures 3.1a and S3.2). At higher concentrations of ZOTeN, denser networks of the rose-thorn-mimicking morphology were produced. To measure the fibers' surface properties, X-ray photoelectron spectroscopy (XPS) is deployed to identify the oxidation states of three elements – zinc, oxygen, and carbon. The zinc region (Zn 2p) was of particular interest, as it probes the interface for antiviral as well photoactive properties. The Zn 2p

peaks were symmetric, indicating only one valence state in ZOTeN. The peak positions of Zn $2p_{3/2}$ in both samples were at 1026 eV, corresponding to the Zn^{2+} valence state.[13] Both conditions had a Zn $2p_{½}$ peak at 1049 eV (Figure 3.1b). The Zn 2p intensities signals were greater in the electrospun material with higher concentrations of ZOTeN compared to the scaffolds with lower particle content. We anticipate that the higher levels of the Zn^{2+} valence state in PCL-ZOTeN-HIGH will have greater overall antiviral and photoactive activity upon blue light stimulation. The oxygen region (O 1s) was asymmetric, suggesting more than one oxygen state on the surface of ZOTeN. From the PCL-ZOTEN-HIGH spectra obtained, the lower binding energy, 529 eV, was assigned to the lattice O^{2-} ions (O_L) bonding to Zn^{2+} ions forming ZOTeN wurtzite crystal structure (Figure 3.1b).[13,14] The higher binding energy oxygen peak, found at 530 eV, correlated to the oxygen of the hydroxyl-terminated (O_H) found on the surface of the ZOTeN.[13,14]

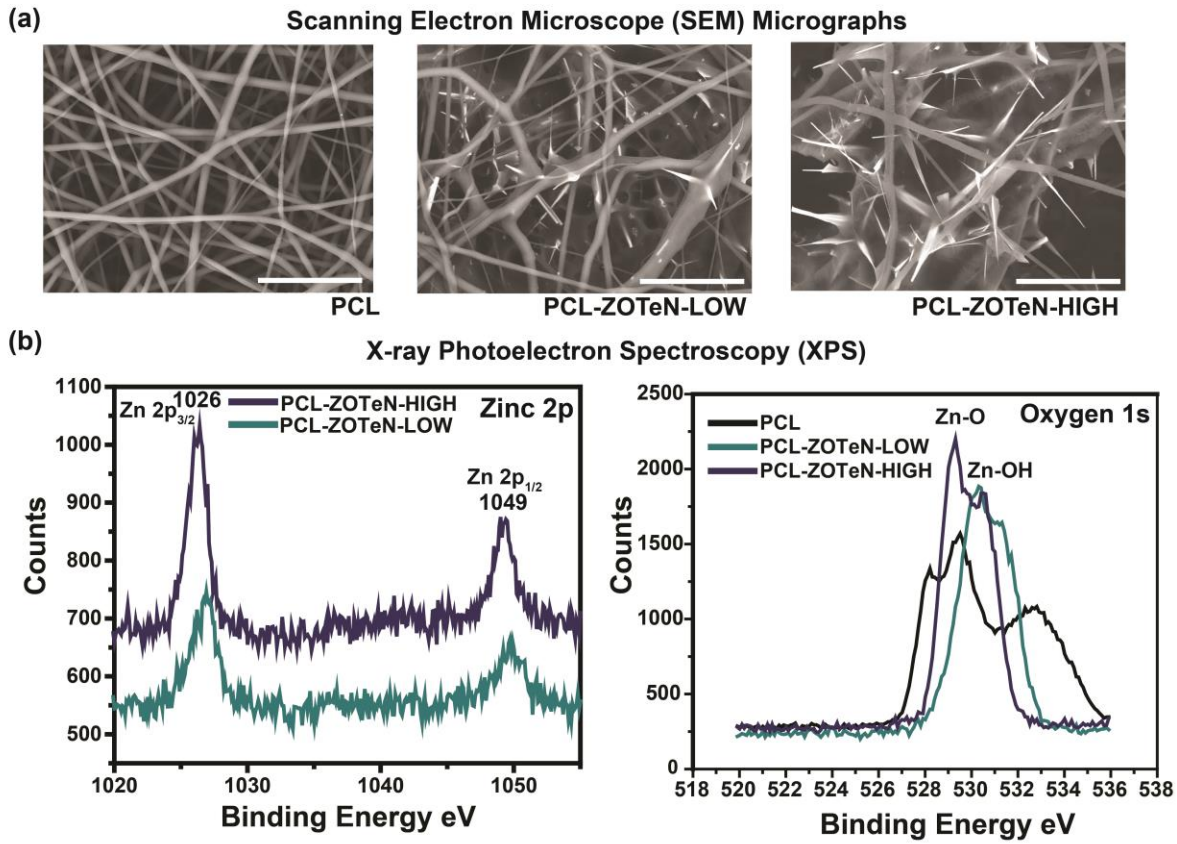

Figure 3.1. Scanning electron microscope (SEM) micrographs and X-ray photoelectron spectroscopy (XPS) of the rose-thorn-inspired antiviral zinc oxide tetrapod nanoparticles (ZOTeN) dressing material. (**a**) Scanning electron microscopy images of the polycaprolactone (PCL) -only scaffold, PCL-ZOTeN-LOW, and PCL-ZOTeN-HIGH. The ZOTeN nanomaterial generates a rose-thorn-inspired dressing material with varying nanomaterial prickle density, mimicking thorn-like protrusions. (**b**) X-ray photoelectron spectra regions the zinc 2p regions, and oxygen 1s regions in the electrospun ZOTeN nanofibers.

A narrow scan of the carbon region (C1s spectrum) of the PCL polymer indicated a binding energy at 281 eV for the methylene carbons and a binding energy of 285 eV for the carbonyl carbons. These values correlate with published work.[14] The carbonyl carbon binding energy was shifted to 286 eV for 4% (w/v) ZOTeN (PCL-ZOTeN-HIGH) and 287 eV binding energy for 2% (w/v) ZOTeN (PCL-ZOTeN-LOW). The XPS results for the PCL carbonyl indicate charged interactions between the ZOTeN nanomaterial and PCL polymer relative to the unmodified pristine polymer.

To enhance the materials' lifetime and durability, we engineered a sterilizing mechanism *via* blue light (405 nm) excitation; under illumination, this process excites electrons to the conduction band, producing electron-hole pairs on the ZOTeN surface. This excitation leads to photoelectrochemical reactions that sterilize the viruses off the scaffolds' surfaces. By submerging the scaffolds in an aerated aqueous media and illuminating with blue light, the nanomaterial surface converts molecular oxygen and water to hydrogen peroxide (H_2O_2), superoxide anion (O_2^-), and hydroxyl radicals (OH). The latter two short-lived species are reactive and can also produce hydrogen peroxide.[13,17,18] Here, we placed the composite dressing material in an aqueous environment and excited them with blue light to produce H_2O_2 from water photochemically (see Supplementary Information for detailed conditions).

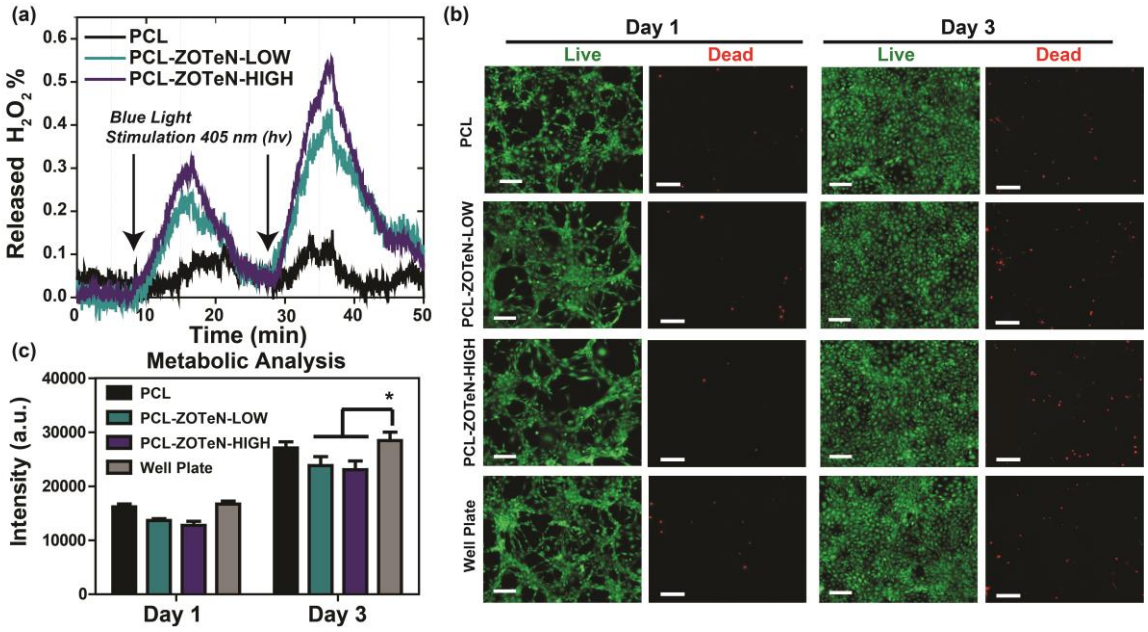

Figure 3.2. Rose-thorn-inspired zinc oxide tetrapod nanoparticles (ZOTeN) dressing light-harvesting properties and the dressing materials' overall biocompatible safety. (**a**) Catalytic production of hydrogen peroxide under blue light stimulation as a function of time. (**b**) Live-dead cytotoxicity assay of a co-culture of NIH (3T3) murine fibroblast and dressing materials tested in the study monitor the cellular membrane integrity at days 1 and 3. (**c**) Metabolic analysis of the biomaterials tested within this study on days 1 and 3 (n=4, *: P <0.05). Scale bars are 200 µm.

To test the photocatalyzed H_2O_2 generation, we incubated the samples with 0.1% (w/v) bovine liver catalase, an enzyme that reacts with H_2O_2 and decomposes it into O_2 and water. We monitored this enzyme-mediated decomposition reaction using a commercial O_2 optical sensor. Upon illumination, the control PCL nanofiber scaffolds do not generate any H_2O_2 and the enzyme produced no measurable O_2 in our *in-situ* measurements (Figure 3.2a). The PCL-ZOTeN-LOW scaffolds did generate O_2 (via H_2O_2), as measured with the optical probe. The PCL-ZOTeN-HIGH had similar behavior upon illumination, but produced higher levels of H_2O_2, which we attribute to the higher density of ZOTeN nanomaterial in the nanofiber network (Figures 3.2a and S3.2). In addition, the XPS results demonstrate that there is a higher concentration of ZOTeN at the interface from the signal intensity (Figure 3.1b). ZOTeN created a favorable interface to oxidize water to

create ROS species. To validate the ability to generate hydrogen peroxide further, a colorimetric assay was performed comparing a solution of H_2O_2 as a positive control, a phosphate buffer solution as a negative control, PCL, and the PCL-ZOTeN scaffold. Samples were measured before and after blue light exposure (Figure S3.4b). The colorimetric assay demonstrated detectable H_2O_2 generation by ambient non blue stimulated PCL-ZOTeN scaffolds in an aqueous media, upon blue light exposure an increase in the level of detectable H_2O_2 generation is noted. These results further demonstrate the capability of the rose-thorn-inspired scaffolds to produce H_2O_2 in a self-sterilization mechanism.

We tested the dressing material's biocompatibility using NIH 3T3 fibroblasts. The viability of the cells was assessed with a Live/Dead Cell Viability Assay Kit (Figure 3.1b). All the tested conditions had comparable results between days 1 and 3 of culture. To investigate these dressing materials' biocompatibility further, we monitored the fibroblast cells' metabolic activity using the PrestoBlue assay. On day 1, we did not see any statistically significant differences between the tested dressing materials PCL, PCL-ZOTeN-LOW, and PCL-ZOTeN-HIGH groups compared to cells cultured on the well plate in the absence of the dressing materials. However, PrestoBlue assay results indicated decreases in cellular viability, compared to the control group with increasing ZOTeN concentration (P-value=0.041 for PCL-ZOTeN-LOW *vs* P-value=0.014 for PCL-ZOTeN-HIGH). This result suggests potential toxicity due to increased levels of free radical species and/or H_2O_2 in PCL-ZOTeN-HIGH.

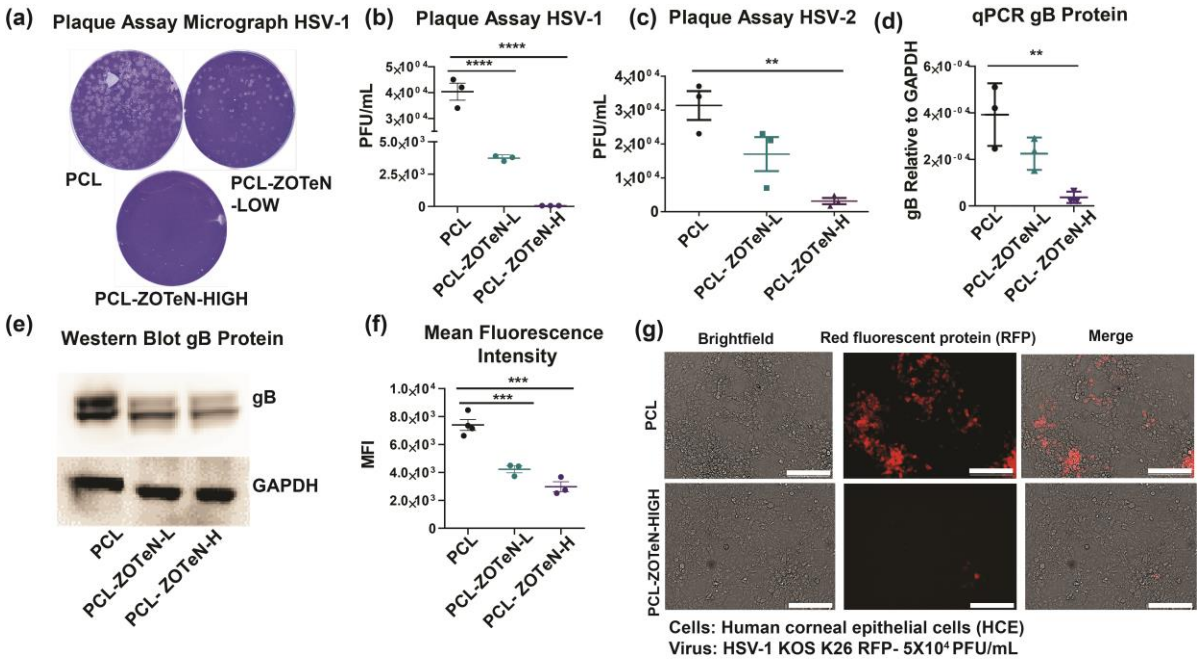

Figure 3.3. Antiviral properties of the tested zinc oxide tetrapod nanoparticles (ZOTeN) dressing material against simplex herpes virus (HSV-1) and (HSV-2) (**a**) HSV-1 plaque assay micrograph of the tested dressing composites demonstrating concentration-dependent inhibition of plaque formation. (**b**) Quantitative measurement of plaque formation between tested dressing conditions a statistical difference was found between tested groups. (**c**) Quantitative HSV-2 plaque assay results. (**d**) Quantitative polymerase chain reaction (qPCR) measures the gB spike protein essential for host infection and dissemination. (**e**) Immunoblot measurements to measure gB proteins in cultured human corneal epithelial cells (HCE) with the generated dressing materials. (**f**) Mean fluorescence intensity measurements of HCE cells co-culture experiments with HSV-1 virions expressing red fluorescent protein (RFP) demonstrates ZOTeN concentration dependence inhibition of virus replication. (**g**) Micrograph images from red fluorescent protein expression from HSV-1 infection with HCE. (n=3 for plaque assay results HSV-1 and HSV-2, mean fluorescence intensity, ***: P <0.001). Scale bar: 200 µm.

To test the fibers' herpes virus neutralization capacity, experiments were first performed against HSV-1 and HSV-2 without visible light stimulation. We performed a plaque assay against both HSV subtypes to measure the dressing's efficacy in trapping and neutralizing the viral particles. Briefly, a plaque assay is a quantitative method to measure infectious virus (here, HSV-1 and HSV-2) particles. This method is the standard for quantifying the concentration of replication-competent lytic virions (Figures 3.3a,b and S3.4). In our study, statistically significant differences were found in the plaque assay for HSV-1 between PCL, PCL-ZOTeN-LOW, and PCL-ZOTeN-HIGH. The micrograph images provided depict plaque formation in PCL, while the addition of the ZOTeN reduces associated plaque formation in a concentration-dependent manner (Figure 3.3a,b). Chemical surface analyses and SEM micrographs confirmed that this concentration dependence was related to the amount of exposed ZOTeN surface available to bind the virus (Figure 3.1b). In the HSV-2 plaque assay experiment, we tested the efficacy of neutralization as before, and found a statistically significant antiviral properties in the PCL-ZOTeN-HIGH composite to the HSV-2 strain (Figures 3.3c and S3.4). Our findings from the plaque assay report a statistically significant effect on the antiviral properties with dressing materials dispersed with ZOTeN, especially the PCL-ZOTeN-HIGH dressing. To understand the dressing's antiviral capabilities, we now further monitored the amount of envelope glycoprotein B (gB) mRNA transcripts synthesized by HSV-1 when cultured with human corneal epithelial cells (HCE) using quantitative polymerase chain reaction (qPCR). The HSV-1 gB transcripts were significantly higher in the PCL condition. Western blot data further confirmed the trend of gB expression at the translational level (Figure 3.3d,e). We used the housekeeping protein glyceraldehyde 3-phosphate dehydrogenase (GAPDH) needed for glycolysis, to ensure the validity of the experimental data. These results indicate that the addition of the ZOTeN had a concentration-

dependent inhibitory effect on virus replication. We infer that ZOTeN thorn architecture within the polymer nanofiber enhances virus trapping and neutralization (Figure 3.3a-f).

Western blot experiments further demonstrated the antiviral properties improved by adding the ZOTeN nanomaterial to the nanofiber dressing materials (Figure 3.3e). Reduced gB protein expression was concentration dependent, as above. For a positive control, we used the housekeeping protein glyceraldehyde 3-phosphate dehydrogenase (GAPDH) needed for glycolysis, to validate the experimental data. Lastly, we monitored the mean fluorescence intensity of a modified HSV-1 viral particle (KOS K26 RFP) that expressed a red fluorescent protein, which corresponds to virus replication. We found the ZOTeN scaffolds show less RFP expression in a concentration-dependent manner. This result further confirmed the dressing's ability to reduce viral particle dissemination (Figure 3.3f,g). The positive control PCL condition had a large percentage of cells expressing the RFP molecular marker. While treatment of the rose-thorn-inspired dressing material reduced virus infection and replication in a concentration-dependent manner with ZOTeN-containing nanomaterials.

3.4 Conclusions and Prospects

In summary, we developed a rose-thorn-inspired antiviral dressing material with visible light activated sterilizing properties. We synthesized this antiviral fibrous topical treatment that displays potent efficacy against HSV-1 and HSV-2 virus *in vitro* with cultured human corneal epithelial cells. We will further develop and test this promising antiviral dressing biomaterial for the topical treatment of HSV-1 and HSV-2 and possibly for other similarly enveloped viral particles, including with *in vivo* animal models and if warranted, in clinical studies.

References

1. Whitley, R. J.; Roizman B. Herpes Simplex Virus Infections. *Lancet*. **2001**, *357*,1513-1518.

2. Farooq, A.V.; Shukla D. Herpes Simplex Epithelial and Stromal Keratitis: An Epidemiologic Update. *Surv. Ophthalmol*. **2012**, *57*, 448–462.

3. Brady, R. C.; Bernstein, D. I. Treatment of Herpes Simplex Virus Infections. *Antiviral Res*. **2004**, *61*, 73−81.

4. Ianevski, A.; Zusinaite, E.; Kuivanen, S.; Strand, M.; Lysvand, H.; Teppor, M.; Kakkola, L.; Paavilainen, H.; Laajala, M.; Kallio-Kokko, H.; et al. Novel Activities of Safe-in-Human Broad-Spectrum Antiviral Agents. *Antiviral Res.* **2018**, *154*, 174−182.

5. Mishra, YK; Adelung, R.; Rohl, C.; Shukla, D.; Spors, F.; Tiwari, V. Virostatic Potential of Micro-Nano Filopodia-Like ZnO Structures against Herpes Simplex Virus-1. *Antiviral Res*. **2011**, *92*, 305−312.

6. Antoine, T. E.; Mishra, Y. K.; Trigilio, J.; Tiwari, V.; Adelung, R.; Shukla, D. Prophylactic, Therapeutic and Neutralizing Effects of Zinc Oxide Tetrapod Structures against Herpes Simplex Virus Type-2 Infection. *Antiviral Res.* **2012**, *96*, 363−375.

7. Papavlassopoulos, H.; Mishra, Y. K.; Kaps, S.; Paulowicz, I.; Abdelaziz, R.; Elbahri, M.; Maser, E.; Adelung, R.; Röhl, C. Toxicity of Functional Nano-Micro Zinc Oxide Tetrapods: Impact of Cell Culture Conditions, Cellular Age, and Material Properties. *PLoS One* **2014**, 9, e84983

8. Agelidis, A.; Koujah, L.; Suryawanshi, R.; Yadavalli, T.; Mishra, Y. K.; Adelung, R.; Shukla, D. An Intra-Vaginal Zinc Oxide Tetrapod Nanoparticles (ZOTEN) and Genital Herpesvirus Cocktail Can Provide a Novel Platform for Live Virus Vaccine. *Front. Immunol.* **2019**, *10*, 500.

9. Antoine, T. E.; Hadigal, S. R.; Yakoub, A. M.; Mishra, Y. K.; Bhattacharya, P.; Haddad, C.; Valyi-Nagy, T.; Adelung, R.; Prabhakar, B. S.; Shukla, D. Intravaginal Zinc Oxide Tetrapod Nanoparticles as Novel Immunoprotective Agents against Genital Herpes. *J. Immunol.* **2016**, *196*, 4566−4575.

10. Nasajpour, A.; Mandla, S.; Shree, S.; Mostafavi, E.; Sharifi, R.; Khalilpour, A.; Saghazadeh, S.; Hassan, S.; Mitchell, M. J.; Leijten, J.; Hou, X.; Moshaverinia, A.; Annabi, N.; Adelung, R.; Mishra, Y. K.; Shin, S. R.; Tamayol, A.; Khademhosseini, A. Nanostructured Fibrous Membranes with Rose Spike-Like Architecture. *Nano Lett.* **2017**, *17*, 6235–6240.

11. Rubin, T. R.; Calvert, J. G.; Rankin, G. T.; MacNevin, W. Photochemical Synthesis of Hydrogen Peroxide at Zinc Oxide Surfaces. *J. Am. Chem. Soc*. **1953**, *75*, 2850−2853.

12. Domenech, X.; Ayllo'n, J. A.; Peral, J. H_2O_2 Formation from Photocatalytic Processes at the ZnO/Water Interface. *Environ. Sci. Pollut. Res*. **2001**, *8*, 285−287.

13. Xu, X.; Chen, D.; Yi, Z.; Jiang, M.; Wang, L.; Zhou, Z.; Fan, X.; Wang, Y.; Hui, D. Antibacterial Mechanism Based on H_2O_2 Generation at Oxygen Vacancies in ZnO Crystals. *Langmuir* **2013**, *29*, 5573–5580.

14. Chang, Y. G.; Xu, J.; Zhang, Y. Y.; Ma, S. Y.; Xin, L. H.; Zhu, L. N.; Xut, C. T. Optical Properties and Photocatalytic Performances of Pd Modified ZnO Samples. *J. Phys. Chem. C* **2009**, *113*, 18761−18767.

15. Louette, P.; Bodino, F.; Pireaux, J. J. Poly(caprolactone) (PCL) XPS Reference Core Level and Energy Loss Spectra. *Surf. Sci. Spectra* **2005**, *12*, 27−31.

16. Al-Gaashani, R.; Radiman, S.; Daud, a. R.; Tabet, N.; Al-Douri, Y. XPS and Optical Studies of Different Morphologies of ZnO Nanostructures Prepared by Microwave Methods. *Ceram. Int.* **2013**, *39*, 2283−2292.

17. Kelly, S. R.; Shi, X.; Back, S.; Vallez, L.; Park, S. Y.; Siahrostami, S.; Zheng, X.; Nørskov, J. K. ZnO As an Active and Selective Catalyst for Electrochemical Water Oxidation to Hydrogen Peroxide. *ACS Catal.* **2019**, *9*, 4593–4599.

18. Siahrostami, S.; Li, G.-L.; Viswanathan, V.; Norskov, J. K. One or Two-Electron Water Oxidation, Hydroxyl Radical, or H_2O_2 Evolution. *J. Phys. Chem. Lett.* **2017**, *8*, 1157−1160.

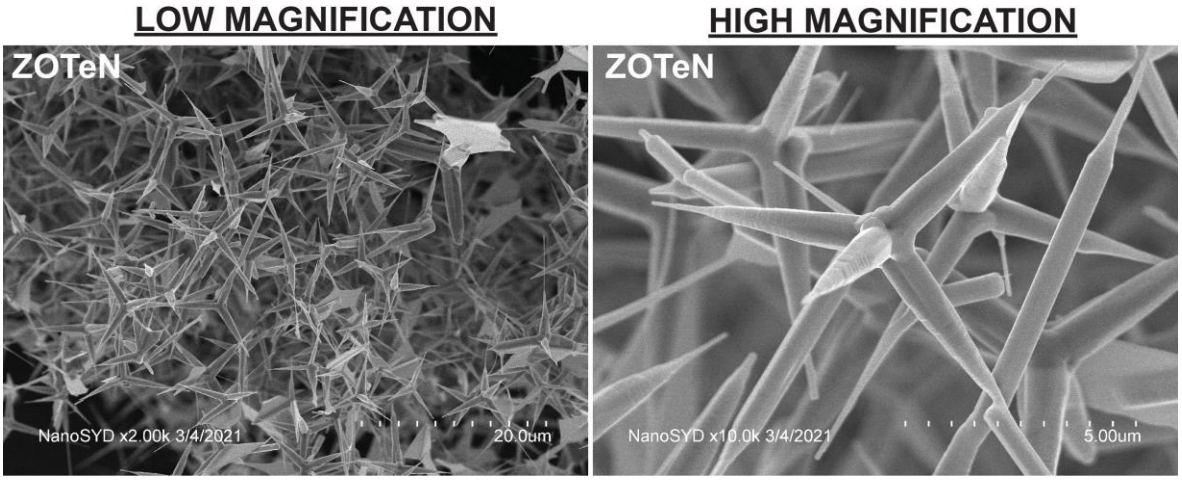

Figure S3.1. Nanomaterial scanning electron micrographs of the micro- and nanoscale zinc oxide tetrapod nanostructures (ZOTeN) used for the synthesis of the rose-thorn-inspired antiviral dressing.

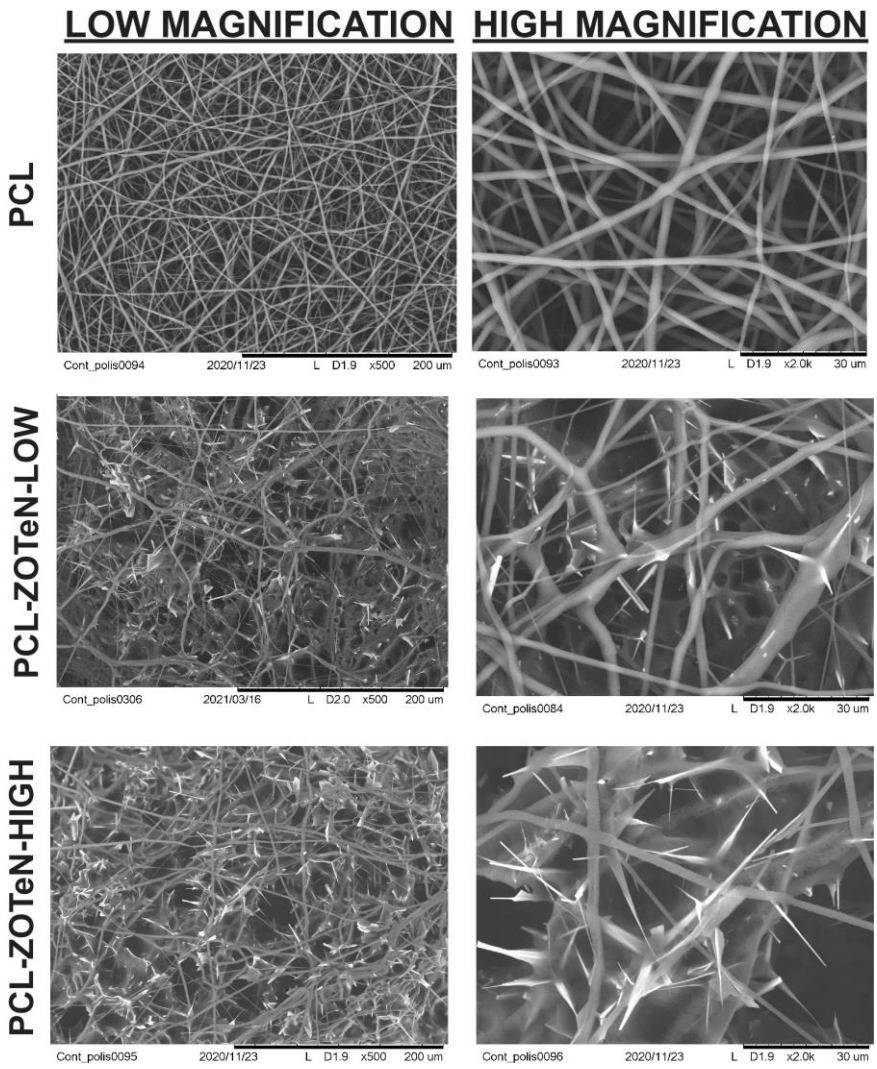

Figure S3.2. Scanning electron micrographs of the engineered rose-thorn-inspired antiviral dressing. Representative polycaprolactone (PCL) with varying concentration of micro- and nanoscale zinc oxide tetrapod nanostructures (ZOTeN).

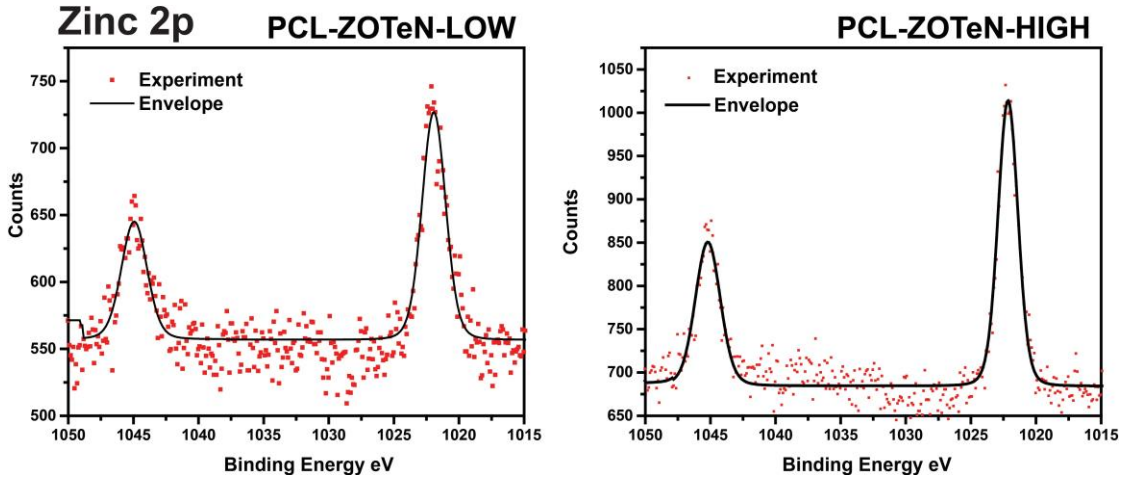

Figure S3.3. X-ray photoelectron spectroscopy (XPS) spectra of the zinc element for the rose-thorn- inspired nanofibers. Varying spectra of the generated weight per volume (w/v)% of micro- and nanoscale zinc oxide tetrapod nanostructures (ZOTeN), 2% (w/v) ZOTeN-LOW, and 4% (w/v) ZOTeN-HIGH to PCL: polycaprolactone.

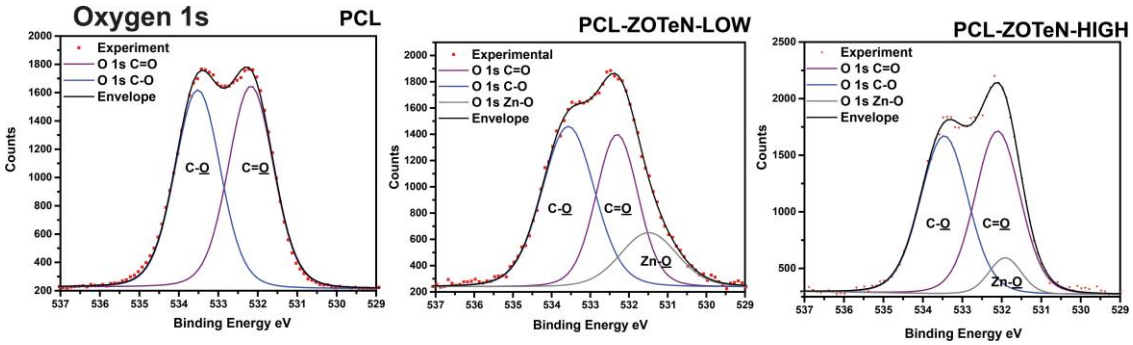

Figure S3.4. X-ray photoelectron spectroscopy (XPS) spectra of the oxygen element for the rose-thorn-inspired nanofibers. Varying spectra of the generated weight per volume (w/v)% of micro- and nanoscale zinc oxide tetrapod nanostructures (ZOTeN), 2% (w/v) ZOTeN-LOW, and 4% (w/v) ZOTeN-HIGH to PCL: polycaprolactone.

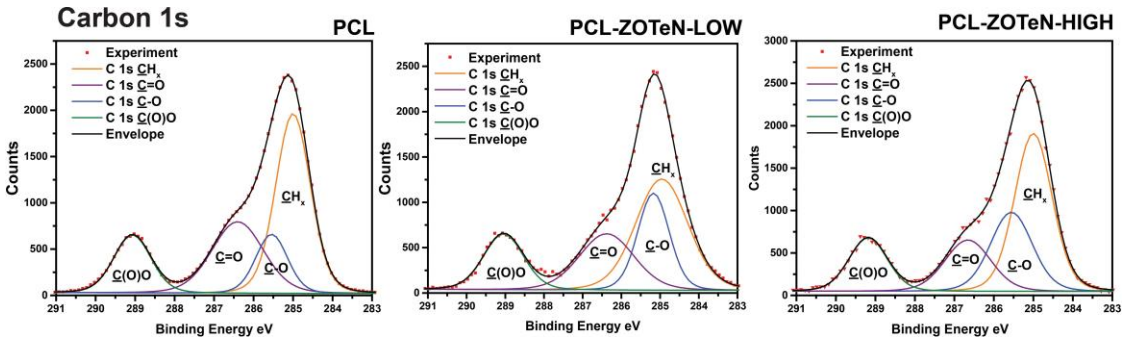

Figure S3.5. X-ray photoelectron spectroscopy (XPS) spectra of the carbon element for the rose-thorn-inspired nanofibers. Varying spectra of the generated weight per volume (w/v)% of micro- and nanoscale zinc oxide tetrapod nanostructures (ZOTeN), 2% (w/v) ZOTeN-LOW, and 4% (w/v) ZOTeN-HIGH to PCL: polycaprolactone.

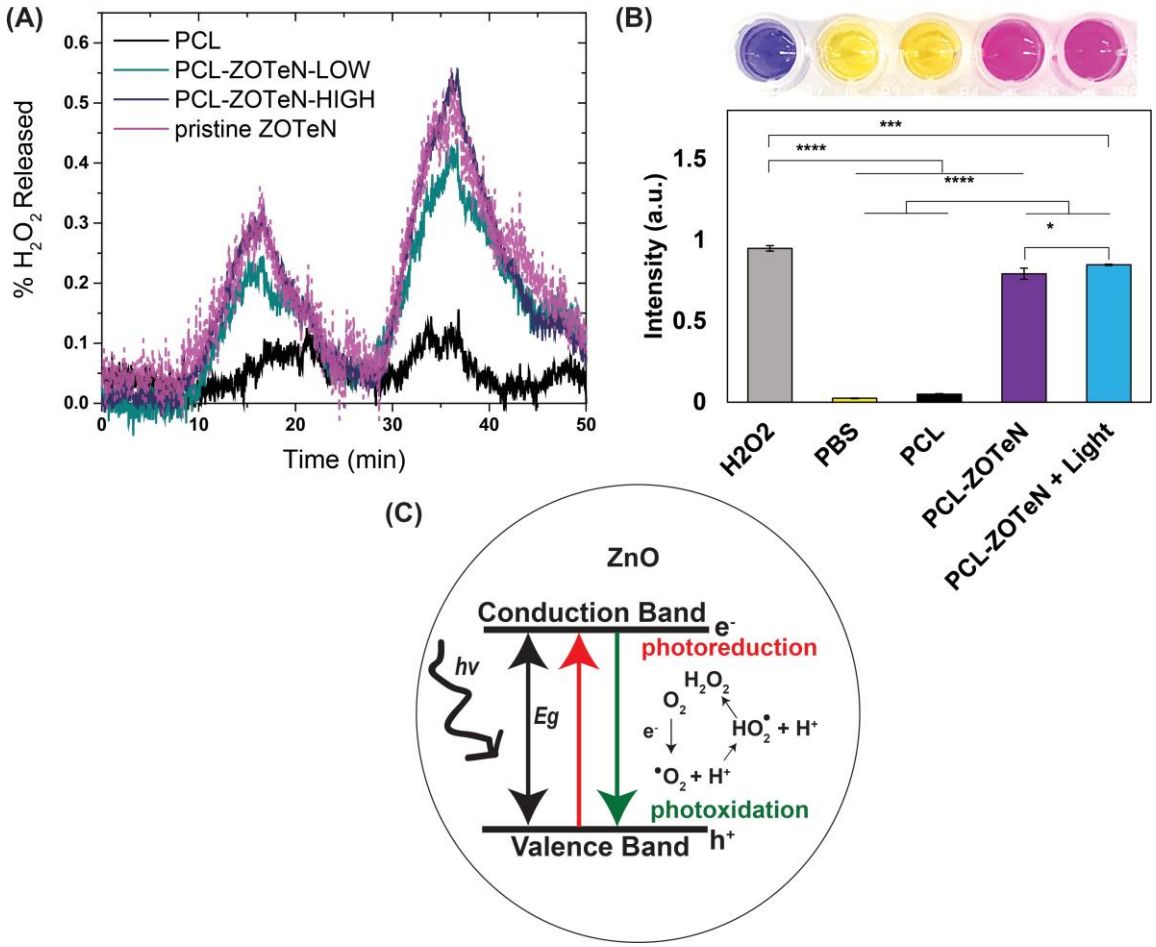

Figure S3.6. (a) Hydrogen peroxide generation detected by catalyze enzyme and optical probe of the generated weight per volume (w/v) %, 2% (w/v), and 4% (w/v) micro- and nanoscale zinc oxide tetrapod nanostructures (ZOTeN) with 12% (w/v) polycaprolactone. (b) H_2O_2 colorimetric assay. (c) ZnO catalytic mechanism proposed.

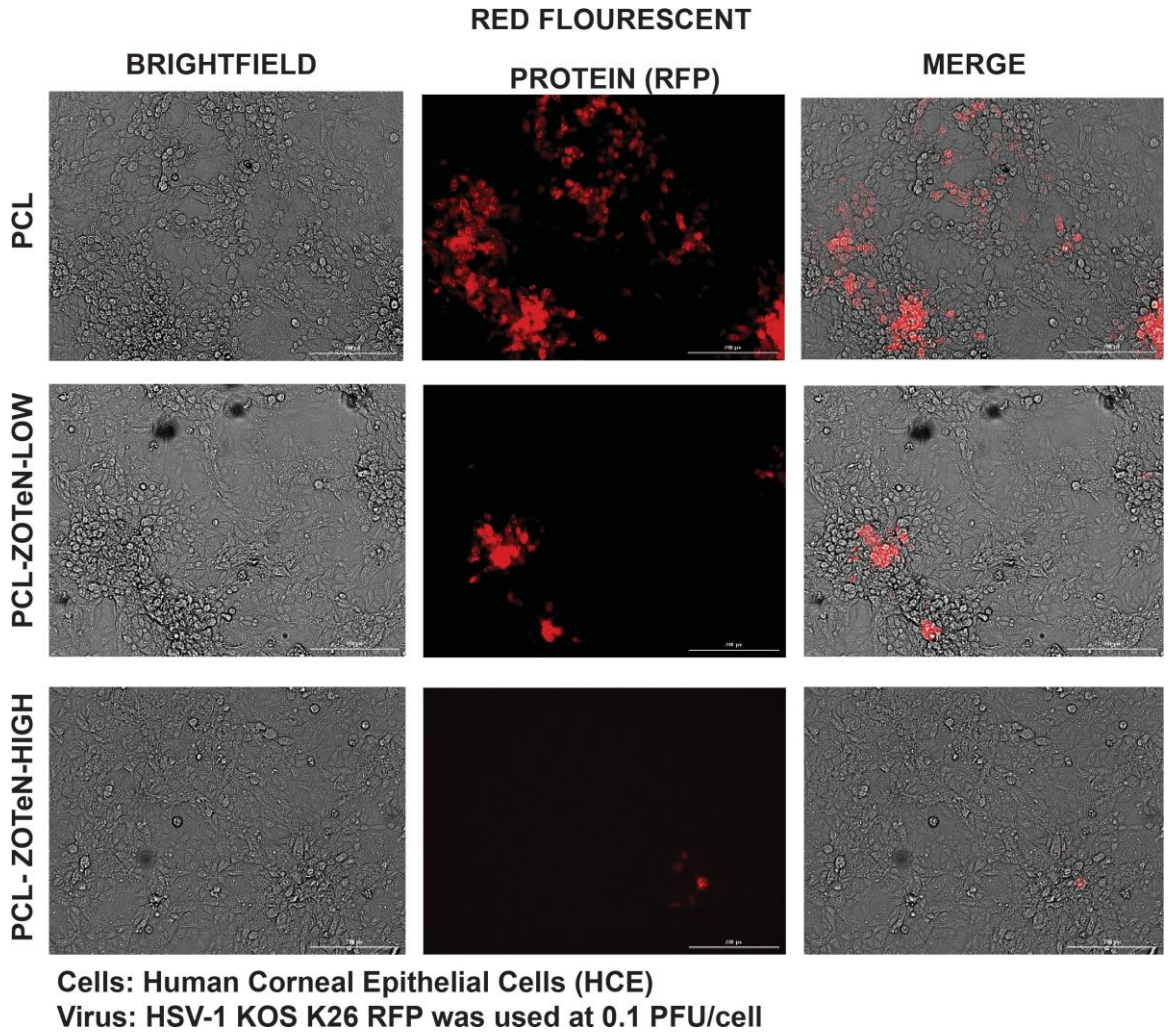

Figure S3.7. Fluorescence red protein measurements of HSV-1 KOS K26 cultured with human corneal epithelial cell lines (HCE) varying magnification of the generated weight per volume of 0%, 2%, and 4% ZOTeN. PCL: polycaprolactone, ZOTeN: zinc oxide tetrapod nanomaterials.

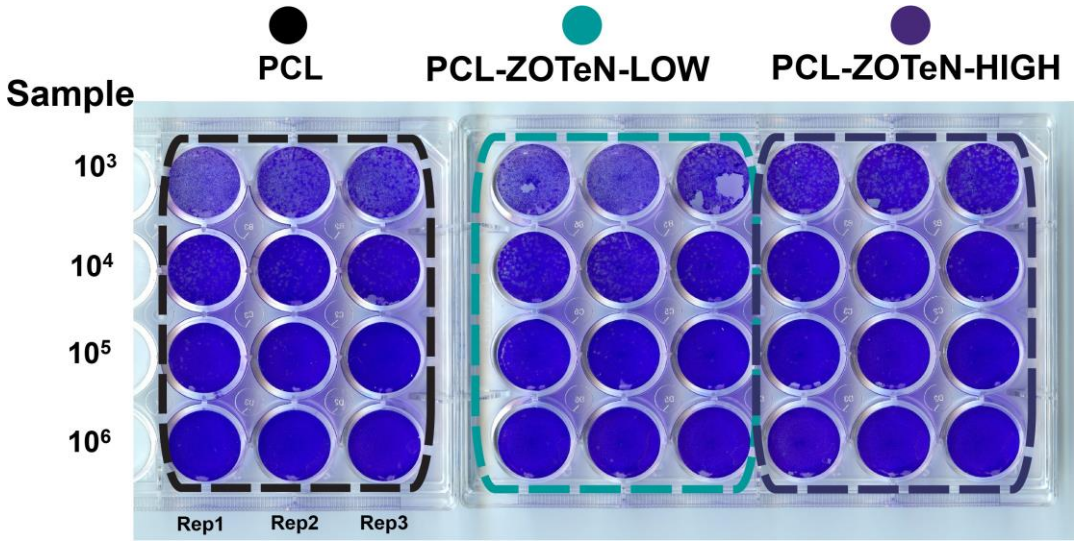

Figure S3.8. Plaque assay micrograph of HSV-2 well plate for tested weight per volumes of 0%, 2%, and 4% (w/v)% micro- and nanoscale zinc oxide tetrapod nanostructures (ZOTeN) with 12%(w/v) PCL: polycaprolactone.

Chapter 4

A Whitlockite-Enabled Hydrogel for Craniofacial Bone Regeneration

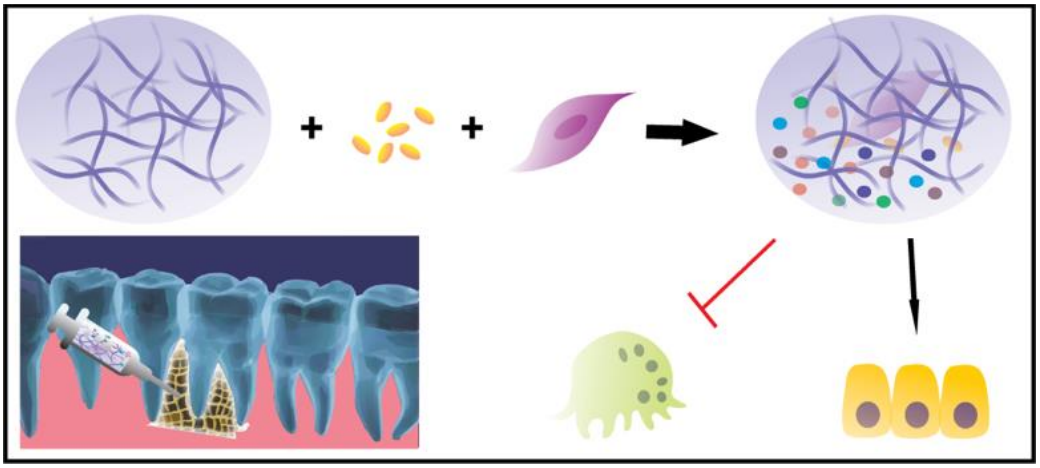

The information in this chapter was published in *ACS Applied Materials & Interfaces* **2021**, *13, 35342–35355* and has been reproduced with permission from the authors.

"Whitlockite-Enabled Hydrogel for Craniofacial Bone Regeneration." Pouraghaei Sevari, S.; Kim, J. K.; Chen, C.; Nasajpour, A.; Wang, C.-Y.; Krebsbach, P. H.; Khademhosseini, A.; Ansari, S.; Weiss, P. S.; Moshaverinia, A. *ACS Applied Materials & Interfaces* **2021**, *13* (30), 35342– 35355

4.1 Abstract

Growth factor-free bone regeneration remains a challenge in craniofacial engineering. Here, we engineered an osteogenic niche comprised of a commercially modified alginate hydrogel and whitlockite microparticles (WHMPs), which impart tunable physicochemical properties that can direct osteogenesis of human gingival mesenchymal stem cells (GMSCs). Our *in vitro* studies demonstrate that WHMPs induce osteogenesis of GMSCs more effectively than previously demonstrated hydroxyapatite microparticles (HApMPs). Alginate-WHMP hydrogels showed higher elasticity without any adverse effects on the viability of the encapsulated GMSCs. Moreover, the alginate-WHMP hydrogels upregulate the mitogen-activated protein kinase (MAPK) pathway, which in turn orchestrates several osteogenic markers, such as Runx2 and OCN, in the encapsulated GMSCs. Concurrent co-culture studies with human osteoclasts demonstrate that GMSCs encapsulated in alginate-WHMP hydrogels downregulate osteoclastic activity, potentially due to release of Mg^{2+} ions from the WHMPs along with secretion of osteoprotegerin from the GMSCs. *In vivo* studies demonstrated that the GMSCs encapsulated in our osteogenic niche were able to promote bone repair in calvarial defects in murine models. Altogether, our results confirmed the development of a promising treatment modality for craniofacial bone regeneration based on an injectable growth factor-free hydrogel delivery system.

4.2 Introduction

Regenerative medicine shows great promise for tissue engineering to treat bone defects, but new functional materials are required for this strategy.[1] The most commonly used technique for repairing bone defects, autologous grafts, has a number of significant disadvantages, such as high cost, complications associated with surgery, pain, bone morbidity, the limited amount of

endogenous bone available, and the concern of persistent inflammation. Although the development of novel biomaterials has revolutionized tissue engineering to avoid some of these drawbacks, a significant gap remains between the demand for advanced clinical therapies and the degree of achieved clinical translation.[25] Injectable, cell-laden osteogenic hydrogels with the ability to downregulate osteoclasts may therefore be of particular interest in regenerating maxillofacial bone.

Mesenchymal stem cells (MSCs) are a source of self-renewing cells residing in various adult tissue with the potential to give rise to numerous types of specialized cells for restoring damaged tissue and organs.[2] Orofacial tissue, harbors mesenchymal stem cells that can be easily harvested for regenerating damaged tissue and have higher bone regenerative potential than bone marrow mesenchymal stem cells (BMMSCs).[3-5] Gingival mesenchymal stem cells (GMSCs) are abundant and easily accessed from the gingiva or from remnant tissue found in the clinic. Furthermore, recent studies have revealed that GMSCs have an innate ability to downregulate osteoclastogenesis by secreting key anti-osteoclastogenic soluble factors, such as osteoprotegerin (OPG).[6-8]

Ex vivo expanded MSCs have been combined with scaffolds for use in a wide spectrum of bone regeneration applications.[9-11] An ideal biomaterial for bone regeneration should promote osteogenesis, be biocompatible with no risk of disease transmission, and biodegrade over an appropriate timescale to enable ingrowth of newly formed tissue. Previously, we have shown that alginate is a suitable candidate for the encapsulation of dental-derived MSCs.[12,13] Osteoconductive hydrogels have been produced by embedding different growth factors (*e.g.*, BMP-2) and bioactive particles (*e.g.*, hydroxyapatite), or simply by harnessing the ability of the hydrogel to induce osteogenic differentiation.[14-17] Whitlockite (WH: $Ca_{18}Mg_2(HPO_4)_2(PO_4)_{12}$) is a magnesium calcium phosphate ceramic that is an important inorganic phase found in bone, comprising up to

20% of bone mineral weight.[18] Studies have confirmed that WH particles are more effective than hydroxyapatite (HAp: $Ca_{10}(PO_4)_6(OH)_2$) in encouraging cellular proliferation and osteogenic differentiation and are able to hinder the activity of osteoclasts.[19,20] In addition, WH is more stable in acidic environments than HAp.[21]

These bioactive WH particles can be incorporated directly within 3D stem cell cultures, enabling control over their amount and spatial presentation. The presence of WH within the stem cell culture differentially modulates expression patterns of numerous differentiation markers at the gene and protein levels without having severe cellular toxicity. Therefore, WH microparticles (MPs) could be embedded within a three-dimensional (3D) hydrogel along with MSCs to control the spatial presentation of the extracellular matrix while directing the differentiation and fate of the MSCs.

To orchestrate osteogenic differentiation the activation of the mitogen-activated protein kinase (MAPK) pathway is critical and controlled by physicochemical properties, like the elasticity of the hydrogel matrix.[22-24] Other research groups have demonstrated that osteogenic differentiation is regulated by key members of the MAPK signaling pathway, particularly Jun amino-terminal kinases (JNK), P38, and extracellular signal-related kinases (ERK).[24] Therefore, studying the precise role of WHMPs in triggering MAPKs and their upstream cascades involved in the osteodifferentiation of encapsulated GMSCs is of great importance.

To respond to the growing demand for alternative therapeutic solutions for bone regeneration, we fabricated a hydrogel based on arginine-glycine-aspartic acid (RGD)-coupled alginate and WH microparticles (WHMPs) that is able to induce osteogenesis of human gingival mesenchymal stem cells (GMSCs). The osteogenic differentiation of the encapsulated GMSCs within the WHMP-loaded hydrogel was studied both *in vitro* and *in vivo*. We analyzed the

molecular mechanism of the osteogenesis of encapsulated GMSCs and assessed the osteoclast downregulatory capacity of the engineered hydrogel.

4.3 Methods and Discussion

We incorporated WHMPs and HApMPs into RGD-coupled alginate (Alg-RGD) and assessed their effect on the osteodifferentiation of encapsulated GMSCs. Scanning electron microscopy (SEM) images confirm the semi-spherical and spherical morphologies for the micrometer-sized aggregates of WHMPs and HApMPs, respectively, with an average size of 5 μm (Figure 4.1a). The energy dispersive X-ray spectroscopy (EDS) data confirm the presence of calcium, magnesium, and phosphate in the WHMPs and the presence of calcium and phosphate in the HApMP, as shown in the inserts in Figure 1a.

X-ray diffraction (XRD) and Raman spectroscopy were used to compare the physical properties of WHMPs and HApMPs. The XRD patterns of the WHMPs and HApMPs corresponded well with previously reported results (Figure 4.1b).[21,26] The Raman spectrum of the WHMPs shows the ν_2 PO_4^{3-} bending vibration at 407 cm^{-1} and the ν_1 PO_4^{3-} symmetric stretching mode at ~970 cm^{-1}, which are characteristic marker bands in WH.[27,28] The Raman spectrum of the HApMPs shows a band at ~960 cm^{-1}, which is characteristic of HAp (Figure 4.1c).[27,29]

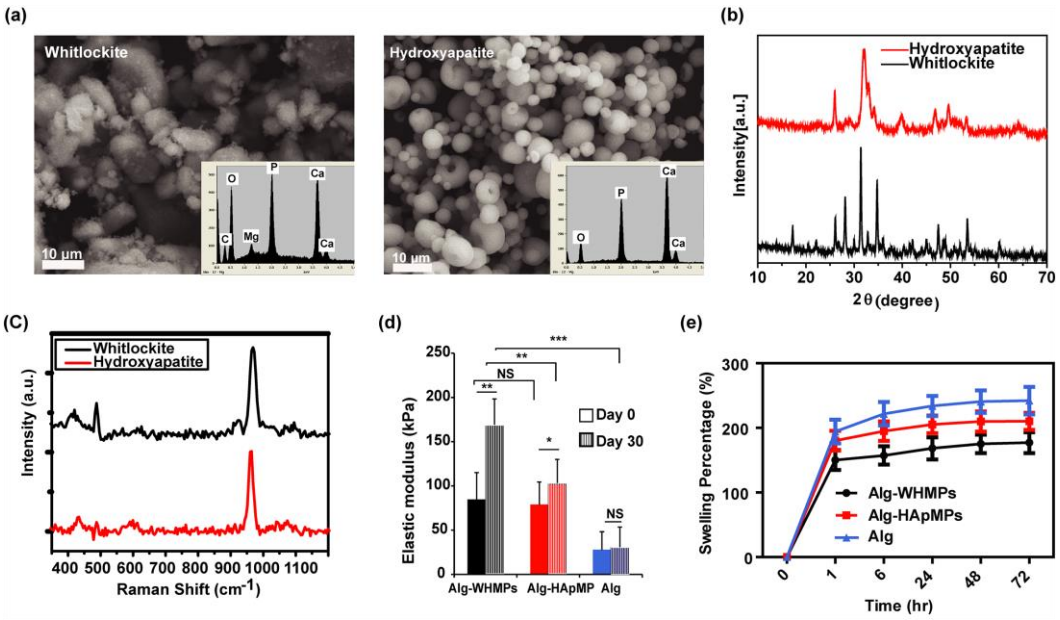

Figure 4.1. Hydrogel Characterizations (a) Scanning electron microscopy (SEM) images of whitlockite microparticles (WHMPs) and hydroxyapatite microparticles (HApMPs). Inserts are the energy dispersive X-ray spectroscopy (EDS) results corresponding to each microparticle type. Scale bars are 10 µm. Bulk compositional analyses of WHMPs and HApMPs acquired using (b) X-ray diffraction (XRD) and (c) Raman spectroscopy. (d) The elastic moduli of the fabricated hydrogels containing 1 mg/mL WHMPs or HApMPs, measured on the day of fabrication (D0) and 1 month (D30) after fabrication. Alginate hydrogel without further modification was used as the control group. (e) The swelling ratio of the fabricated hydrogels was measured by incubating the dry hydrogels in phosphate-buffered saline (PBS) buffer at 37 ºC at several time points.

Mechanical analyses of the prepared hydrogels showed that the elastic modulus of the WHMP-loaded hydrogel was not significantly higher than the HApMP-loaded hydrogel on day 0 ($p > 0.5$). However, the WHMP-loaded hydrogel showed significantly higher elastic modulus than the HApMP-loaded hydrogel on day 30 (Figure 4.1d). Hydrogels are known for their ability to swell in aqueous environments, with swelling ratios that depend on their composition. After a few hours, the hydrogels reach equilibrium, after which there is no further swelling. We observed lower swelling ratios in the hydrogels containing WHMPs compared to those containing HApMPs, which is consistent with their higher elastic moduli (Figure 4.1e).

It is important to determine the protein permeability of the fabricated hydrogels, because any cells encapsulated in the hydrogels can be affected by soluble cues in the surrounding medium or body fluid, including cytokines and growth factors released by the cells themselves. The secretome of MSCs, in particular, is known to affect the local microenvironment and provide immunosuppression.[32] Alginate hydrogels are often used as delivery vehicles to release therapeutic proteins.[30,31] Bovine serum albumin (BSA) was encapsulated within our hydrogls as a model protein to evaluate the hydrogel microstructure and its permeability to release soluble biological factors secreted from the encapsulated GMSCs. After incorporating BSA into both the WHMP-loaded and HApMP-loaded hydrogels, we observed slower release of BSA in the WHMP-loaded hydrogels (Figure 4.2a). The slower release kinetics of the WHMP-loaded hydrogels is consistent with their higher elastic moduli and lower swelling ratios, which suggest higher cross-linking densities and therefore lower permeabilities.

Understanding protein adsorption on the surfaces of biomaterials is of great importance, since it is the first phenomenon that occurs upon the introduction of a foreign object into the body and is also required for optimal cell adhesion.[33,34] Inorganic particles with negative surface charge can induce protonation of ionizable functional groups in adjacent proteins, leading to increased protein adsorption on the surface and enhanced osteoconduction.[35] There has been relatively little investigation into the effects of the WH particles' surface charge on their high protein adsorption potential and the subsequent cell responses.[36] Here, we confirmed that the WHMP-loaded hydrogels showed higher adsorption of BSA compared to HApMP-loaded hydrogels and alginate controls, which may be another factor contributing to their slower release rates (Figure 4.2b).

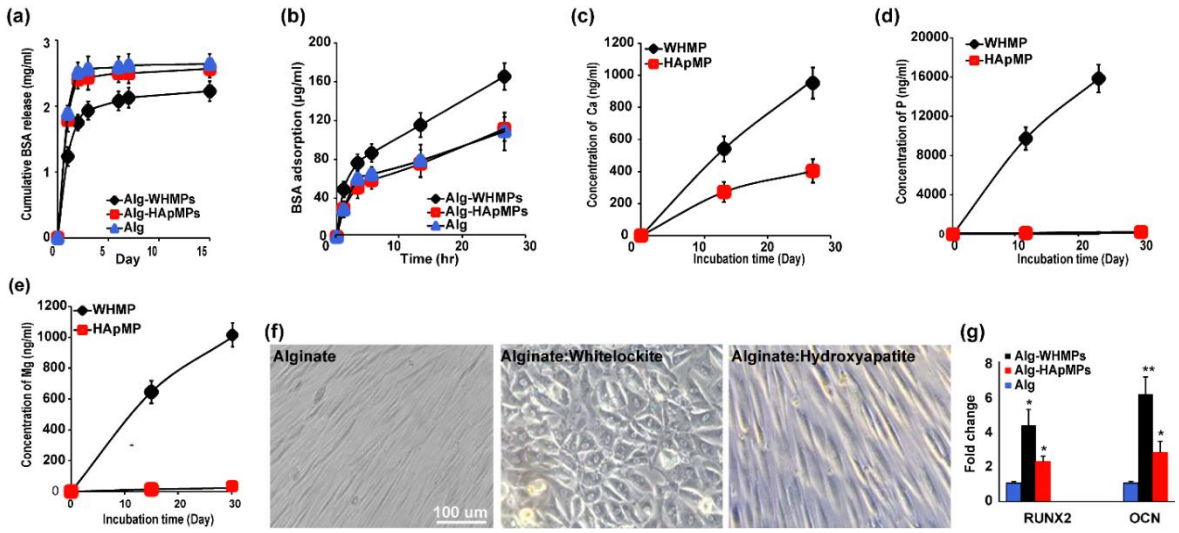

Figure 4.2 Physiochemical Analyses of Hydrogels (a) *In vitro* cumulative bovine serum albumin (BSA) release profile of the hydrogels showing decreased release amounts from the whitlockite microparticles (WHMPs) containing alginate hydrogel with greater stiffness. (b) Protein adsorption study by incubating the alginate hydrogels containing 1 mg/mL WHMPs or hydroxyapatite microparticles (HApMPs) in a 1 mg/mL solution of BSA under constant rotation at 4 ºC for 24 h. (c-e) Inductively coupled plasma mass spectrometry (ICP-MS) curves showing phosphorus, calcium, and magnesium release profiles during a period of 1 month in phosphate buffer solution, respectively. Triplicate measurements were performed for each sample, with background correction. (f) Light microscope images of the 2D plated gingival mesenchymal stem cells (GMSCs) co-cultured with alginate hydrogels (left), the hydrogel containing 1 mg/mL of WHMPs (middle) or HApMPs (right) for three weeks in regular media showing that the ions released from WHMPs have the potential to derive the co-cultured MSCs towards osteogenesis, *in vitro*. (g) Quantitative polymerase chain reaction (qPCR) analysis confirms the expression of the osteogenic markers, OCN and RUNX2, in the 2D-plated GMSCs co-cultured with the hydrogels containing WHMPs, HApMPs, or particle-free hydrogel for three weeks in regular media. (*$p < 0.05$, **$p < 0.01$, and ***$p < 0.001$).

Inductively coupled plasma mass spectrometry (ICP-MS) was utilized to evaluate the amounts of specific ions released from WHMPs and HApMPs. As discussed in the materials preparation section, the alginate is physically cross-linked through ionic interactions with divalent cations (*i.e.*, Ca^{2+}, Mg^{2+}). Our data indicate that WHMPs continuously supply divalent cations (Ca^{2+}, Mg^{2+}), which can act as *in situ* crosslinking agents that further reinforce the structure of the hydrogel over time in significantly greater amounts than HApMPs (Figure 4.2c). Moreover, the

pronounced release of Mg^{2+} and PO_4^{3-} from WHMPs aided in the highly osteogenic nature of these hydrogels (Figure 4.2d,e). Although the Ca:Mg ratio is not 1:1, we see a similar pattern of Ca^{2+} and Mg^{2+} release from the WHMPs. As previous studies reported, synthesizing pure WHMP under laboratory conditions is difficult and it usually does not precipitate according to its theoretical compositional molar ratio ($Mg:P:Ca = 2:14:18$).[26] However, a recent study reported that the successful precipitation of pure WHMPs requires excess Mg^{2+} ions and acidic conditions, which in turn result in higher concentrations of released Mg^{2+} ions from the WHMPs.[18] Thus, the WHMPs utilized in this study have been synthesized under acidic conditions using excess Mg^{2+} ions.[18] Synthetic hydroxyapatite is known as one of the most stable bioceramics under physiological conditions, with limited release of ions such as calcium and phosphate.[37,38] Recently, we have shown the potential use of HAp in alginate hydrogel for craniofacial tissue engineering in the presence of GMSCs.[39] Interestingly, the higher concentrations of released ions from WH particles resulted in morphological changes to the 2D cultured GMSCs after co-culturing with hydrogels containing 1 mg/mL WHMPs compared to the HApMPs containing hydrogel for 3 weeks (Figure 4.2f), and their osteogenic differentiation was confirmed by gene expression studies using qPCR analysis (Figure 4.2g).

We tested GMSCs that were harvested from healthy human gingival tissue. Following *in vitro* expansion, the GMSCs were encapsulated in Alg-RGD hydrogels containing WHMPs or HApMPs and were used in the *in vitro* osteogenic assays. Cell-free samples served as negative controls. Live/dead assays confirmed the high viability of the GMSCs in all of the experimental groups (Figure 4.3a). The quantitative measurements confirmed over 80% viability in all studied groups (Figure 4.3b). The calcein-AM staining images show the morphology of the encapsulated

GMSC after 4 weeks of incubation (Figure S4.1a). The identity of the encapsulated cells was determined by measuring the expression of surface markers with flow cytometry (Figure S4.1b).

Secretion of paracrine signaling factors such as growth factors, cytokines, and chemokines within the microenvironment niche of osteogenic cells helps maintain the homeostasis and architecture of bone.[40] Osteoprotegerin (OPG) is a soluble factor belonging to the tumor necrosis factor family and a decoy receptor of receptor activator of NF-κB ligand (RANKL), also known as osteoclast inhibitory factor (OCIF).[41] Moreover, OPG is one of the main regulators of bone metabolism and is known to have a suppressing effect on the osteoclast activity and differentiation.[42] Osteopontin (OPN), also known as the bone bridge, is an abundant non-collagenous protein in the bone matrix that bridges cells to the mineralized matrix with its RGD motif, which can bind to integrins and enables adhesion to calcium phosphate of the bone.[43,44] Parathyroid hormone (PTH) is known to have a regulatory role on calcium homeostasis and bone turnover regulation and to enhance differentiation of osteoblastic precursors and to prevent their apoptosis.[45] Leptin is a product of adipocytes that regulates the appetite by acting on the hypothalamus. However, leptin is also secreted by various cells, such as bone marrow and primary cultures of human osteoblasts regulating bone metabolism.[46] In addition, leptin can induce osteoblast differentiation, promote mineralization, and inhibit the generation of osteoclasts.[47]

Here, we used four different concentrations of WHMPs and HApMPs to assess the effects of the microparticle concentration on the osteogenic potential of the hydrogels as shown schematically in Figure 4.3c. The heatmaps in Figure 4.3d show that secretion of all five bone metabolism-related factors was higher in the hydrogels containing WHMPs in comparison to the HApMP group in a concentration-dependent manner. The higher concentrations of secreted OPG

prompted us to study the effects of WHMPs in combination with GMSCs on the down-regulation of osteoclasts.

The results of the secretome assay revealed that hydrogels containing 1 mg/mL of the microparticles had the highest osteogenic potential; therefore, we selected 1 mg/mL as the optimum concentration to study the osteogenic properties of the hydrogels. To test this hypothesis, we encapsulated GMSCs in Alg-RGD containing 1 mg/mL of WHMPs or HApMPs and incubated them for 4 weeks under regular or osteogenic culture conditions. After 4 weeks of incubating in the osteogenic media, the GMSCs encapsulated in the WHMPs embedded hydrogels showed significantly higher mineralization in comparison to HApMP-containing hydrogels, as determined by XO staining (Figure 4.3e,f).

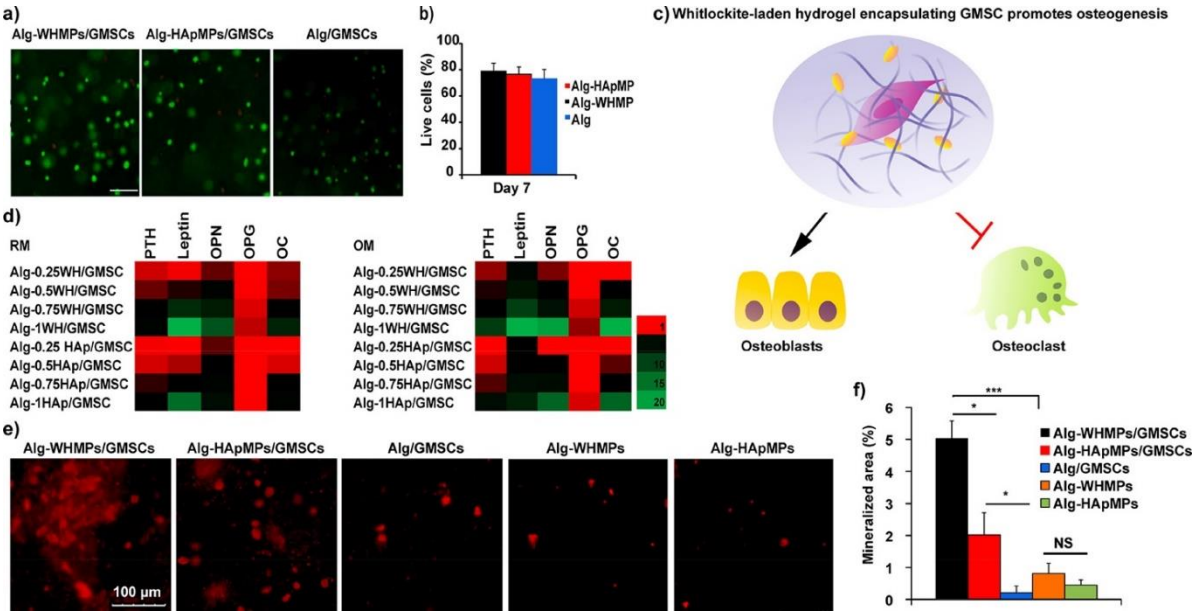

Figure 4.3. ***In vitro*** **3D encapsulation analysis of human gingival mesenchymal stem cells (GMSCs).** (a) Fluorescence images visualizing viability of the encapsulated GMSCs after seven days. Scale bar 250 µm. (b) Quantitative viability analyses did not show any significant difference between the cell-laden hydrogels with different compositions ($p > 0.05$). (c) Schematic representation showing the capability of whitlockite-laden hydrogels in osteodifferentiation of encapsulated GMSCs while down-regulating the osteoclastic activity through soluble factors. (d) Bone metabolism assay heat maps showing secretion of parathyroid hormone (PTH), leptin, osteopontin (OPN), osteoprotegrin (OPG), and osteocalcin (OC) from the hGMSCs encapsulated in hydrogels containing different concentrations of whitlockite microparticles (WHMPs) or hydroxyapatite microparticles (HApMPs) (0.25, 0.5, 0.75, and 1 mg/mL) after culturing in regular culture medium (RM) or osteogenic culture medium (OM) for four weeks, respectively. (e) Xylenol orange (XO) straining was used for histochemical analyses done on the *in vitro* mineralization of the cell-laden hydrogels for four weeks in the osteogenic culture medium. (f) Quantitative measurement of the mineralization based on XO staining. (NS: not significant. *$p < 0.05$, and ***$p < 0.001$).

Higher solubility of WH and faster release of Mg ions from the WH composites account for the enhanced osteogenesis compared to HAp-based hydrogels.[20] Higher intracellular alkaline phosphatase (ALP) activity has also been observed in the presence of higher Mg concentrations.[48] We used gene expression analyses of osteogenic markers such as ALP, osteocalcin (OCN), and

Runt-related transcription factor 2 (RUNX2) to study the roles of the composition and characteristics of the hydrogel on the osteogenic properties of the GMSCs. Reverse transcription polymerase chain reaction results demonstrated that the cells encapsulated in the hydrogels containing WHMPs had significantly higher expression of the osteogenic markers in comparison to the hydrogels containing HApMPs or particle-free Alg-RGD hydrogels in both regular and osteogenic culture media (Figure 4.4a,b). Altogether, these results revealed that under physiological conditions, WHMPs will support osteogenic differentiation of encapsulated GMSCs, at least in part, by continuously supplying PO_4^{3-} and Mg^{2+}, as confirmed by ICP-MS assays.

The mitogen-activated kinases (MAPKs) are important mediators of cellular response to a wide variety of stimuli and are known to be central signal transducers in regulating bone homeostasis and skeleton formation that specifically influence osteoblast commitment and differentiation.[49] Three important members of the MAPK family, namely ERK, JNK, and P38, can become activated at early or late phases of osteo-differentiation of stem cells, which can result in modulation of various osteogenic transcription factors including RUNX2, OCN, DLX5, and Osterix.[50,51] Biochemical analyses determined that ERK actively contributes to regulating the transcriptional activity of RUNX2 through phosphorylation of its S301 and S319 sites.[52] Moreover, active ERK can utilize the association between ERK and RUNX2 for binding to the promoters of OCN in osteoblasts.[53] Similar to what has been reported for ERK, P38 enhances osteoblast differentiation in part by phosphorylation of RUNX2.[54] In addition to its role in regulating cell death and apoptosis, JNK is known as a major osteoblast differentiation regulator.[55] Furthermore, mechanical stimuli can direct osteogenesis by activation of P38, ERK, and JNK.[56,57] The ERK and JNK are known to be critical regulators of the transcription factor activator protein-

1 (AP-1), an important mediator of osteogenic differentiation, which can bind to the promoter regions of mechanosensitive genes.[58]

The results of ICP-MS studies along with our mechanical characterization of the hydrogels containing WHMPs or HApMPs suggest that the Ca^{2+} released from WHMPs can act as an *in situ* cross-linking agent that further reinforces the hydrogel structure and increases its elasticity. The protein expression studies demonstrated that bands of P38MAPK and p-P38MAPK, ERK and p-ERK, JNK and p-JNK, OCN, and RUNX2 were detected in both groups, including Alg-RGD/WHMPs and Alg-RGD/HApMPS hydrogels (Figure 4.4c,d); however, the intensities of the acquired bands were significantly different, consistent the higher osteogenic potential of the WHMPs in comparison to the HApMPs (Figure 4.4e). The higher elasticity of the hydrogels containing WHMPs can activate ERK, JNK, and P38 MAPK pathways in the encapsulated GMSCs, as confirmed by the western blot results, suggesting that the hydrogel itself might be actively contributing to osteogenesis through its mechanical properties in addition to the osteogenic nature of the embedded inorganic microparticles.

The pyridinyl imidazole molecule (SB203580) has been considered as a specific p38α/β inhibitor.[59] Earlier studies reported that treating cells with SB203580 can abolish osteoblast differentiation.[60] Here, we aimed to test the effect of P38 MAPK inhibitor in differentiation of the encapsulated GMSCs in the inductive media. Gingival mesenchymal stem cells were pretreated with a p38α/β inhibitor (SB203580) before starting the osteogenic differentiation, then encapsulated in alginate hydrogel containing WHMPs or HApMPs at concentrations of 10^6 cells/mL. Interestingly, inhibiting the P38 MAPK did not result in amplification of Runx2 or ALP gene expressions, but the OCN was slightly amplified, which can be considered as negligible due to the high (over 33) cycle threshold values (CT) (Figure 4.4b).

Moreover, the results of Western blot analysis confirmed that after inhibition of P38 MAPK in the encapsulated cells, significant downregulation was observed in all the tested osteogenic markers (Figure 4.4c-e). The schematic image in Figure 4.4f summarizes the molecular mechanism underlying the osteoconduction by whitlockite-laden alginate hydrogel.

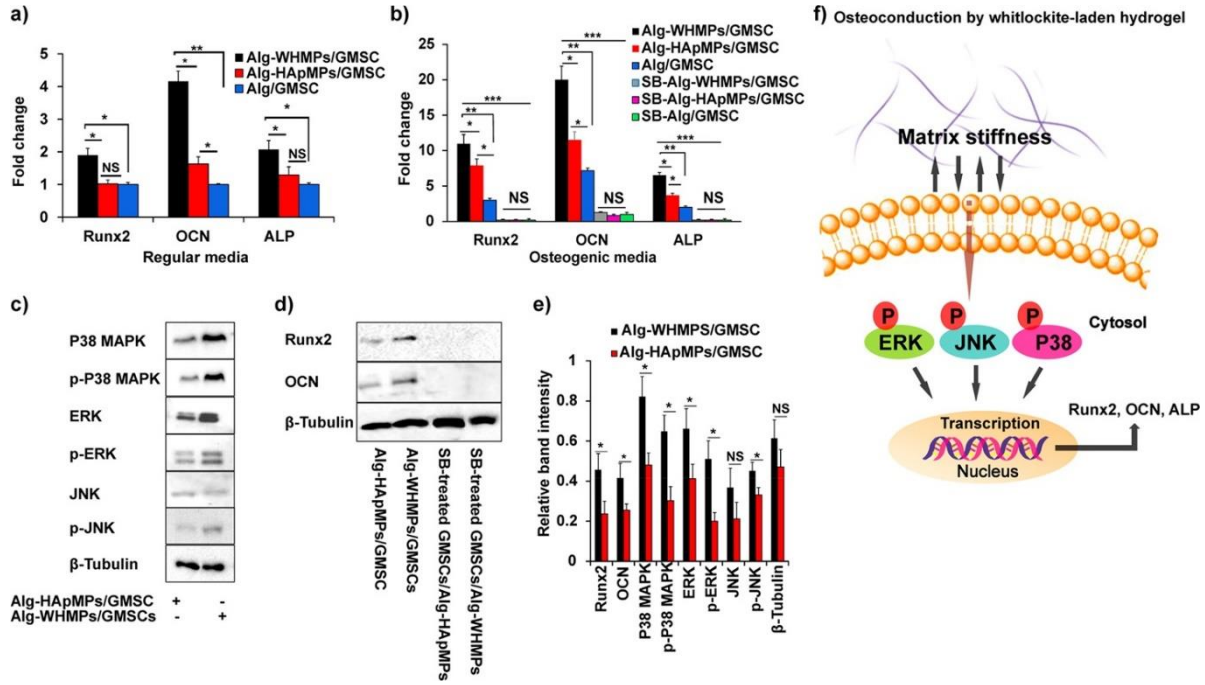

Figure 4.4. Genetic analyses of 3D encapsulated human gingival mesenchymal stem cells (GMSCs). (a,b) Quantitative polymerase chain reaction (qPCR) reaction analyses exhibiting expressions of the osteogenic markers, Runx2, OCN, and ALP four weeks post incubation in regular and osteogenic media, respectively. The qPCR results for the SB203580-treated encapsulated GMSCs demonstrate that only OCN was slightly amplified, but it can be considered as negligible since the cycle threshold values (CT) are over 33; the difference between groups was not statistically significant ($p>0.05$). (c) With higher elastic moduli, the WHMPs incorporated hydrogel shows higher phosphorylation levels of P38, extracellular signal-regulated kinase (ERK), and Jun N-terminal kinase (JNK) mitogen-activated protein kinases (MAPKs) in the encapsulated GMSCs. (d) Western blot studies revealed differences in the expression of osteogenesis regulators with higher expression of Runx2 and OCN in the encapsulated GMSCs in WHMPs-loaded alginate hydrogels. Inhibition of P38 MAPK with SB203580 resulted in diminishing expression of Runx2 and OCN in the encapsulated GMSCs, while non-treated GMSCs expressed them after incubation in osteogenic culture medium for four weeks. (e) Quantification of relative levels of the acquired western blot band intensities. (f) Summary of the molecular mechanism underlying the osteoconduction by whitlockite-laden alginate hydrogel. (NS: not significant. *$p < 0.05$, **$p < 0.01$, and ***$p < 0.001$).

Immunofluorescence (IF) analyses revealed that the percentages of encapsulated GMSCs expressing OCN and RUNX2 were significantly higher in the hydrogels containing WHMPs

compared to the ones containing HApMPs or the particle-free hydrogels (Figure 4.5a-d). Also, the intensities of the expressed markers were higher in the presence of WHMPs. Additionally, results of the IF staining with antibodies against P38 MAPK were in good agreement with the results obtained by Western blot analyses (Figure 4.5e,f).

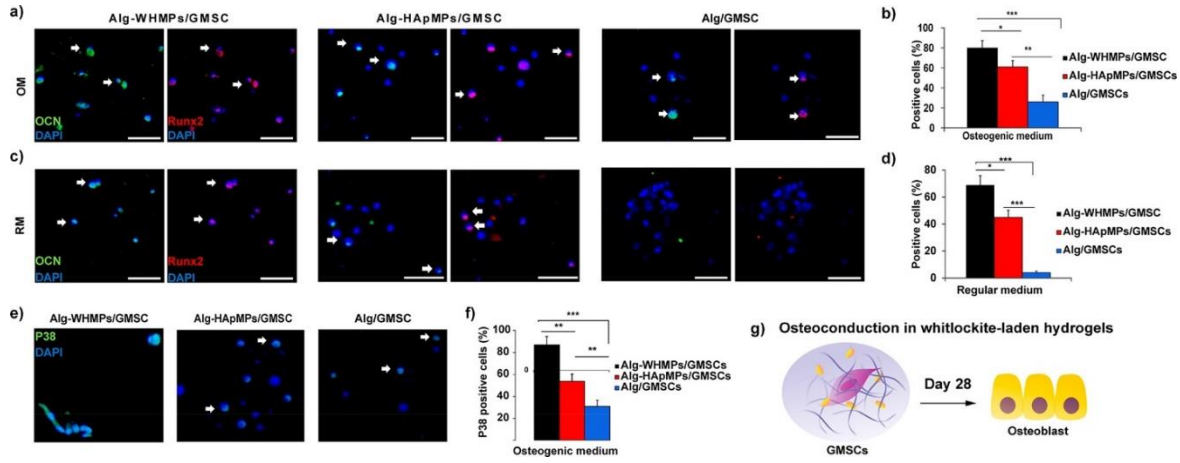

Figure 4.5. Osteoconductive analysis of tested hydrogels. Incorporation of whitlockite microparticles (WHMPs) in the alginate hydrogel improves the osteoconductive potential of the mesenchymal stem cell encapsulating hydrogel. Immunofluorescent microscopy images showing positive staining (indicated by small white arrows) of OCN (green) and Runx2 (red) in the hydrogels encapsulating human gingival mesenchymal stem cells (hGMSCs) after four weeks of incubating in (a,c) osteogenic medium or regular medium, respectively. Cellular nuclei were counterstained with 4′,6-diamidino-2-phenylindole (DAPI) (blue). Scale bar is 100 µm. (b,d) Quantitative analyses of positive cells under osteogenic and regular culture medium conditions, respectively. (e) Incorporation of WHMPs in the alginate hydrogel triggers activation of p38 mitogen-activated protein kinase (MAPK) pathway in the encapsulated GMSCs. Immunofluorescent microscopy images show positive staining of P38 MAPK (green) and DAPI (blue). Scale bar is 50 µm. (f) Quantitative analysis of P38 positive cells under osteogenic culture medium condition. OM: : osteogenic medium, RM: : rregular medium. (g) Schematic image showing osteoconduction by whitlockite-laden hydrogel (*$p < 0.05$, **$p < 0.01$, and ***$p<0.001$).

Osteoclasts are specialized multinucleated giant cells that are formed by the fusion of the monocyte-macrophage precursors. They can be characterized by F-actin ring formation and high tartrate-resistant acidic phosphatase (TRAP) enzyme activity.[61] Intriguingly, MSCs have been proposed to play profound roles in down-regulating osteoclastic activity.[62] Additionally, previous studies demonstrated that osteoblasts have higher proliferation potential in comparison to osteoclasts in the presence of Mg^{2+} ions and alkaline environments because osteoblasts can better tolerate the high alkalinity of the environment and further proliferate while osteoclasts cannot.[21,63] One proposed mechanism related to this restriction of osteoclast proliferation and activity is that *TRAP*, a gene associated with osteoclast differentiation and function, has lower activity levels in the presence of Mg^{2+} ions; thus, osteoclasts need more time to develop their activities fully.

Moreover, the secretome of osteogenic cells has important paracrine functions in balancing bone formation with bone resorption. Receptor activator of NF-κB (RANK)/receptor activator of NF-κB ligand (RANK/RANKL) is one of the main osteoclastogenesis pathways but OPG is believed to act as a decoy receptor for RANKL that supports the anti-osteoclastogenic potential of MSCs.[64] Additionally, it has been reported that leptin can significantly reduce the number of TRAP-positive osteoclasts through the RANKL/RANK/OPG system since it increases transcription of osteoprotegerin (OPG) messenger RNA and expression of the protein in the peripheral blood mononuclear cells (PBMCs).[47,65] Another study showed that leptin promotes the osteogenic activity of human dental stem cells.[66] As the heatmaps in Figure 3c show, secretion of OPG and leptin, which are potent osteoclast suppressive factors, from the encapsulated GMSCs increases with increasing concentration of WHMPs.

The light microscope images indicate that macrophages successfully developed into multinucleated osteoclasts with high TRAP activity in the absence of GMSCs, but their

differentiation was restricted when osteoclast precursors were co-cultured with hydrogels encapsulating GMSCs (Figure 4.6a,bi,ii). The colorimetric demonstration of TRAP activity in culture supernatants is shown in Figure S1c. We observed even more restrictions when we included HApMPs or WHMPs along with GMSCs in the hydrogel. Interestingly, not only was differentiation of osteoclasts suppressed in the presence of WHMPs, but also the number of attached macrophages that we used to study osteoclastogenesis was significantly reduced, suggesting that the presence of WHMPs disfavored the viability and differentiation of macrophages (Figure 4.6a,biii,iv). Actin staining also confirmed the formation of giant, multinucleated osteoclasts in the absence of GMSCs (Figure 4.6ci). The graph in Figure 6d demonstrates quantitative quantification of the TRAP activity in culture media. The schematic image in Figure 6e shows the downregulation of osteoclastic activity in the co-cultured BMMs. Additionally, the encapsulated GMSCs were highly viable after 4 days of co-culture with macrophages in osteoclastogenic culture media (Figure S4.2a,b).

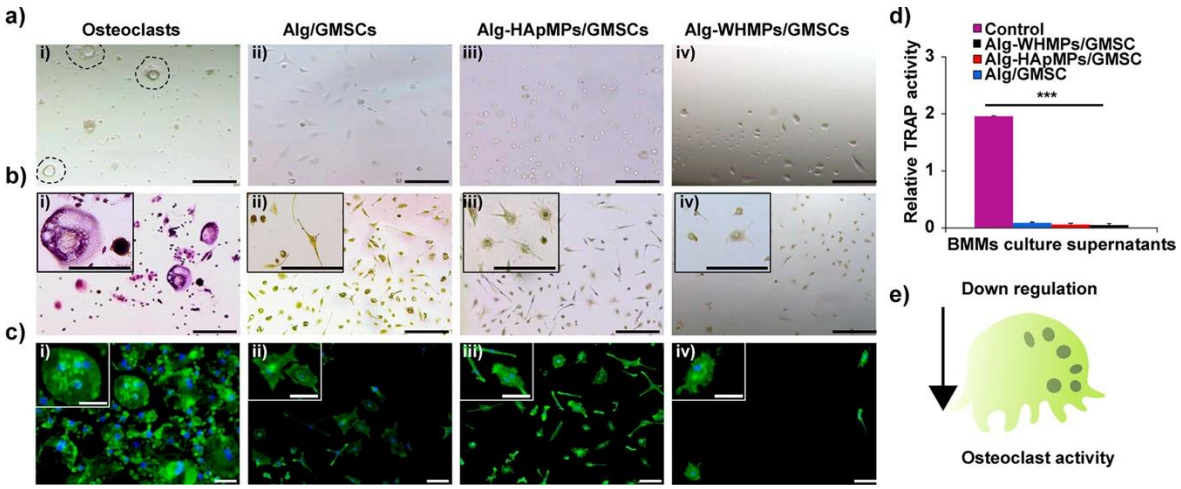

Figure 4.6 Osteoclast activity of human gingival mesenchymal stem cells (GMSCs). (a) Light microscope images, (b) tartrate-resistant acidic phosphatase (TRAP) staining, and (c) F-actin fluorescent imaging of the bone marrow macrophages (BMMs) (i) cultured alone, or co-cultured with (ii) GMSCs encapsulated in Alg-hydrogel, (iii) GMSCs encapsulated in Alg-HApMP (hydroxyapatite microparticle) hydrogel, or (iv) GMSCs encapsulated in Alg-WHMP (whitlockite microparticles) hydrogel. The dashed lines outline the border of giant multinucleated osteoclasts. Scale bars are 200 µm in panels (a) and (b), and 100 µm in panel (c). Inserts demonstrate higher magnification of the images, scale bars are 100 µm (panel b) and 50 µm (panel c). (d) Quantification of the TRAP activity in culture media. (e) Schematic image showing downregulation of the osteoclastic activity in the co-cultured BMMs. ($p<0.001$).

The *in vivo* functionality of the WHMP-loaded alginate hydrogels with encapsulated MSCs were tested in a 7 mm critical-sized calvarial defect in rats. Autologous rat GMSCs (rGMSCs) harvested from rat gingival tissue were utilized in the *in vivo* studies. Our micro-CT (Figure 4.7a,b) and histological (Figure 4.7c,d) analyses showed substantial amounts of bone repair/fill in WHMP-loaded hydrogel group compared to HApMP-loaded hydrogel ($p < 0.05$) or sham group ($P < 0.01$). Histological analysis correlated well with our micro-CT findings showing significantly greater amounts of bone regeneration in the WHMP-loaded hydrogel group. Additionally, Masson's trichrome staining demonstrated significantly better bone regeneration in the whitlockite incorporated hydrogel as indicated by the dark blue color (Figure 4.7f,g).

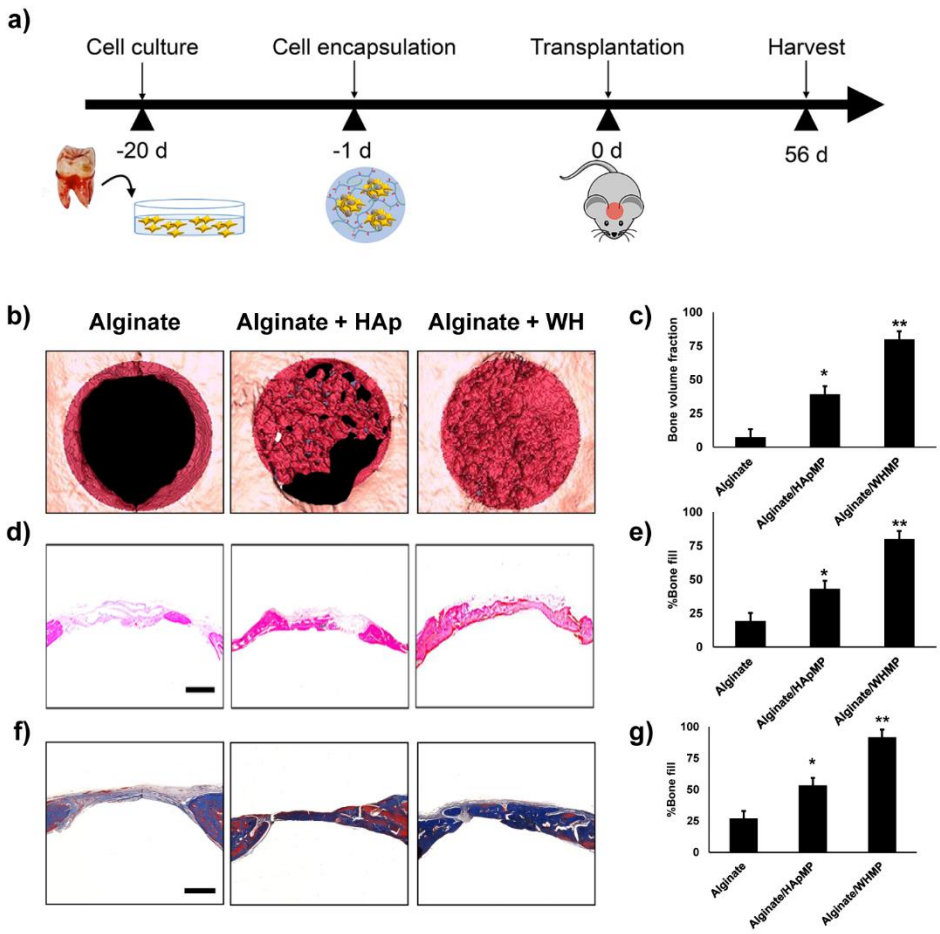

Figure 4.7. *In vivo* delivery of Human gingival mesenchymal stem cells (GMSCs) in a calvarial defect model. (a) Schematic representation depicting isolation of MSCs from gingival tissue, encapsulation of the obtained MSCs in the WHMP-embedded alginate hydrogel and transplanting the cell-laden hydrogel microspheres in the calvarial defect of the rat. (b) Microcomputed tomography (CT) 3D reconstruction of bone repair in calvarial defects (c) Semiquantitative analysis of bone formation *via* micro-CT images. (d) Histomicrographs (H & E) of calvarial bone defects after eight weeks of transplantation, scale bar 100 µm (e) Quantification of the histomorphometry studies demonstrates the relative amount of the regenerated bone. (f) Masson's trichrome staining indicating new bone formation in the calvarial defects after eight weeks of transplantation, scale bar 100 µm (g) Quantification of new bone formation indicated by Masson's trichrome staining. *$p < 0.05$, **$p < 0.01$, $n = 5$ for each group.

Since *in vivo* osteogenesis is dependent also on environmental signals, the hydrogel sections that are in direct contact with the host tissue (borders) are receiving these cues to form new bone-like tissues. Therefore, new bone formation can be seen near host bone edges in control

hydrogels without any osteogenic particles. However, the presence of potent osteogenic agents, here WH particles, can boost osteogenesis throughout the entire implanted area.

4.4 Conclusions and Prospects

The presence of WHMPs enhances the elasticity of a growth factor-free hydrogel, favoring osteogenic differentiation of encapsulated GMSCs through upregulation of the MAPK pathway. Moreover, this growth factor-free hydrogel delivery system exerts osteoclast suppressive properties due to the presence of WHMPs, making it an ideal regenerative treatment modality for craniofacial bone tissue engineering. Our *in vivo* calvarial defect model demonstrated the *in vivo* functionality and bone regenerative potential of the developed Alg-WHMP/GMSC constructs. The main limitations of the current cell delivery systems for bone regeneration include poor adhesion to the surrounding tissue, uncontrolled biodegradation rates and dynamics, and lack of regenerative potential. These results will guide future studies to address the growing demand for smart osteogenic adhesive hydrogels. Upcoming studies will detail the clinical applicability, safety, and efficacy of this approach for bone tissue engineering.

References

1. Amin, S.; Achenbach, S. J.; Atkinson, E. J.; Khosla, S. Trends in Fracture Incidence. *J. Bone Miner. Res*. **2015**, *29*, 581-589.

2. Ullah, I.; Subbarao, R. B.; Rho, G. J. Human Mesenchymal Stem Cells - Current Trends and Future Prospective. *Biosci. Rep*. **2015**, *35*, e00191.

3. Ansari, S.; Seagroves, J. T.; Chen, C.; Shah, K.; Aghaloo, T.; Wu, B. M.; Bencharit, S.; Moshaverinia, A. Dental and Orofacial Mesenchymal Stem Cells in Craniofacial Regeneration: The Prosthodontist's Point of View. *J. Prosth. Den*. **2017**, *118*, 455-461.

4. Sun, Q.; Nakata, H.; Yamamoto, M.; Kasugai, S.; Kuroda, S., Comparison of Gingiva-Derived and Bone Marrow Mesenchymal Stem Cells for Osteogenesis. *J. Cell. Mol. Med*. **2019**, *23*, 7592-7601.

5. Tomar, G. B.; Srivastava, R. K.; Gupta, N.; Barhanpurkar, A. P.; Pote, S. T.; Jhaveri, H. M.; Mishra, G. C.; Wani, M. R., Human Gingiva-Derived Mesenchymal Stem Cells Are Superior to Bone Marrow-Derived Mesenchymal Stem Cells for Cell Therapy in Regenerative Medicine. *Biochem. Biophys. Res. Commun*. **2010**, *393*, 377-383.

6. Takano, T.; Li, Y.-J.; Kukita, A.; Yamaza, T.; Ayukawa, Y.; Moriyama, K.; Uehara, N.; Nomiyama, H.; Koyano, K.; Kukita, T. Mesenchymal Stem Cells Markedly Suppress Inflammatory Bone Destruction in Rats with Adjuvant-Induced Arthritis. *Lab. Invest*. **2014**, *94*, 286-296.

7. Moshaverinia, A.; Chen, C.; Akiyama, K.; Xu, X.; Chee, W. W. L.; Schricker, S. R.; Shi, S. Encapsulated Dental-Derived Mesenchymal Stem Cells in an Injectable and Biodegradable Scaffold for Applications in Bone Tissue Engineering. *J. Biomed. Mater. Res. A* **2013**, *101*, 3285-3294.

8. Moshaverinia, A.; Chen, C.; Xu, X.; Akiyama, K.; Ansari, S.; Zadeh, H. H.; Shi, S. Bone Regeneration Potential of Stem Cells Derived from Periodontal Ligament or Gingival Tissue Sources Encapsulated in RGD-Modified Alginate Scaffold. *Tiss. Eng. A* **2014**, *20*, 611-621.

9. Schneider, R. K.; Puellen, A.; Kramann, R.; Raupach, K.; Bornemann, J.; Knuechel, R.; Pérez-Bouza, A.; Neuss, S. The Osteogenic Differentiation of Adult Bone Marrow and Perinatal Umbilical Mesenchymal Stem Cells and Matrix Remodelling in Three-Dimensional Collagen Scaffolds. *Biomaterials* **2010**, *31*, 467-480.

10. Meinel, L.; Karageorgiou, V.; Fajardo, R.; Snyder, B.; Shinde-Patil, V.; Zichner, L.; Kaplan, D.; Langer, R.; Vunjak-Novakovic, G. Bone Tissue Engineering Using Human Mesenchymal Stem Cells: Effects of Scaffold Material and Medium Flow. *Ann. Biomed. Eng*. **2004**, *32*, 112-122.

11. Bensaıd, W.; Triffitt, J.; Blanchat, C.; Oudina, K.; Sedel, L.; Petite, H. A Biodegradable Fibrin Scaffold for Mesenchymal Stem Cell Transplantation. *Biomaterials* **2003**, *24*, 2497-2502.

12. Ansari, S.; Chen, C.; Xu, X.; Annabi, N.; Zadeh, H. H.; Wu, B. M.; Khademhosseini, A.; Shi, S.; Moshaverinia, A. Muscle Tissue Engineering Using Gingival Mesenchymal Stem Cells Encapsulated in Alginate Hydrogels Containing Multiple Growth Factors. *Ann. Biomed. Eng*. **2016**, *44*, 1908-1920.

13. Moshaverinia, A.; Chen, C.; Akiyama, K.; Ansari, S.; Xu, X.; Chee, W. W.; Schricker, S. R.; Shi, S. Alginate Hydrogel as a Promising Scaffold for Dental-Derived Stem Cells: An *in vitro* Study. *J. Mater. Sci. Mater. Med*. **2012**, *23*, 3041-3051.

14. Burdick, J. A.; Mason, M. N.; Hinman, A. D.; Thorne, K.; Anseth, K. S. Delivery of Osteoinductive Growth Factors from Degradable PEG Hydrogels Influences Osteoblast Differentiation and Mineralization. *J. Contr. Rel*. **2002**, *83*, 53-63.

15. Gaharwar, A. K.; Mihaila, S. M.; Swami, A.; Patel, A.; Sant, S.; Reis, R. L.; Marques, A. P.; Gomes, M. E.; Khademhosseini, A. Bioactive Silicate Nanoplatelets for Osteogenic Differentiation of Human Mesenchymal Stem Cells. *Adv. Mater*. **2013**, *25*, 3329-3336.

16. Xavier, J. R.; Thakur, T.; Desai, P.; Jaiswal, M. K.; Sears, N.; Cosgriff-Hernandez, E.; Kaunas, R.; Gaharwar, A. K. Bioactive Nanoengineered Hydrogels for Bone Tissue Engineering: A Growth-Factor-Free Approach. *ACS Nano* **2015**, *9*, 3109-3118.

17. Sevari, S. P.; Shahnazi, F.; Chen, C.; Mitchell, J. C.; Ansari, S.; Moshaverinia, A. Bioactive Glass-Containing Hydrogel Delivery System for Osteogenic Differentiation of Human Dental Pulp Stem Cells. *J. Biomed. Mater. Res. A* **2019**, *108*, 557-564.

18. Jang, H. L.; Jin, K.; Lee, J.; Kim, Y.; Nahm, S. H.; Hong, K. S.; Nam, K. T. Revisiting Whitlockite, the Second Most Abundant Biomineral in Bone: Nanocrystal Synthesis in Physiologically Relevant Conditions and Biocompatibility Evaluation. *ACS Nano* **2014**, *8*, 634-641.

19. Jang, H. L.; Zheng, G. B.; Park, J.; Kim, H. D.; Baek, H.-R.; Lee, H. K.; Lee, K.; Han, H. N.; Lee, C.-K.; Hwang, N. S.; Lee, J. H.; Nam, K. T. *In vitro* and *in vivo* Evaluation of Whitlockite Biocompatibility: Comparative Study with Hydroxyapatite and β-Tricalcium Phosphate. *Adv. Healthc. Mater*. **2016**, *5*, 128-136.

20. Cheng, H.; Chabok, R.; Guan, X.; Chawla, A.; Li, Y.; Khademhosseini, A.; Jang, H. L. Synergistic Interplay between the Two Major Bone Minerals, Hydroxyapatite and Whitlockite Nanoparticles, for Osteogenic Differentiation of Mesenchymal Stem Cells. *Acta Biomater*. **2018**, *69*, 342-351.

21. Kim, H. D.; Jang, H. L.; Ahn, H.-Y.; Lee, H. K.; Park, J.; Lee, E.-s.; Lee, E. A.; Jeong, Y.-H.; Kim, D.-G.; Nam, K. T.; Hwang, N. S. Biomimetic Whitlockite Inorganic Nanoparticles-Mediated *in Situ* Remodeling and Rapid Bone Regeneration. *Biomaterials* **2017**, *112*, 31-43.

22. Cargnello, M.; Roux, P. P. Activation and Function of the MAPKs and Their Substrates, the MAPK-Activated Protein Kinases. *Microbiol. Mol. Biol. Rev*. **2011**, *75*, 50-83.

23. Meyer-ter-Vehn, T.; Han, H.; Grehn, F.; Schlunck, G. Extracellular Matrix Elasticity Modulates TGF-B-Induced P38 Activation and Myofibroblast Transdifferentiation in Human Tenon Fibroblasts. *Invest. Ophthalmol. Vis. Sci*. **2011**, *52*, 9149-9155.

24. Xiao, G.; Jiang, D.; Thomas, P.; Benson, M. D.; Guan, K.; Karsenty, G.; Franceschi, R. T. MAPK Pathways Activate and Phosphorylate the Osteoblast-Specific Transcription Factor, Cbfa1. *J. Biol. Chem*. **2000**, *275*, 4453-4459.

25. Winkler, T.; Sass, F. A.; Duda, G. N.; Schmidt-Bleek, K. A Review of Biomaterials in Bone Defect Healing, Remaining Shortcomings and Future Opportunities for Bone Tissue Engineering: The Unsolved Challenge. *Bone Joint Res*. **2018**, *7*, 232-243.

26. Lin Jang, H.; Kyoung Lee, H.; Jin, K.; Ahn, H.-Y.; Lee, H.-E.; Tae Nam, K. Phase Transformation from Hydroxyapatite to the Secondary Bone Mineral, Whitlockite. *J. Mater. Chem. B* **2015**, *3*, 1342-1349.

27. Rasskazova, L. A.; Zhuk, I. V.; Korotchenko, N. M.; Brichkov, A. S.; Chen, Y.-W.; Paukshtis, E. A.; Ivanov, V. K.; Kurzina, I. A.; Kozik, V. V., Synthesis of Magnesium- and Silicon-Modified Hydroxyapatites by Microwave-Assisted Method. *Sci. Rep*. **2019**, *9*, 14836.

28. Shah, F. A.; Lee, B. E. J.; Tedesco, J.; Larsson Wexell, C.; Persson, C.; Thomsen, P.; Grandfield, K.; Palmquist, A. Micrometer-Sized Magnesium Whitlockite Crystals in Micropetrosis of Bisphosphonate-Exposed Human Alveolar Bone. *Nano Lett*. **2017**, *17*, 6210-6216.

29. Timchenko, P. E.; Timchenko, E. V.; Pisareva, E. V.; Vlasov, M. Y.; Volova, L. T.; Frolov, O. O.; Kalimullina, A. R. Experimental Studies of Hydroxyapatite by Raman Spectroscopy. *J. Opt. Tech*. **2018**, *85*, 130-135.

30. Li, J.; Mooney, D. J., Designing Hydrogels for Controlled Drug Delivery. *Nat. Rev. Mater*. **2016**, *1*, 16071.

31. Vermonden, T.; Censi, R.; Hennink, W. E., Hydrogels for Protein Delivery. *Chem. Rev*. **2012**, *112*, 2853-2888.

32. Zhang, Q.; Shi, S.; Liu, Y.; Uyanne, J.; Shi, Y.; Shi, S.; Le, A. D. Mesenchymal Stem Cells Derived from Human Gingiva Are Capable of Immunomodulatory Functions and Ameliorate Inflammation-Related Tissue Destruction in Experimental Colitis. *J. Immun.* **2009**, *183*, 7787-7798.

33. Hartvig, R. A.; van de Weert, M.; Østergaard, J.; Jorgensen, L.; Jensen, H. Protein Adsorption at Charged Surfaces: The Role of Electrostatic Interactions and Interfacial Charge Regulation. *Langmuir* **2011**, *27*, 2634-2643.

34. Ke, P. C.; Lin, S.; Parak, W. J.; Davis, T. P.; Caruso, F. A Decade of the Protein Corona. *ACS Nano* **2017**, *11*, 11773-11776.

35. Dos Santos, E. A.; Farina, M.; Soares, G. A.; Anselme, K. Surface Energy of Hydroxyapatite and B-Tricalcium Phosphate Ceramics Driving Serum Protein Adsorption and Osteoblast Adhesion. *J. Mater. Sci. Mater. Med*. **2008**, *19*, 2307-2316.

36. Qi, C.; Chen, F.; Wu, J.; Zhu, Y.-J.; Hao, C.-N.; Duan, J.-L. Magnesium Whitlockite Hollow Microspheres: A Comparison of Microwave-Hydrothermal and Conventional Hydrothermal Syntheses Using Fructose 1,6-Bisphosphate, and Application in Protein Adsorption. *RSC Adv*. **2016**, *6*, 33393-33402.

37. Kattimani, V. S.; Kondaka, S.; Lingamaneni, K. P., Hydroxyapatite–-Past, Present, and Future in Bone Regeneration. Bone Tissue Regener. *Bone tissue regen. Insights.* **2016**, *7*, BTRI.S36138.

38. Witek, L.; Shi, Y.; Smay, J., Controlling Calcium and Phosphate Ion Release of 3D Printed Bioactive Ceramic Scaffolds: An *in Vitro* Study. *J. Adv. Ceram*. **2017**, *6*, 157-164.

39. Hasani-Sadrabadi, M. M.; Sarrion, P.; Pouraghaei, S.; Chau, Y.; Ansari, S.; Li, S.; Aghaloo, T.; Moshaverinia, A., An Engineered Cell-Laden Adhesive Hydrogel Promotes Craniofacial Bone Tissue Regeneration in Rats. *Sci. Transl. Med*. **2020**, *12*, eaay6853.

40. Han, Y.; You, X.; Xing, W.; Zhang, Z.; Zou, W. Paracrine and Endocrine Actions of Bone-The Functions of Secretory Proteins from Osteoblasts, Osteocytes, and Osteoclasts. *Bone Res*. **2018**, *6*, 16.

41. Kohli, S. S.; Kohli, V. S. Role of RANKL-RANK/Osteoprotegerin Molecular Complex in Bone Remodeling and Its Immunopathologic Implications. *Indian J. Endocr. Metab*. **2011**, *15*, 175-181.

42. Boyce, B. F.; Xing, L. Functions of RANKL/RANK/OPG in Bone Modeling and Remodeling. *Arch. Biochem. Biophys*. **2008**, *473*, 139.

43. Bernards, M. T.; Qin, C.; Ratner, B. D.; Jiang, S. Adhesion of MC3T3-E1 Cells to Bone Sialoprotein and Bone Osteopontin Specifically Bound to Collagen I. *J. Biomed. Mater. Res. A* **2008**, *86*, 779-787.

44. Morinobu, M.; Ishijima, M.; Rittling, S. R.; Tsuji, K.; Yamamoto, H.; Nifuji, A.; Denhardt, D. T.; Noda, M. Osteopontin Expression in Osteoblasts and Osteocytes during Bone Formation under Mechanical Stress in the Calvarial Suture *in vivo*. *J. Bone Mine. Res*. **2003**, *18*, 1706-1715.

45. Fan, Y.; Hanai, J.-I.; Le, P. T.; Bi, R.; Maridas, D.; DeMambro, V.; Figueroa, C. A.; Kir, S.; Zhou, X.; Mannstadt, M.; Baron, R.; Bronson, R. T.; Horowitz, M. C.; Wu, J. Y.; Bilezikian, J. P.; Dempster, D. W.; Rosen, C. J.; Lanske, B. Parathyroid Hormone Directs Bone Marrow Mesenchymal Cell Fate. *Cell Metab*. **2017**, *25*, 661-672.

46. Reseland, J. E.; Syversen, U.; Bakke, I.; Qvigstad, G.; Eide, L. G.; Hjertner, Ø.; Gordeladze, J. O.; Drevon, C. A. Leptin Is Expressed in and Secreted from Primary Cultures of Human Osteoblasts and Promotes Bone Mineralization. *J. Bone Mine. Res*. **2001**, *16*, 1426-1433.

47. Holloway, W. R.; Collier, F. M.; Aitken, C. J.; Myers, D. E.; Hodge, J. M.; Malakellis, M.; Gough, T. J.; Collier, G. R.; Nicholson, G. C. Leptin Inhibits Osteoclast Generation. *J. Bone Mine. Res*. **2002**, *17*, 200-209.

48. Wu, L.; Luthringer, B. J. C.; Feyerabend, F.; Schilling, A. F.; Willumeit, R. Effects of Extracellular Magnesium on the Differentiation and Function of Human Osteoclasts. *Acta Biomate*. **2014**, *10*, 2843-2854.

49. Ge, C.; Xiao, G.; Jiang, D.; Franceschi, R. T. Critical Role of the Extracellular Signal–Regulated Kinase–MAPK Pathway in Osteoblast Differentiation and Skeletal Development. *J. Cell Biol*. **2007**, *176*, 709-718.

50. Ulsamer, A.; Ortuño, M. J.; Ruiz, S.; Susperregui, A. R. G.; Osses, N.; Rosa, J. L.; Ventura, F. BMP-2 Induces Osterix Expression through Up-Regulation of Dlx5 and Its Phosphorylation by p38. *J. Biol. Chem*. **2008**, *283*, 3816-3826.

51. Greenblatt, M. B.; Shim, J.-H.; Glimcher, L. H. Mitogen-Activated Protein Kinase Pathways in Osteoblasts. *Ann. Rev. Cell Dev. Biol*. **2013**, *29*, 63-79.

52. Ge, C.; Xiao, G.; Jiang, D.; Yang, Q.; Hatch, N. E.; Roca, H.; Franceschi, R. T. Identification and Functional Characterization of ERK/MAPK Phosphorylation Sites in the RUNX2 Transcription Factor. *J. Biol. Chem*. **2009**, *284*, 32533-32543.

53. Li, Y.; Ge, C.; Franceschi, R. T. Differentiation-Dependent Association of Phosphorylated Extracellular Signal-Regulated Kinase with the Chromatin of Osteoblast-Related Genes. *J. Bone Mine. Res*. **2010**, *25*, 154-163.

54. Greenblatt, M. B.; Shim, J.-H.; Zou, W.; Sitara, D.; Schweitzer, M.; Hu, D.; Lotinun, S.; Sano, Y.; Baron, R.; Park, J. M.; Arthur, S.; Xie, M.; Schneider, M. D.; Zhai, B.; Gygi, S.; Davis, R.; Glimcher, L. H. The p38 MAPK Pathway Is Essential for Skeletogenesis and Bone Homeostasis in Mice. *J. Clin. Invest*. **2010**, *120*, 2457-2473.

55. Yamashita, M.; Ying, S.-X.; Zhang, G.-m.; Li, C.; Cheng, S. Y.; Deng, C.-x.; Zhang, Y. E. Ubiquitin Ligase Smurf1 Controls Osteoblast Activity and Bone Homeostasis by Targeting MEKK2 for Degradation. *Cell* **2005**, *121*, 101-113.

56. Kearney, E. M.; Farrell, E.; Prendergast, P. J.; Campbell, V. A. Tensile Strain as a Regulator of Mesenchymal Stem Cell Osteogenesis. *Ann. Biomed. Eng*. **2010**, *38*, 1767-1779.

57. Gu, Q.; Tian, H.; Zhang, K.; Chen, D.; Chen, D.; Wang, X.; Zhao, J. Wnt5a/FZD4 Mediates the Mechanical Stretch-Induced Osteogenic Differentiation of Bone Mesenchymal Stem Cells. *Cell. Physiol. Biochem*. **2018**, *48*, 215-226.

58. Liedert, A.; Kaspar, D.; Blakytny, R.; Claes, L.; Ignatius, A. Signal Transduction Pathways Involved in Mechanotransduction in Bone Cells. *Biochem. Biophys. Res. Comm*. **2006**, *349*, 1-5.

59. Cuenda, A.; Rouse, J.; Doza, Y. N.; Meier, R.; Cohen, P.; Gallagher, T. F.; Young, P. R.; Lee, J. C. SB 203580 Is a Specific Inhibitor of a MAP Kinase Homologue Which Is Stimulated by Cellular Stresses and Interleukin-1. *FEBS Lett*. **1995**, *364*, 229-233.

60. Suzuki, A.; Guicheux, J.; Palmer, G.; Miura, Y.; Oiso, Y.; Bonjour, J.-P.; Caverzasio, J. Evidence for a Role of P38 MAP Kinase in Expression of Alkaline Phosphatase During Osteoblastic Cell Differentiation. *Bone* **2002**, *30*, 91-98.

61. Marino, S.; Logan, J. G.; Mellis, D.; Capulli, M. Generation and Culture of Osteoclasts. *BoneKEy Rep*. **2014**, *3*, 570.

62. Oshita, K.; Yamaoka, K.; Udagawa, N.; Fukuyo, S.; Sonomoto, K.; Maeshima, K.; Kurihara, R.; Nakano, K.; Saito, K.; Okada, Y.; Chiba, K.; Tanaka, Y. Human Mesenchymal Stem Cells Inhibit Osteoclastogenesis through Osteoprotegerin Production. *Arthritis Rheum*. **2011**, *63*, 1658-1667.

63. Bushinsky, D. A. Metabolic Alkalosis Decreases Bone Calcium Efflux by Suppressing Osteoclasts and Stimulating Osteoblasts. *Am. J. Physiol. Renal Physiol*. **1996**, *271*, F216-F222.

64. Cho, K.-A.; Park, M.; Kim, Y.-H.; Ryu, K.-H.; Woo, S.-Y. Mesenchymal Stem Cells Inhibit RANK-RANKL Interactions between Osteoclasts and Th17 Cells via Osteoprotegerin Activity. *Oncotarget* **2017**, *8*, 83419-83431.

65. Cornish, J.; Callon, K. E.; Bava, U.; Lin, C.; Naot, D.; Hill, B. L.; Grey, A. B.; Broom, N.; Myers, D. E.; Nicholson, G. C.; Reid, I. R. Leptin Directly Regulates Bone Cell Function *in Vitro* and Reduces Bone Fragility *in Vivo*. *J. Endocrinol*. **2002**, *175*, 405-415.

66. Um, S.; Choi, J.-R.; Lee, J.-H.; Zhang, Q.; Seo, B. Effect of Leptin on Differentiation of Human Dental Stem Cells. *Oral Dis*. **2011**, *17*, 662-669.

67. Liu, Y.; Uyanne, J.; Shi, Y.; Zhang, Q.; Le, A. D.; Shi, S. Mesenchymal Stem Cells Derived from Human Gingiva Are Capable of Immunomodulatory Functions and Ameliorate Inflammation-Related Tissue Destruction in Experimental Colitis. *J. Immunol*. **2009**, *183*, 7787-7798.

68. Pouraghaei, S.; Moztarzadeh, F.; Chen, C.; Ansari, S.; Moshaverinia, A., Microenvironment Can Induce Development of Auditory Progenitor Cells from Human Gingival Mesenchymal Stem Cells. *ACS Biomater. Sci. Eng*. **2020**, *6*, 2263-2273.

69. Lee, K. Y.; Mooney, D. J., Alginate: Properties and Biomedical Applications. *Prog. Polym. Sci*. **2012**, *37*, 106-126.

70. Augst, A. D.; Kong, H. J.; Mooney, D. J., Alginate Hydrogels as Biomaterials. *Macromol. Biosci*. **2006**, *6*, 623-633.

71. Grant, G. T.; Morris, E. R.; Rees, D. A.; Smith, P. J. C.; Thom, D., Biological Interactions between Polysaccharides and Divalent Cations: The Egg-Box Model. *FEBS Letters* **1973**, *32*, 195-198.

72. Rowley, J. A.; Madlambayan, G.; Mooney, D. J., Alginate Hydrogels as Synthetic Extracellular Matrix Materials. *Biomaterials* **1999**, *20*, 45-53.

73. Kuo, C. K.; Ma, P. X., Ionically Crosslinked Alginate Hydrogels as Scaffolds for Tissue Engineering: Part 1. Structure, Gelation Rate and Mechanical Properties. *Biomaterials* **2001**, *22*, 511-521.

74. Sun, J.; Tan, H., Alginate-Based Biomaterials for Regenerative Medicine Applications. *Materials (Basel, Switzerland)* **2013**, *6*, 1285-1309.

75. Hartvig, R. A.; van de Weert, M.; Østergaard, J.; Jorgensen, L.; Jensen, H. Formation of Dielectric Layers and Charge Regulation in Protein Adsorption at Biomimetic Interfaces. *Langmuir* **2012**, *28*, 1804-1815.

76. Nasajpour, A.; Ansari, S.; Rinoldi, C.; Rad, A. S.; Aghaloo, T.; Shin, S. R.; Mishra, Y. K.; Adelung, R.; Swieszkowski, W.; Annabi, N.; Khademhosseini, A.; Moshaverinia, A.; Tamayol, A. A Multifunctional Polymeric Periodontal Membrane with Osteogenic and Antibacterial Characteristics. *Adv. Funct. Mater*. **2018**, *28*, 1703437.

77. Moshaverinia, A.; Ansari, S.; Chen, C.; Xu, X.; Akiyama, K.; Snead, M. L.; Zadeh, H. H.; Shi, S. Co-Encapsulation of Anti-BMP2 Monoclonal Antibody and Mesenchymal Stem Cells in Alginate Microspheres for Bone Tissue Engineering. *Biomater*. **2013**, *34*, 6572-6579.

78. Tevlin, R.; Mcardle, A.; Chan, C. K. F.; Pluvinage, J.; Walmsley, G. G.; Wearda, T.; Marecic, O.; Hu, S.; Paik, K. J.; Senarath-yapa, K.; Atashroo, D. A.; Zielins, E. R.; Wan, D. C.; Weissman, I. L. Osteoclast Derivation from Mouse Bone Marrow. *J. Vis. Exp*. **2014**, *93*, e52056.

79. Dai, Q.; Han, Y.; Xie, F.; Ma, X.; Xu, Z.; Liu, X.; Zou, W.; Wang, J. A RANKL-Based Osteoclast Culture Assay of Mouse Bone Marrow To Investigate the Role of mTORC1 in Osteoclast Formation. *J. Vis. Exp*. **2018**, e56468.

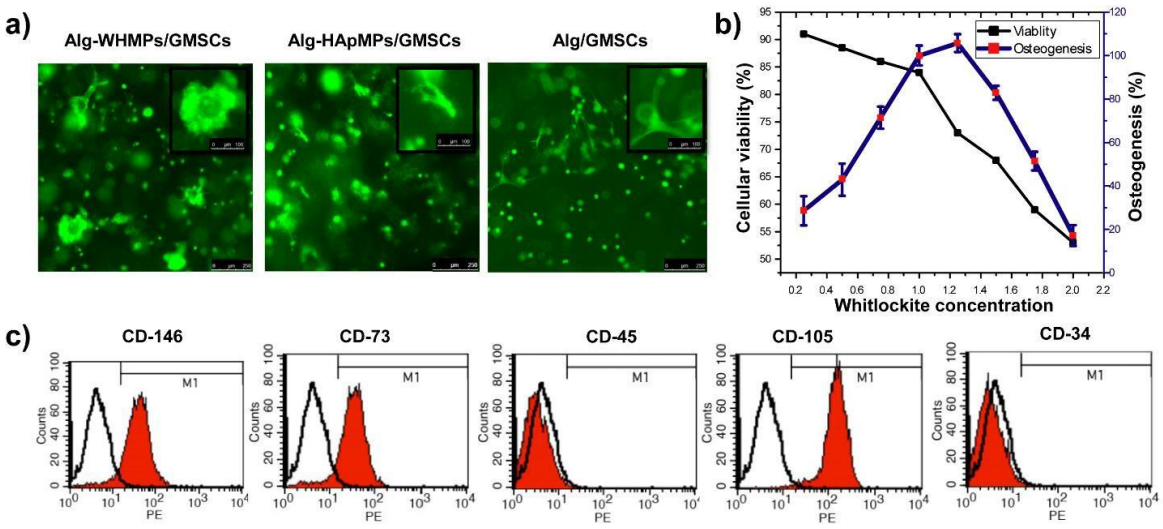

Figure S4.1. (a) Fluorescence images of calcein-AM staining demonstrate morphology and high viability of the encapsulated gingival mesenchymal stem cells (GMSCs) after four weeks of incubation, scale bar 250 µm. Insets are magnified images for better demonstration, scale bar 100 µm. (b) Viability *vs* osteogenesis of the GMSCs encapsulated in alginate hydrogel containing varying concentration of whitlockite microparticles (0.2-2 mg/ml). (c) Expression of stemness surface markers on GMSCs evaluated using flow cytometric analysis.

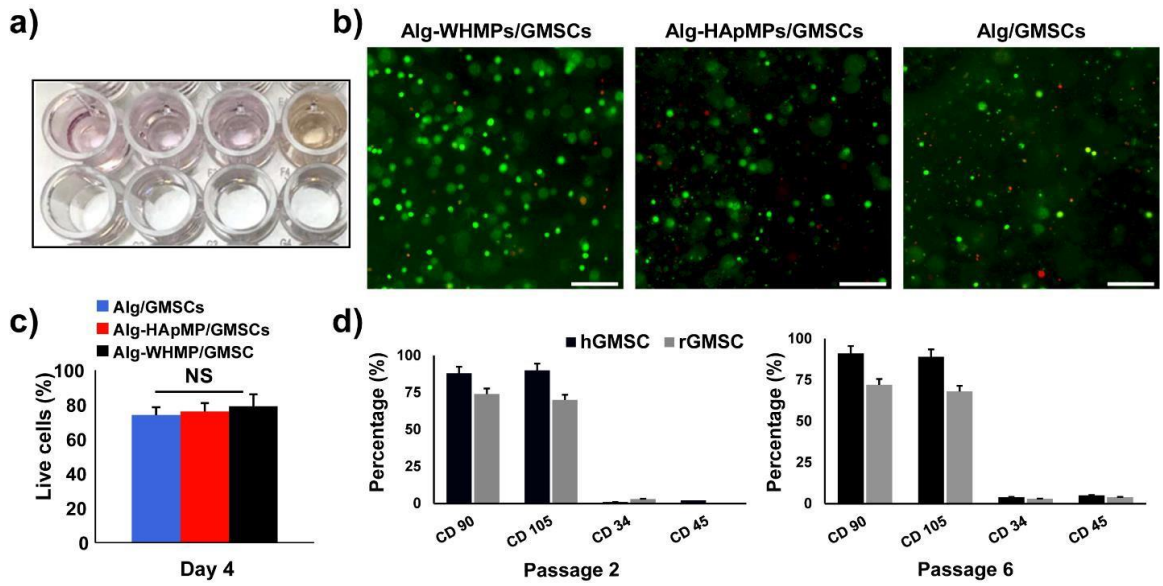

Figure S4.2. (a) Colorimetric demonstration of tartrate-resistant acidic phosphatase (TRAP) activity in culture supernatants. (b) Fluorescence images of live/dead staining demonstrate high viability of the encapsulated gingival mesenchymal stem cells (GMSCs) after four days of co-culturing with bone marrow macrophages (BMMs) under osteoclastogenic culture media. Scale bar 250 µm. (c) Quantitative live/dead results show not significant difference between the viability of GMSCs encapsulated in the different alginate hydrogels (Alg) ($p > 0.05$). (d) Quantification of stemness markers expression on human GMSCs (hGMSCs) and rat GMSCs (rGMSCs) after passages two and six determined by flow cytometry analysis. The results are representative of at least five independent experiments from passages 2–6.

Chapter 5

Conclusions and Prospects

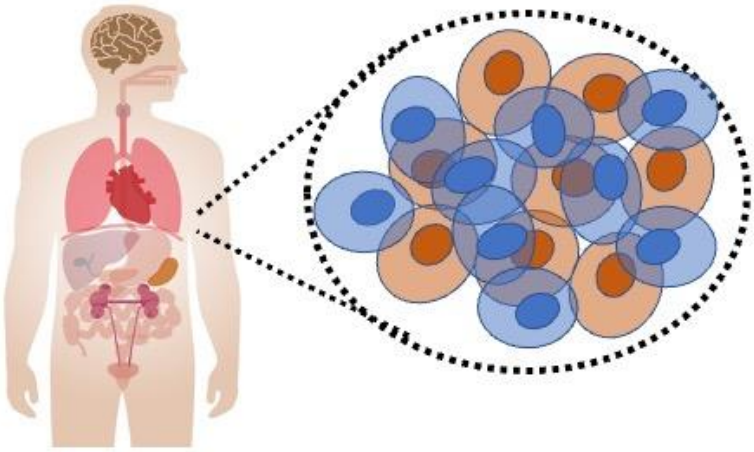

We have shown that our liquid crystal technology catalyzes the assembly of cells into freestanding tissue. By inducing a phase transition in the liquid crystal, we are able to transform the attached cells into a variety of complex 3D cell structures, from standard tissue samples to marbled constructs containing multiple cell types. We have also demonstrated the creation of 3D cellular organoids from our technology, in some cases in unprecedented times of less than six hours from cell seeding.

We are developing a startup buisness that utilizes this liquid crystal technology. Current scaffolding organizations like CASS, Micromeat, and MatrixFood provide vegan polymer entities such as bacteria cellulose, zein, and alginate/pectin combinations, but these materials lack the cell-directing motifs critical to promoting cellular attachment. This process is essential for promoting

cell proliferation, preventing apoptotic cellular programed death and differentiation of satellite muscle cells. Unlike the technology of current scaffold suppliers, our materials not only facilitate cellular attachment, but also demonstrate more endogenous viscoelastic, fluidlike behavior, closely mimicking the native properties of whole cut meat. Tantti Laboratory, Inc., a company based in Taiwan, uses a traditional method in the field of tissue engineering to generate porous 3D scaffolds by dissolving microsphere particles embedded within an elastic, crosslinked resin system under selective solvent. We have demonstrated generation of such porous biomaterials using our liquid crystal material instead, microcarriers, and non-organic solvents, avoiding any toxicity issues that may arise with the methods developed by Tantti. We have also demonstrated coating decellularized plant tissues with our liquid crystal technology on the millimeter scale.

Our liquid crystal technology possesses further advantages. First, our plant-derived liquid crystal results in rapid cellular attachment, avoiding a common bottleneck in the field where incompatible scaffolds must be coated with some animal-derived serum or polymer, such as gelatin, in order to provide fibronectin and induce attachment. Because that method relies on animal-derived biomaterials, it is less viable for commercial applications. Additionally, another incumbent, Geleax, has implemented a gelatin-based technology in this area. They use a proprietary scaffold method of stacking alternating, 45° angled bilayers of cotton gauze and electrospun gelatin nanofibers crosslinked with reactive species. However, scaffolds generated with this method also use animal-based materials and only create stacked cell sheets, lacking the desired marbling effect and elastic-like properties that mimic the nonendogenous extracellular matrix.

In our startup company, we will provide a cell culture technology that enables the growth of complex multi-cellular organoids. We will be a biotools-producing company providing liquid

crystal-based technology, structuring ourselves as a business-to-business organization providing disposable cell culture reagents and contract service projects to those looking to use our materials to make advanced 3D tissue.